Journal of Computational Physics 521 (2025) 113563

Contents lists available at ScienceDirect

Journal of Computational Physics

journal homepage: www.elsevier.com/locate/jcp

A time-relaxation reduced order model for the turbulent channel flow

Ping-Hsuan Tsai [a,*], Paul Fischer [b,c], Traian Iliescu [a]

[a] Department of Mathematics, Virginia Tech, Blacksburg, 24061, VA, United States
[b] Department of Computer Science, University of Illinois at Urbana-Champaign, Urbana, 61801, IL, United States
[c] Department of Mechanical Science & Engineering, University of Illinois at Urbana-Champaign, Urbana, 61801, IL, United States

ARTICLE INFO

Keywords:
Reduced order model
Turbulent channel flow
Spatial filter
Time relaxation
Regularized model

ABSTRACT

Regularized reduced order models (Reg-ROMs) are stabilization strategies that leverage spatial filtering to alleviate the spurious numerical oscillations generally displayed by the classical Galerkin ROM (G-ROM) in under-resolved numerical simulations of turbulent flows. In this paper, we propose a new Reg-ROM, the time-relaxation ROM (TR-ROM), which filters the marginally resolved scales. We compare the new TR-ROM with the two other Reg-ROMs in current use, i.e., the Leray ROM (L-ROM) and the evolve-filter-relax ROM (EFR-ROM) and one eddy viscosity model, the mixing-length model, in the numerical simulation of the turbulent channel flow at $Re_\tau = 180$ and $Re_\tau = 395$ in both the reproduction and the predictive regimes. For each Reg-ROM, we investigate two different filters: (i) the differential filter (DF), and (ii) the higher-order algebraic filter (HOAF). In our numerical investigation, we monitor the Reg-ROM performance with respect to the ROM dimension, N, and the filter order. We also perform sensitivity studies of the three Reg-ROMs with respect to the time interval, relaxation parameter, and filter radius. The numerical results yield the following conclusions: (i) All three Reg-ROMs are significantly more accurate than the G-ROM. (ii) All three Reg-ROMs are more accurate than the ROM projection in terms of Reynolds stresses. (iii) With the optimal parameter values, the new TR-ROM yields more accurate results than the L-ROM and the EFR-ROM in all tests. (iv) The new TR-ROM is more accurate than the mixing-length ROM. (v) For most N values, DF yields the most accurate results for all three Reg-ROMs. (vi) The optimal parameters trained in the reproduction regime are also optimal for the predictive regime for most N values, demonstrating the Reg-ROM predictive capabilities. (vii) All three Reg-ROMs are sensitive to the filter order and the filter radius, and the EFR-ROM and the TR-ROM are sensitive to the relaxation parameter. (viii) The optimal range for the filter radius and the effect of relaxation parameter are similar for the two Re_τ values.

1. Introduction

Reduced order models (ROMs) are computational models that leverage data to approximate the dynamics in a space whose dimension is orders of magnitude lower than the dimension of full order models (FOMs), i.e., models obtained from classical numerical discretizations (e.g., the finite element or spectral element methods). In the numerical simulation of fluid flows, Galerkin ROMs (G-

* Corresponding author.
E-mail addresses: pinghsuan@vt.edu (P.-H. Tsai), fischerp@illinois.edu (P. Fischer), iliescu@vt.edu (T. Iliescu).

https://doi.org/10.1016/j.jcp.2024.113563
Received 11 February 2024; Received in revised form 26 August 2024; Accepted 4 November 2024

Available online 6 November 2024

ROMs), which use a data-driven basis in a Galerkin framework, have provided efficient and accurate approximations of laminar flows, such as the two-dimensional flow past a circular cylinder at low Reynolds numbers [1–4].

However, turbulent flows (e.g., the turbulent channel flow [5,6]) are notoriously hard for the standard G-ROM: To capture the complex dynamics of the turbulent flow, a relatively large number (on the order of hundreds and even thousands [7, Table II][8]) of ROM basis functions are needed. Thus, the resulting G-ROM is relatively high-dimensional, and its computational cost is too large to be used in realistic applications, such as control of turbulent flows. To mitigate this issue, the standard G-ROM is often constructed with relatively few basis functions. The resulting G-ROM is appealing because it is low-dimensional and computationally efficient. It is, however, inaccurate. The reason is that the ROM basis functions that were not used to build the low-dimensional G-ROM have an important role in the G-ROM dynamics. Indeed, as shown in [9], the role of the discarded ROM modes is to extract energy from the system. Without including this dissipation mechanism, the under-resolved G-ROM (i.e., the G-ROM that does not include enough basis functions to capture the underlying complex dynamics) generally yields spurious numerical oscillations. Thus, in the numerical simulation of turbulent flows, these efficient, low-dimensional ROMs are generally equipped with ROM closures (see the review in [7]) and stabilizations (see, e.g., [10–14]). For example, in the reduced order modeling of the turbulent channel flow, ROM closures (e.g., the eddy viscosity ROM [15] and the mixing-length ROM [12]) or ROM stabilizations (e.g., the evolve-filter-relax ROM [12]) have been successfully employed. Regularized ROMs (Reg-ROMs) are stabilizations that leverage ROM spatial filtering of terms of the Navier-Stokes equations to decrease the size of the spurious numerical oscillations and increase the ROM accuracy. The two Reg-ROMs in current use are (i) the Leray ROM (L-ROM) [16–19], in which the velocity component of the convective term of the Navier-Stokes equations is filtered, and (ii) the evolve-filter-relax ROM (EFR-ROM) [16,18], which filters an intermediate approximation of the Navier-Stokes equations, and then relaxes it.

In this paper, we propose a new Reg-ROM, the time-relaxation ROM (TR-ROM), which filters the marginally resolved scales. The main goal of this paper is to investigate the new TR-ROM in the numerical simulation of the turbulent channel flow at friction Reynolds numbers $\mathrm{Re}_\tau = 180$ and 395, in both the reproduction and the predictive regimes. To ensure a thorough assessment of the new TR-ROM, we compare it with the two other Reg-ROMs in current use, i.e., L-ROM and EFR-ROM, and an eddy viscosity approach, the mixing-length ROM. For each Reg-ROM, we investigate two different filters: (i) the differential filter (DF); and (ii) the higher-order algebraic filter. We also compare the three Reg-ROMs with the classical G-ROM (i.e., the ROM that does not use any stabilization or closure). As a benchmark for the three Reg-ROMs and the G-ROM, we use the FOM, which is a direct numerical simulation (DNS) of the turbulent channel flow. Furthermore, in our numerical comparison, we use the projection error, which is the error with respect to the projection of the FOM solution onto the space spanned by the ROM basis functions. We expect the three Reg-ROMs to alleviate the G-ROM spurious numerical oscillations and yield more accurate results with a negligible computational overhead.

It is well known that, in numerical simulation of turbulent flows, the parameters used in the computational setting can have a significant effect on the ROM results. Thus, to ensure a fair assessment of the Reg-ROMs, we perform a sensitivity study of the numerical results with respect to the following parameters: (i) the number of ROM basis functions, N, used to construct the ROM; (ii) the higher-order algebraic filter order, m; (iii) the filter radius, δ; (iv) the relaxation parameter, χ; and (v) the time interval.

The rest of the paper is organized as follows: In Section 2, we present the FOM and the G-ROM. In Section 3, we describe the two ROM spatial filters that we use to construct the Reg-ROMs: the classical differential filter and the higher-order algebraic filter. In Section 4, we leverage these two ROM filters to construct the L-ROM, EFR-ROM, and the new TR-ROM. In Section 5, we quantify the computational cost of the three Reg-ROMs (i.e., L-ROM, EFR-ROM, and TR-ROM) and perform a numerical investigation in the numerical simulation of the turbulent channel flow at friction Reynolds numbers $\mathrm{Re}_\tau = 180$ and 395. In addition, we assess the accuracy of the three Reg-ROMs and their sensitivity with respect to parameters in both the reproduction and the predictive regimes, and, we compare the performance of the Reg-ROMs and mixing-length ROM. In Section 6, we present the conclusions of our numerical investigation, and we outline directions for future research. Finally, in Appendix A, we present a theoretical and numerical investigation of the higher-order algebraic filter.

2. Numerical modeling

In this section, we briefly outline the FOM (Section 2.1) and the G-ROM (Section 2.2) used in our numerical investigation.

2.1. Full order model (FOM)

The governing equations are the incompressible Navier-Stokes equations (NSE) with forcing:

$$\frac{\partial \boldsymbol{u}}{\partial t} + (\boldsymbol{u}\cdot\nabla)\boldsymbol{u} = -\nabla p + \frac{1}{\mathrm{Re}}\nabla^2\boldsymbol{u} + \mathbf{f}(\boldsymbol{u}), \qquad \nabla\cdot\boldsymbol{u} = 0, \tag{2.1}$$

where $\boldsymbol{u}$ is the velocity and p the pressure. Here, $\mathbf{f}(\boldsymbol{u})$ is a uniform forcing vector field function in the streamwise direction, x, that enforces a time-constant flow rate on the solution. The initial condition consists of random noise, which eventually triggers a transition to turbulence, and the boundary conditions are periodic in the streamwise and spanwise directions of the channel, and homogeneous Dirichlet in the wall-normal direction.

The FOM is constructed using the Galerkin projection of (2.1) onto the spectral element space with the $\mathcal{P}_q - \mathcal{P}_q$ velocity-pressure coupling. Following [20], a semi-implicit scheme BDFk/EXTk is used for time discretization. Specifically, the kth-order backward differencing (BDFk) is used for the time-derivative term, kth-order extrapolation (EXTk) for the advection and forcing terms, and implicit treatment on the dissipation terms. As discussed in [20], $k = 3$ is used to ensure the imaginary eigenvalues associated with the skew-symmetric advection operator are within the stability region of the BDFk/EXTk time-stepper.

The full discretization leads to solving a linear unsteady Stokes system at each time step. The forcing term effectively adds an impulse-response streamwise velocity field. This impulse response is scaled appropriately at each time step to ensure that the mean velocity at each timestep yields the prescribed flow rate [21,22]. The treatment of the constant flow rate and the detailed derivation of the FOM can be found in [13] and [23], respectively.

2.2. Galerkin reduced order model (G-ROM)

In this section, we introduce the G-ROM. We follow the standard proper orthogonal decomposition (POD) procedure [24,25] to construct the reduced basis function. To this end, we collect a set of DNS solutions lifted by the zeroth mode $\boldsymbol{\varphi}_0$, and form its corresponding Gramian matrix using the L^2 inner product (see, e.g., [14,19] for alternative strategies). The first N POD basis functions $\{\boldsymbol{\varphi}_i\}_{i=1}^N$ are constructed from the first N eigenmodes of the Gramian. Setting the zeroth mode, $\boldsymbol{\varphi}_0$, to the time-averaged velocity field in the time interval in which the snapshots were collected, the G-ROM is constructed by inserting the ROM basis expansion

$$\boldsymbol{u}_{\mathrm{r}}(\mathbf{x}) = \boldsymbol{\varphi}_0(\mathbf{x}) + \sum_{j=1}^{N} u_{\mathrm{r},j}\boldsymbol{\varphi}_j(\mathbf{x}) \tag{2.2}$$

into the weak form of (2.1): *Find* $\boldsymbol{u}_r$ *such that, for all* $\mathbf{v} \in \mathbf{X}_0^N$,

$$\left(\frac{\partial \boldsymbol{u}_{\mathrm{r}}}{\partial t}, \mathbf{v}_i\right) + Re^{-1}\left(\nabla \boldsymbol{u}_{\mathrm{r}}, \nabla \mathbf{v}_i\right) + \left((\boldsymbol{u}_{\mathrm{r}} \cdot \nabla)\boldsymbol{u}_{\mathrm{r}}, \mathbf{v}_i\right) = 0, \tag{2.3}$$

where $(\cdot,\cdot)$ denotes the L^2 inner product and $\mathbf{X}_0^N := \mathrm{span}\{\boldsymbol{\varphi}_i\}_{i=1}^N$ is the ROM space.

Remark 2.1. We note that, in the case of fixed geometries, the divergence and pressure terms drop out of Section 2.2 because the ROM basis function is weakly divergence-free. For ROMs that include the pressure approximation, see, e.g., [2,4,26–28].

Remark 2.2. Because the zeroth mode has the prescribed flow rate, the remaining POD basis functions have zero flow rate, meaning that the test space $\mathbf{X}_0^N = \mathrm{span}\{\boldsymbol{\varphi}\}_{i=1}^N$ contains only members with zero flow-rate. Hence no additional forcing term is required for the ROM formulation because the forcing term drops out of (2.3):

$$\int_\Omega \mathbf{v}\cdot\mathbf{f}\, dV = f_x\left(\int_\Omega v_x dV\right) = 0, \quad \forall\, \mathbf{v} \in \mathbf{X}_0^N, \tag{2.4}$$

where f_x and v_x are the streamwise components of $\mathbf{f}$ and $\mathbf{v}$, respectively.

With (2.3), the following evolution equations are derived for the ROM basis coefficients $u_{\mathrm{r},j}$: For each $i = 1, \ldots, N$,

$$\sum_{j=1}^{N} B_{ij}\frac{du_{\mathrm{r},j}}{dt} = -\sum_{k=0}^{N}\sum_{j=0}^{N} C_{ikj}u_{\mathrm{r},k}(t)u_{\mathrm{r},j}(t) - \frac{1}{\mathrm{Re}}\sum_{j=0}^{N} A_{ij}u_{\mathrm{r},j}(t), \tag{2.5}$$

where A, B, and C represent the stiffness, mass, and advection operators, respectively, with entries

$$A_{ij} = \int_\Omega \nabla\boldsymbol{\varphi}_i : \nabla\boldsymbol{\varphi}_j\, dV, \quad B_{ij} = \int_\Omega \boldsymbol{\varphi}_i\cdot\boldsymbol{\varphi}_j\, dV, \quad C_{ikj} = \int_\Omega \boldsymbol{\varphi}_i\cdot(\boldsymbol{\varphi}_k\cdot\nabla)\boldsymbol{\varphi}_j\, dV. \tag{2.6}$$

Applying the BDFk/EXTk scheme to the reduced system (2.5), the fully discrete $N\times N$ reduced system can be written as follows:

$$H_{\mathrm{r,Re}}\,\underline{u}_{\mathrm{r}}^{l+1} = \underline{f}(\underline{u}_{\mathrm{r}}^{l};\mathrm{Re}), \tag{2.7}$$

for each timestep t^l, where $H_{\mathrm{r,Re}}$ and $\underline{f}(\underline{u}_{\mathrm{r}}^{l};\mathrm{Re})$ are the resulting Helmholtz matrix and right-hand side vector, and $\underline{u}_{\mathrm{r}}^{l}$ is the vector of ROM coefficients of $\boldsymbol{u}_{\mathrm{r}}^{l}$. We note that because the POD basis functions are orthonormal in the L^2 inner product, the ROM mass matrix B is an identity matrix.

3. ROM filters

In this section, we present the two ROM spatial filters that we use to construct the Reg-ROMs in Section 4: the classical differential filter (Section 3.1) and the higher-order algebraic filter (Section 3.2).

3.1. ROM differential filter (DF)

The first ROM spatial filter we investigate is the *ROM differential filter (DF)*: *Given* $\boldsymbol{u}_r = \sum_{j=1}^N u_{r,j}\boldsymbol{\varphi}_j(\mathbf{x})$, *find* $\overline{\boldsymbol{u}}_r(\mathbf{x}) = \sum_{j=1}^N \overline{u}_{r,j}\boldsymbol{\varphi}_j(\mathbf{x})$ *such that*

$$\left(\overline{\boldsymbol{u}}_{\mathrm{r}} - \delta^2 \Delta \overline{\boldsymbol{u}}_{\mathrm{r}}, \boldsymbol{\varphi}_i\right) = \left(\boldsymbol{u}_{\mathrm{r}}, \boldsymbol{\varphi}_i\right) \qquad \forall i = 1, \ldots N, \tag{3.1}$$

where δ is the filter radius. The DF weak form (3.1) yields the following linear system:

$$\left(\mathbb{I} + \delta^2 A\right) \underline{\overline{u}}_{\mathrm{r}} = \underline{u}_{\mathrm{r}}, \tag{3.2}$$

where $\underline{\overline{u}}_{\mathrm{r}}$ is the vector of ROM coefficients of $\overline{\boldsymbol{u}}_{\mathrm{r}}$, and $\mathbb{I}$ and A are the identity and ROM stiffness matrices, respectively.[1] We note that the expansions for $\boldsymbol{u}_{\mathrm{r}}$ and $\overline{\boldsymbol{u}}_{\mathrm{r}}$ do not include the zeroth mode, $\boldsymbol{\varphi}_0$. This is in contrast with the expansion (2.2), which does include $\boldsymbol{\varphi}_0$. The reason for not including $\boldsymbol{\varphi}_0$ in our expansions is that this strategy was shown in [16] to yield more accurate results.

We emphasize that (3.2) is a low-dimensional, $N \times N$ linear system, whose computational overhead is negligible. Thus, DF will be used in Section 4 to construct regularized ROMs that increase the ROM accuracy without significantly increasing the computational cost.

DF was used in large eddy simulation of turbulent flows with classical numerical discretizations [29,30]. In reduced order modeling, DF was used to develop Reg-ROMs for the Kuramoto-Sivashinsky equation [17], the NSE [16,18], and the quasi-geostrophic equations [31].

3.2. ROM higher-order algebraic filter (HOAF)

The second filter we investigate is the *higher-order algebraic filter (HOAF)*: *Given* $\boldsymbol{u}_r = \sum_{j=1}^{N} u_{r,j} \boldsymbol{\varphi}_j(\mathbf{x})$, *find* $\overline{\boldsymbol{u}}_r(\mathbf{x}) = \sum_{j=1}^{N} \overline{u}_{r,j} \boldsymbol{\varphi}_j(\mathbf{x})$ *such that*

$$H_m \underline{\overline{u}}_{\mathrm{r}} := \left(\mathbb{I} + \delta^{2m} A^m\right) \underline{\overline{u}}_{\mathrm{r}} = \underline{u}_{\mathrm{r}}, \tag{3.3}$$

where $\underline{\overline{u}}_{\mathrm{r}}$ is the vector of ROM basis coefficients of $\overline{\boldsymbol{u}}_{\mathrm{r}}$, and m is a positive integer. As motivated in Section 3.1, the expansions for $\boldsymbol{u}_{\mathrm{r}}$ and $\overline{\boldsymbol{u}}_{\mathrm{r}}$ do not include the zeroth mode, $\boldsymbol{\varphi}_0$. As explained in [32] in the Fourier setting, the role of the exponent m is to control the percentage of filtering at different wavenumbers: As m increases, the amount of filtering increases for the high wavenumber components and decreases for the low wavenumber components.

Just as the DF (3.2), the HOAF (3.3) is also a low-dimensional, $N \times N$ linear system. Thus, HOAF will also be used in Section 4 to develop accurate and efficient Reg-ROMs.

Remark 3.1 *(Notation Convention).* We also note that, for $m = 1$, the linear systems (3.3) and (3.2) are identical. Thus, DF can be considered a particular case of HOAF with $m = 1$. In what follows, for notation convenience, we will use the linear system (3.3) for both HOAF and DF, and we will only specify the m value to differentiate between the two: $m = 1$ for DF and $m \geq 2$ for HOAF.

Remark 3.2. The HOAF (3.3) was proposed in [33] and was based on the HOAF introduced by Fischer and Mullen [32] in a spectral element method (SEM) setting. We also note that the HOAF used in [33] has a δ scaling that is dimensionally inconsistent. This is rectified in (3.3).

Remark 3.3 *(Nomenclature).* In [33], the HOAF (3.3) was called the higher-order differential filter, to be consistent with the SEM nomenclature. In Appendix A.1, we show that the HOAF is related to, but slightly different from, the spatial discretization of a higher-order differential operator. (They are the same in the periodic case.) Thus, for clarity, in this paper we call the operator in (3.3) the high-order algebraic filter: The term A^m yields the high-order algebraic character of the operator (3.3), and the numerical investigation in Appendix A.2 shows that the operator (3.3) acts like a spatial filter.

A theoretical and numerical investigation of HOAF is performed in Appendix A.

4. Regularized reduced order models (Reg-ROMs)

In this section, we outline the three Reg-ROMs that we compare in our numerical investigation in Section 5: the Leray ROM (Section 4.1), the evolve-filter-relax ROM (Section 4.2), and the novel time relaxation ROM (Section 4.3). We also discuss similarities and differences between the EFR-ROM and TR-ROM. All three Reg-ROMs are developed based on the same principle: Use the ROM spatial filters presented in Section 3 to smooth (filter) terms in the standard G-ROM (2.3) and eliminate/alleviate the G-ROM's spurious numerical oscillations in under-resolved turbulent flow simulations. Furthermore, because the computational cost of the ROM spatial filters is low, the Reg-ROM computational overhead with respect to the G-ROM is negligible. Thus, Reg-ROMs are expected to yield more accurate results than the standard G-ROM without a significantly increase in the computational cost.

[1] In general, the inverse of the ROM mass matrix, B^{-1}, shows up in the DF definition. However, because the POD basis function is orthonormal in the L^2 norm, B is the identity matrix and ignored here to avoid confusion.

4.1. Leray ROM (L-ROM)

The *Leray ROM (L-ROM)* [19,16] modifies the standard G-ROM weak formulation (2.3) as follows: *Find* $\boldsymbol{u}_r$ *of the form* (2.2) *such that,* $\forall\, i = 1, \dots N$,

$$\left(\frac{\partial \boldsymbol{u}_{\mathrm{r}}}{\partial t}, \boldsymbol{\varphi}_i\right) + Re^{-1}\ \left(\nabla \boldsymbol{u}_{\mathrm{r}}, \nabla \boldsymbol{\varphi}_i\right) + \left((\overline{\boldsymbol{u}}_{\mathrm{r}} \cdot \nabla)\boldsymbol{u}_{\mathrm{r}}, \boldsymbol{\varphi}_i\right) = 0 \tag{4.1}$$

where $\overline{\boldsymbol{u}}_{\mathrm{r}}$ is the ROM velocity filtered with one of the ROM spatial filters introduced in Section 3, that is, DF (3.2) or HOAF (3.3).

L-ROM (4.1) is a Reg-ROM, because it leverages spatial filtering of the convective term of the G-ROM (i.e., it replaces $(\boldsymbol{u}_{\mathrm{r}} \cdot \nabla)\boldsymbol{u}_{\mathrm{r}}$ with $(\overline{\boldsymbol{u}}_{\mathrm{r}} \cdot \nabla)\boldsymbol{u}_{\mathrm{r}}$) in order to smooth out the G-ROM's spurious numerical oscillations in the convection-dominated, under-resolved regime.

In a more general setting, the Leray model was first introduced by Jean Leray in 1934 as a theoretical tool to prove the existence of weak solutions of the NSE [34]. As a computational tool, Leray regularization was first used in [35] as a stabilization strategy for under-resolved simulations of turbulent flows with classical numerical discretizations [30]. As noted by Guermond and co-authors [36,37], when a differential filter is used, the Leray model is similar to the NS-α model of Foias, Holm, and Titi [38]. Leray regularization was first used in the context of reduced order models in [17] for the Kuramoto-Sivashinsky equations. For fluid flows, L-ROM was first used in [16] for the 3D flow past a circular cylinder at $Re = 1{,}000$. Since then, L-ROM has been successfully used as a stabilization technique for various under-resolved flows: the NSE [39,40], the stochastic NSE [33,41], and the quasigeostrophic equations [31,42]. To our knowledge, L-ROM has never been used for the turbulent channel flow.

4.2. Evolve-filter-relax ROM (EFR-ROM)

The *evolve-filter-relax ROM (EFR-ROM)*, introduced in [16,33], consists of three steps. *Given the EFR-ROM approximation at the current time step,* $\boldsymbol{u}_r^n$*, find the EFR-ROM approximation at the next time step,* $\boldsymbol{u}_r^{n+1}$*, as follows:*

(I) *Evolve*: *Find* $\mathbf{w}_r$ *of the form* (2.2) *such that,* $\forall\, i = 1, \dots N$,

$$\left(\frac{\mathbf{w}_{\mathrm{r}}^{n+1} - \boldsymbol{u}_{\mathrm{r}}^{n}}{\Delta t}, \boldsymbol{\varphi}_i\right) + Re^{-1}\ \left(\nabla \boldsymbol{u}_{\mathrm{r}}^{n}, \nabla \boldsymbol{\varphi}_i\right) + \left((\boldsymbol{u}_{\mathrm{r}}^{n} \cdot \nabla)\boldsymbol{u}_{\mathrm{r}}^{n}, \boldsymbol{\varphi}_i\right) = 0 \tag{4.2}$$

(II) *Filter*: $$\mathbf{w}_{\mathrm{r}}^{n+1} \longmapsto \overline{\mathbf{w}_{\mathrm{r}}^{n+1}} \tag{4.3}$$

(III) *Relax*: $$\boldsymbol{u}_{\mathrm{r}}^{n+1} = (1-\chi)\,\mathbf{w}_{\mathrm{r}}^{n+1} + \chi\,\overline{\mathbf{w}}_{\mathrm{r}}^{n+1}. \tag{4.4}$$

In Step (I) of the EFR-ROM, called the evolve step, one step of the standard G-ROM time discretization is used to advance the current EFR-ROM approximation, $\boldsymbol{u}_{\mathrm{r}}^{n}$, to an intermediate EFR-ROM approximation, $\mathbf{w}_{\mathrm{r}}^{n+1}$. In Step (II), called the filter step, one of the two ROM spatial filters presented in Section 3 is used to filter the intermediate EFR-ROM approximation obtained in Step (I) and obtain a smoother approximation, without spurious numerical oscillations. Finally, in Step (III), called the relax step, the EFR-ROM approximation at the next time step is defined as a convex combination of the unfiltered intermediate EFR-ROM approximation obtained in Step (I), $\mathbf{w}_{\mathrm{r}}^{n+1}$, and its filtered counterpart, $\overline{\mathbf{w}}_{\mathrm{r}}^{n+1}$. The goal of the relax step is to adjust the amount of dissipation introduced in the filter step by using a relaxation parameter, $0 \le \chi \le 1$. By varying χ, one can produce a range of filter strengths, from no filtering at all ($\chi = 0$) to maximum filtering ($\chi = 1$). We note that the numerical investigation in [18] has shown that EFR-ROM is sensitive with respect to χ.

The EFR strategy is well-developed for classical numerical discretizations, for example, in the context of finite element method [30], spectral method [43] and spectral element method [32]. In reduced order modeling, the evolve-filter ROM was introduced in [16] and EFR-ROM was introduced in [33]. Since then, EFR-ROM has been developed in several directions, for example, the FOM-ROM consistency [18] and feedback control [44].

4.3. Time relaxation ROM (TR-ROM)

In this paper, we propose a new type of Reg-ROM: the *time-relaxation ROM (TR-ROM)*: *Find* $\boldsymbol{u}_r$ *of the form* (2.2) *such that,* $\forall\, i = 1, \dots N$,

$$\left(\frac{\partial \boldsymbol{u}_{\mathrm{r}}}{\partial t}, \boldsymbol{\varphi}_i\right) + \frac{1}{\mathrm{Re}}\left(\nabla \boldsymbol{u}_{\mathrm{r}}, \nabla \boldsymbol{\varphi}_i\right) + \left((\boldsymbol{u}_{\mathrm{r}} \cdot \nabla)\boldsymbol{u}_{\mathrm{r}}, \boldsymbol{\varphi}_i\right) + \left(\chi(\boldsymbol{u}_{\mathrm{r}} - \overline{\boldsymbol{u}}_{\mathrm{r}}), \boldsymbol{\varphi}_i\right) = 0, \tag{4.5}$$

where χ is the time-relaxation parameter, and $\overline{\boldsymbol{u}}_{\mathrm{r}}$ is the ROM velocity filtered with one of the ROM spatial filters introduced in Section 3, that is, DF (3.2) or HOAF (3.3).

Time-relaxation has been used as a regularization/stabilization strategy at a FOM level [30, Chapter 5] (see also [45–49]). To our knowledge, this is the first use of time-relaxation stabilization in the ROM context.

To understand the role of the time relaxation term, we consider $\boldsymbol{u}_{\mathrm{r}}$ as test function in TR-ROM (4.5), which is the usual approach in energy-stability analysis. With this choice, the last term on the right-hand side of (4.5) can be written as follows:

$$(\chi(\boldsymbol{u}_{\mathrm{r}} - \overline{\boldsymbol{u}}_{\mathrm{r}}), \boldsymbol{u}_{\mathrm{r}}) = \chi(\boldsymbol{u}_{\mathrm{r}}', \boldsymbol{u}_{\mathrm{r}}), \tag{4.6}$$

where $\boldsymbol{u}'_{\mathrm{r}}$ represents the fluctuations of $\boldsymbol{u}_{\mathrm{r}}$ around $\overline{\boldsymbol{u}}_{\mathrm{r}}$:

$$\boldsymbol{u}'_{\mathrm{r}} := \boldsymbol{u}_{\mathrm{r}} - \overline{\boldsymbol{u}}_{\mathrm{r}}. \tag{4.7}$$

Using the decomposition (4.7), the inner product in the time relaxation term (4.6) becomes:

$$(\boldsymbol{u}'_{\mathrm{r}}, \boldsymbol{u}_{\mathrm{r}}) = (\boldsymbol{u}'_{\mathrm{r}}, \boldsymbol{u}'_{\mathrm{r}}) + (\boldsymbol{u}'_{\mathrm{r}}, \overline{\boldsymbol{u}}_{\mathrm{r}}). \tag{4.8}$$

The first term on the right-hand side of (4.8) has a clear physical interpretation: It is a dissipative term acting only on the fluctuations. To understand the role played by the second term on the right-hand side of (4.8), we distinguish two cases:

Case 1: DF When DF is used to construct TR-ROM, we can use (3.1) and (4.7) to formally write the following:

$$\boldsymbol{u}'_{\mathrm{r}} = \boldsymbol{u}_{\mathrm{r}} - \overline{\boldsymbol{u}}_{\mathrm{r}} = -\delta^2 \Delta \overline{\boldsymbol{u}}_{\mathrm{r}}. \tag{4.9}$$

Using (4.9) in the last term in (4.8), we obtain the following:

$$\begin{aligned}(\boldsymbol{u}'_{\mathrm{r}}, \boldsymbol{u}_{\mathrm{r}}) &= (\boldsymbol{u}'_{\mathrm{r}}, \boldsymbol{u}'_{\mathrm{r}}) + (\boldsymbol{u}'_{\mathrm{r}}, \overline{\boldsymbol{u}}_{\mathrm{r}}) = (\boldsymbol{u}'_{\mathrm{r}}, \boldsymbol{u}'_{\mathrm{r}}) - \delta^2(\Delta \overline{\boldsymbol{u}}_{\mathrm{r}}, \overline{\boldsymbol{u}}_{\mathrm{r}}) \\ &\overset{\overline{\boldsymbol{u}}_{\mathrm{r}}=0 \text{ on } \partial\Omega}{=} (\boldsymbol{u}'_{\mathrm{r}}, \boldsymbol{u}'_{\mathrm{r}}) + \delta^2(\nabla \overline{\boldsymbol{u}}_{\mathrm{r}}, \nabla \overline{\boldsymbol{u}}_{\mathrm{r}}) \\ &\overset{(4.9)}{=} \delta^4(\Delta \overline{\boldsymbol{u}}_{\mathrm{r}}, \Delta \overline{\boldsymbol{u}}_{\mathrm{r}}) + \delta^2(\nabla \overline{\boldsymbol{u}}_{\mathrm{r}}, \nabla \overline{\boldsymbol{u}}_{\mathrm{r}}).\end{aligned} \tag{4.10}$$

Equality (4.10) shows that the TR-ROM term in (4.6) is a dissipative term that has two components: The first component can be interpreted either as a dissipation term acting on the fluctuations or as a hyperviscosity term acting on the averages. The second component is a diffusion term acting on the averages.

Case 2: HOAF The HOAF is a high-order algebraic filter (3.3) that does not have a direct interpretation as a differential operator (primarily because of ambiguity related to boundary conditions; see discussion in Appendix A). When HOAF (3.3) is used to construct TR-ROM, we cannot use the above approach to interpret the TR-ROM term because the HOAF cannot be easily written in terms of the spatial derivative operators. However, we can (optimistically) expect behavior of the following form for a $2m$th-order filter,

$$(\boldsymbol{u}'_{\mathrm{r}}, \boldsymbol{u}_{\mathrm{r}}) = (\boldsymbol{u}'_{\mathrm{r}}, \boldsymbol{u}'_{\mathrm{r}}) + \delta^{2m}(\nabla^m \overline{\boldsymbol{u}}_{\mathrm{r}}, \nabla^m \overline{\boldsymbol{u}}_{\mathrm{r}}) = \delta^{4m}(\Delta^m \overline{\boldsymbol{u}}_{\mathrm{r}}, \Delta^m \overline{\boldsymbol{u}}_{\mathrm{r}}) + \delta^{2m}(\nabla^m \overline{\boldsymbol{u}}_{\mathrm{r}}, \nabla^m \overline{\boldsymbol{u}}_{\mathrm{r}}), \tag{4.11}$$

which has the same physical interpretation as that in the DF case and which is, in fact, exact if the domain is periodic in all directions.

Remark 4.1. We note that, at the FOM level, various levels of spatial filtering in the time relaxation term have been obtained by using approximate deconvolution strategies of different orders [30, Chapter 5]. In the new TR-ROM, we employ a different strategy and adjust the HOAF order in order to control the amount of filtering in TR-ROM. Although the zeroth order deconvolution and the DF yield identical models [30], the higher-order approximate deconvolution methods and the HOAF yield different time relaxation models.

A numerical comparison of DF and HOAF and an investigation of their effect on the TR-ROM results is performed in Section 5.

Remark 4.2. Note that in [50], the author shows that with implicit time discretization, the evolve-filter-relax method yields the implicit discretization of the Navier-Stokes equations with an explicitly treated time-relaxation term. One can also use the same derivation to show that EFR-ROM is equivalent to TR-ROM with an explicitly treated time-relaxation term. Next, we show that with a semi-implicit time discretization (which is used in the numerical investigation in Section 5), the TR-ROM is different from the EFR-ROM. For simplicity, we consider BDF1/EXT1 for the semi-implicit scheme. We note, however, that the same conclusion holds for BDFk/EXTk for $k \geq 2$. We begin with EFR-ROM at time t^{l+1}:

$$\frac{\underline{v}_r^{l+1} - \underline{u}_r^l}{\Delta t} + A\underline{v}^{l+1} = -C(\underline{u}_r^l)\underline{u}_r^l \tag{4.12}$$

$$H_m \overline{\underline{v}}_r^{l+1} = \underline{v}_r^{l+1} \tag{4.13}$$

$$\underline{u}_r^{l+1} = (1-\chi)\underline{v}_r^{l+1} + \chi \overline{\underline{v}}_r^{l+1}, \tag{4.14}$$

with the notation introduced in Section 2.2. Next, we consider the evolve step of EFR-ROM at time t^{l+2},

$$\frac{\underline{v}_r^{l+2} - \underline{u}_r^{l+1}}{\Delta t} + A\underline{v}^{l+2} = -C(\underline{u}_r^{l+1})\underline{u}_r^{l+1}. \tag{4.15}$$

With the relationship in the relax step, $\underline{u}_r^{l+1} = (1-\chi)\underline{v}_r^{l+1} + \chi \overline{\underline{v}}_r^{l+1}$, the evolve step at time t^{l+2} becomes

$$\frac{\underline{v}_r^{l+2} - \left[(1-\chi)\underline{v}_r^{l+1} + \chi \overline{\underline{v}}_r^{l+1}\right]}{\Delta t} + A\underline{v}^{l+2} = -C\left((1-\chi)\underline{v}_r^{l+1} + \chi \overline{\underline{v}}_r^{l+1}\right)\left((1-\chi)\underline{v}_r^{l+1} + \chi \overline{\underline{v}}_r^{l+1}\right). \tag{4.16}$$

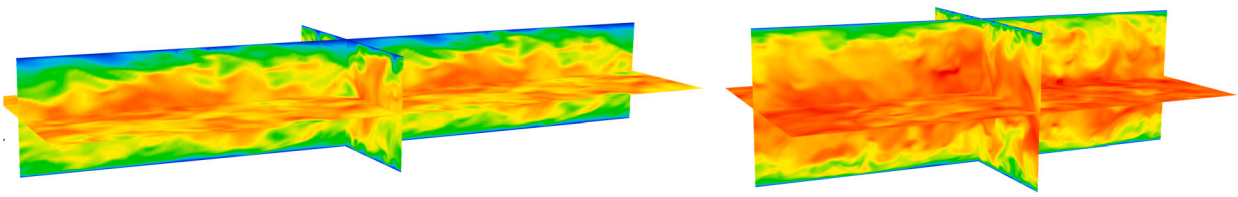

Fig. 5.1. Turbulent channel flow: FOM velocity magnitude snapshots at $\mathrm{Re}_\tau = 180$ (left) and 395 (right).

Rearranging the left-handed side in (4.16), the evolve step becomes

$$\frac{\underline{v}_r^{l+2} - \underline{v}_r^{l+1}}{\Delta t} + A\underline{v}^{l+2} = -C\left((1-\chi)\underline{v}_r^{l+1} + \chi\overline{\underline{v}}_r^{l+1}\right)\left((1-\chi)\underline{v}_r^{l+1} + \chi\overline{\underline{v}}_r^{l+1}\right) - \frac{\chi}{\Delta t}\left(\underline{v}_r^{l+1} - \overline{\underline{v}}_r^{l+1}\right). \tag{4.17}$$

Comparing (4.17) to the TR-ROM at time t^{l+2} with BDF1/EXT1,

$$\frac{\underline{v}_r^{l+2} - \underline{v}_r^{l+1}}{\Delta t} + A\underline{v}^{l+2} = -C(\underline{v}_r^{l+1})\underline{v}_r^{l+1} - \chi\left(\underline{v}_r^{l+1} - \overline{\underline{v}}_r^{l+1}\right), \tag{4.18}$$

we notice that EFR-ROM is different from TR-ROM because of the terms highlighted in red[2], which are the explicit treatment of the advection term. This could explain the difference between the optimal χ for EFR-ROM and the optimal χ for TR-ROM reported in Section 5. Specifically, although the two χ values seem to be related by a $1/\Delta t$ factor, the red terms in (4.17), which are not present in (4.18), make this relationship more complex. We note that the EFR-ROM and TR-ROM are different as long as one has an explicit term that depends on the ROM solution. Hence, EFR-ROM and TR-ROM are different for any semi-implicit or explicit schemes.

5. Numerical results

In this section, we present numerical results for the three Reg-ROMs outlined in Section 4 in the simulation of the turbulent channel flow. Specifically, we compare the L-ROM (4.1), the EFR-ROM (4.4), and the novel TR-ROM (4.5). For comparison purposes, we also investigate the standard G-ROM (2.3). As a benchmark for our comparison, we use the FOM results, which correspond to a DNS of the turbulent channel flow. We compare the three Reg-ROMs, the G-ROM, and the ROM projection in terms of their accuracy with respect to the FOM benchmark. We expect the three Reg-ROMs to yield significantly more accurate results than the standard G-ROM. We also note that, as mentioned in Section 3, the computational cost of the three Reg-ROMs is similar, and is on the same order of magnitude as the G-ROM cost.

The rest of this section is organized as follows: In Section 5.1, we present the FOM computational setting, which is then leveraged to construct the ROMs. In Section 5.2, we quantify the computational cost of the G-ROM and Reg-ROMs. In Section 5.3, we define the criteria used to evaluate the ROM performance. In Section 5.3.1 we outline the efficient offline-online decomposition of the Reynolds stresses that are used in our numerical investigation. We also outline the ROM projection for the Reynolds stresses, which is used as a benchmark in our numerical investigation. Next, we present numerical results of the Reg-ROM comparison for two regimes: In Section 5.4, we present results for the reproduction regime, i.e., when the ROMs are tested on the training time interval. In Section 5.5, we present results for the predictive regime, i.e., when the ROMs are tested on a time interval that is different from the training interval. In Section 5.6, we perform a numerical investigation of the Reg-ROMs' sensitivity with respect to the following parameters: (i) the time interval; (ii) the relaxation parameter, χ; and (iii) the filter radius, δ. The objective of this sensitivity study is to determine which of the three Reg-ROMs is more robust with respect to parameter changes. Finally, in Section 5.7, we compare the performance of Reg-ROMs with an eddy viscosity approach, the mixing-length ROM (ML-ROM).

5.1. FOM computational setting

In this section, we present the computational setting for the FOM, which has two main goals: (i) to generate the snapshots used in Section 5.2 to construct the ROMs; and (ii) to serve as a benchmark in the ROM numerical investigation. Our FOM is a DNS of the turbulent channel flow at $\mathrm{Re}_\tau = 180$ and $\mathrm{Re}_\tau = 395$ using the spectral element code Nek5000/RS [51,52]. The friction Reynolds number Re_τ is based on the friction velocity u_τ at the wall, channel half-height h, and the fluid kinematic viscosity ν, with $u_\tau = \sqrt{\tau_w}/\rho$ determined using the wall shear stress, τ_w, and the fluid density, ρ. FOM velocity magnitude snapshots for both Re_τ are shown in Fig. 5.1.

For $\mathrm{Re}_\tau = 180$, we follow the setup in [5], in which the streamwise (i.e., the x-direction) and spanwise (i.e., the z-direction) lengths of the channel are set to $4\pi h$ and $4\pi h/3$, respectively, and the channel half-height is set to $h = 1$. We consider twice as many grid points as in [5], with $E = 5,832$ elements (an array of $18 \times 18 \times 18$ elements in the $x \times y \times z$ directions), of order $q = 9$, for a total of $\mathcal{N} \approx 4.3$ million grid points. FOM statistics are collected over 1,000 convection time units (CTUs) and compared against the

[2] For interpretation of the references to colour please refer to the web version of this article.

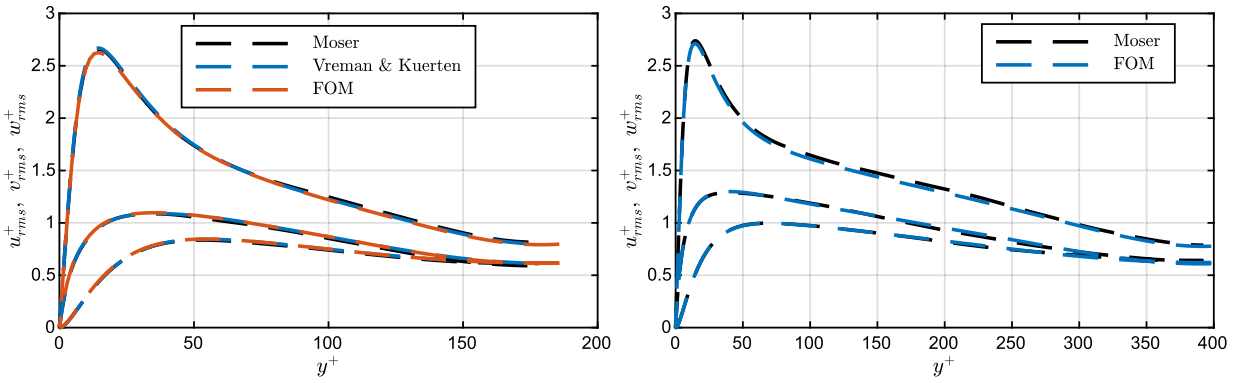

Fig. 5.2. FOM 2nd order statistics u^+_{rms}, v^+_{rms}, and w^+_{rms} validation: (Left) $\mathrm{Re}_\tau = 180$, comparison with [5,53]. (Right) $\mathrm{Re}_\tau = 395$, comparison with [6]. (For interpretation of the colors in the figure(s), the reader is referred to the web version of this article.)

following two databases: (i) data in [53], which is collected over 3140 CTUs and has 14.2 million grid points; and (ii) data in [5], which has 2.1 million grid points.[3]

For $\mathrm{Re}_\tau = 395$, we follow the setup in [6], in which the streamwise and spanwise lengths of the channel are set to 2π and π, respectively, and the channel half-height is set to $h = 1$. We consider twice as many grid points as in [6], with $E = 26,244$ elements (an array of $36 \times 27 \times 27$ elements in the $x \times y \times z$ directions), of order $q = 9$, for a total of $\mathcal{N} \approx 20$ million grid points. FOM statistics are collected over 1500 CTUs and compared against the data in [6], which has 9.5 million grid points.

For both Reynolds numbers, the FOM is run until the solution reaches a statistically steady state prior to gathering statistics. To validate our FOM, in Fig. 5.2, for both Re_τ, we compare the FOM with the reference data with respect to the 2nd-order turbulent statistics u^+_{rms}, v^+_{rms}, and w^+_{rms} (in wall-units). For both Re_τ, we observe that the FOM 2nd order statistics are in good agreement with the published results.

5.2. ROM computational setting

The POD basis functions are constructed using $K = 2{,}000$ uniformly distributed snapshots in the statistically steady state region, which spans 500 CTUs for $\mathrm{Re}_\tau = 180$, and 1,000 CTUs for $\mathrm{Re}_\tau = 395$.

For each Re_τ, we compare the ROM performance for different ROM parameters in both the reproduction and the predictive regimes. The ROM offline phase, which includes the construction of the POD basis functions and reduced operators, is performed using NekROM [54] on the UIUC cluster Delta. The ROM online phase, which includes loading the reduced operators and solving the ROM systems, is performed using Matlab on a workstation.

Next, we quantify the computational cost of the G-ROM and Reg-ROMs. To this end, the fully discrete $N \times N$ G-ROM system (2.7) at timestep t^l solved using the BDFk/EXTk scheme is written as

$$\text{(G-ROM)} \quad \left(\frac{\beta_0}{\Delta t} B + \mathrm{Re}\, A\right) \underline{u}_{\mathrm{r}}^l = -\sum_{i=1}^{k} \alpha_i C(\underline{u}_{\mathrm{r}}^{l-i}) \underline{u}_{\mathrm{r}}^{l-i} - B \sum_{i=1}^{k} \frac{\beta_i}{\Delta t} \underline{u}_{\mathrm{r}}^{l-i} - \mathrm{Re}\, \underline{a}_0, \tag{5.1}$$

where A, B, and C are the ROM operators defined in (2.6), and α_i and β_i are the respective BDFk/EFTk coefficients. For time step $l > 3$, the computational cost of advancing (5.1) is dominated by the application of the rank-3 advection tensor, C, which requires $\mathcal{O}(N^3)$ operations and memory references. The remaining terms require $\mathcal{O}(N^2)$ operations or less. For the first three time steps, in addition to the tensor contraction, one needs to compute the Cholesky factorization of the system matrix, that is $(\frac{\beta_0}{\Delta t} B + \mathrm{Re}\, A) = R^T R$, which requires $N^3/2$ operations. Note that with the Cholesky factorization, two triangular systems are solved at each time step, but the corresponding cost is only $\mathcal{O}(N^2)$.

The fully discrete $N \times N$ systems of the three Reg-ROMs (4.1) at time step t^l are listed below:

$$\text{(L-ROM)} \quad \begin{cases} \left(\frac{\beta_0}{\Delta t} B + \mathrm{Re}\, A\right) \underline{u}_{\mathrm{r}}^l = -\sum_{i=1}^{k} \alpha_i C(\overline{\underline{u}}_{\mathrm{r}}^{l-i}) \underline{u}_{\mathrm{r}}^{l-i} - B \sum_{i=1}^{k} \frac{\beta_i}{\Delta t} \underline{u}_{\mathrm{r}}^{l-i} - \mathrm{Re}\, \underline{a}_0 \\ \left(I + \delta^{2m} (B^{-1} A)^m\right) \overline{\underline{u}}_{\mathrm{r}}^{l-i} = \underline{u}_{\mathrm{r}}^{l-i}. \end{cases} \tag{5.2}$$

$$\text{(EFR-ROM)} \quad \begin{cases} \left(\frac{\beta_0}{\Delta t} B + \mathrm{Re}\, A\right) \underline{w}_{\mathrm{r}}^l = -\sum_{i=1}^{k} \alpha_i C(\underline{u}_{\mathrm{r}}^{l-i}) \underline{u}_{\mathrm{r}}^{l-i} - B \sum_{i=1}^{k} \frac{\beta_i}{\Delta t} \underline{u}_{\mathrm{r}}^{l-i} - \mathrm{Re}\, \underline{a}_0 \\ \left(I + \delta^{2m} (B^{-1} A)^m\right) \overline{\underline{w}}_{\mathrm{r}}^l = \underline{w}_{\mathrm{r}}^l \\ \underline{u}_{\mathrm{r}}^l = (1 - \chi) \underline{w}_{\mathrm{r}}^l + \chi \overline{\underline{w}}_{\mathrm{r}}^l. \end{cases} \tag{5.3}$$

[3] We couldn't find out how long the statistics are collected for in [5].

$$\text{(TR-ROM)} \quad \begin{cases} \left(\frac{\beta_0}{\Delta t} B + \mathrm{Re}\, A\right) \underline{u}_{\mathrm{r}}^{l} = -\sum_{i=1}^{k} \alpha_i \left[C(\underline{u}_{\mathrm{r}}^{l-i}) \underline{u}_{\mathrm{r}}^{l-i} + \chi B(\underline{u}_{\mathrm{r}}^{l-i} - \overline{\underline{u}}_{\mathrm{r}}^{l-i}) \right] - B \sum_{i=1}^{k} \frac{\beta_i}{\Delta t} \underline{u}_{\mathrm{r}}^{l-i} - \mathrm{Re}\, \underline{a}_0 \\ \left(I + \delta^{2m} (B^{-1}A)^m\right) \overline{\underline{u}}_{\mathrm{r}}^{l-i} = \underline{u}_{\mathrm{r}}^{l-i}. \end{cases} \tag{5.4}$$

ROM filtering is required in all three Reg-ROMs (5.2–5.4). However, before time advancing the Reg-ROMs, one can precompute the Cholesky factorization of the filter operator, that is $(I + \delta^{2m}(B^{-1}A)^m) = R^T R$, which requires $N^3/2$ operations. Then, at each time step, the vector of filtered ROM coefficients, $\overline{\underline{u}}$, is computed by solving two triangular systems that cost only $\mathcal{O}(N^2)$.

In summary, given the total number of time steps, N_t, the computational cost of the G-ROM, L-ROM, EFR-ROM, and TR-ROM is $\mathcal{O}(3N^3/2 + N_t N^3) + \mathcal{O}(3N_t N^2) + \mathcal{O}(N_t N)$, $\mathcal{O}(4N^3/2 + N_t N^3) + \mathcal{O}(5N_t N^2) + \mathcal{O}(N_t N)$, $\mathcal{O}(4N^3/2 + N_t N^3) + \mathcal{O}(5N_t N^2) + \mathcal{O}(2N_t N)$, and $\mathcal{O}(4N^3/2 + N_t N^3) + \mathcal{O}(6N_t N^2) + \mathcal{O}(2N_t N)$, respectively. The computational cost of advancing the three Reg-ROMs is similar, and the differences are only in the low-order terms. The computational cost of the G-ROM is the lowest, but in the same order of magnitude as the cost of Reg-ROMs. The reason is that, for all the ROMs, the computational cost is dominated by the computation of the advection tensor.

5.3. Criteria

To evaluate the ROM performance, we use the FOM data as a benchmark, and the streamwise Reynolds normal stress $\langle u'u' \rangle$ and the Reynolds shear stress $\langle u'v' \rangle$, which are the two dominant terms in the Reynolds stress tensor, as criteria for accuracy evaluation. Specifically, we use the following formulas:

$$\varepsilon_{u'u'} := \frac{\|\langle u'u' \rangle_{\mathrm{r}} - \langle u'u' \rangle\|_2}{\|\langle u'u' \rangle\|_2}, \quad \varepsilon_{u'v'} := \frac{\|\langle u'v' \rangle_{\mathrm{r}} - \langle u'v' \rangle\|_2}{\|\langle u'v' \rangle\|_2}, \tag{5.5}$$

where $\langle u'u' \rangle$ and $\langle u'v' \rangle$ are the FOM Reynolds stresses, and $\langle u'u' \rangle_{\mathrm{r}}$, $\langle u'v' \rangle_{\mathrm{r}}$ are the ROM Reynolds stresses. The FOM Reynolds stresses are defined as follows:

$$\langle u'u' \rangle := \left\langle (u - \langle u \rangle)^2 \right\rangle = \left\langle u^2 - 2u\langle u \rangle + \langle u \rangle^2 \right\rangle = \langle u^2 \rangle - \langle u \rangle^2, \tag{5.6}$$

$$\langle u'v' \rangle := \left\langle (u - \langle u \rangle)(v - \langle v \rangle) \right\rangle = \left\langle uv - u\langle v \rangle - v\langle u \rangle + \langle u \rangle \langle v \rangle \right\rangle = \langle uv \rangle - \langle u \rangle \langle v \rangle. \tag{5.7}$$

The ROM Reynolds stresses are computed using (5.6)-(5.7), but with the ROM approximated solution (2.2):

$$\langle u'u' \rangle_{\mathrm{r}} := \langle u_{\mathrm{r}}^2 \rangle - \langle u_{\mathrm{r}} \rangle^2, \quad \langle u'v' \rangle_{\mathrm{r}} := \langle u_{\mathrm{r}} v_{\mathrm{r}} \rangle - \langle u_{\mathrm{r}} \rangle \langle v_{\mathrm{r}} \rangle. \tag{5.8}$$

In this paper, an angle bracket $\langle \cdot \rangle$ indicates an average over x, z, and t, and is defined as:

$$\langle u \rangle(y) = \frac{1}{T L_x L_x} \sum_{x,z,t} u(x, y, z, t), \tag{5.9}$$

where T is the length of the time interval, L_x is the dimension of the computational domain in the x-direction, L_z is the dimension of the computational domain in the z-direction, u is a scalar field, and a prime indicates perturbation from this average.

We note that using (5.8) to compute ROM Reynolds stresses requires accessing the POD basis functions and reconstructing the ROM quantities $\langle u_{\mathrm{r}}^2 \rangle$, $\langle u_{\mathrm{r}} v_{\mathrm{r}} \rangle$, $\langle u_{\mathrm{r}} \rangle^2$, and $\langle u_{\mathrm{r}} \rangle \langle v_{\mathrm{r}} \rangle$, which scale with the FOM dimension, $\mathcal{N}$. Thus, using (5.8) to compute $\langle u'u' \rangle_{\mathrm{r}}$ and $\langle u'v' \rangle_{\mathrm{r}}$ is inefficient.

5.3.1. Efficient offline-online Reynolds-stress evaluation

To efficiently compute the ROM Reynolds stresses, we use an alternative approach, based on an offline-online splitting. First, we rewrite (5.8) with the POD expansion:

$$\begin{aligned} \langle u'u' \rangle_{\mathrm{r}} &= \left\langle \left(\sum_{j=0}^{N} u_{\mathrm{r},j}(t)\varphi_j\right)\left(\sum_{k=0}^{N} u_{\mathrm{r},k}(t)\varphi_k\right) \right\rangle - \left\langle \sum_{j=0}^{N} u_{\mathrm{r},j}(t)\varphi_j \right\rangle^2, \\ &= \sum_{j=0}^{N}\sum_{k=0}^{N} \left\langle u_{\mathrm{r},j}(t) u_{\mathrm{r},k}(t) \varphi_j \varphi_k \right\rangle - \left(\sum_{j=0}^{N} \left\langle u_{\mathrm{r},j}(t)\varphi_j \right\rangle \right) \left(\sum_{k=0}^{N} \left\langle u_{\mathrm{r},k}(t)\varphi_k \right\rangle \right), \\ &= \sum_{j=0}^{N}\sum_{k=0}^{N} \langle u_{\mathrm{r},j} u_{\mathrm{r},k} \rangle_t \langle \varphi_j \varphi_k \rangle_{xz} - \sum_{j=0}^{N}\sum_{k=0}^{N} \langle u_{\mathrm{r},j} \rangle_t \langle u_{\mathrm{r},k} \rangle_t \langle \varphi_j \rangle_{xz} \langle \varphi_k \rangle_{xz}, \end{aligned} \tag{5.10}$$

where φ_j and φ_k are the POD basis functions in the streamwise direction, and $\langle \cdot \rangle_t$ and $\langle \cdot \rangle_{xz}$ are the average operators in t and the x-z plane. Then, in the offline stage, for each y coordinate, we compute and store $\langle \varphi_j \varphi_k \rangle_{xz}$ and $\langle \varphi_j \rangle_{xz}$ for all $j,\ k = 0, \ldots, N$. Finally, in the online stage, we compute $\langle u_{\mathrm{r},j} u_{\mathrm{r},k} \rangle_t$ and $\langle u_{\mathrm{r},j} \rangle_t$ for all $j,\ k = 0, \ldots, N$. Thus, to construct the ROM streamwise Reynolds normal stress $\langle u'u' \rangle_{\mathrm{r}}$ at a given point y^*, we use (5.10), which is independent of $\mathcal{N}$ and, thus, does not significantly increase the computational cost. The offline-online splitting for the ROM Reynolds shear stress $\langle u'v' \rangle_{\mathrm{r}}$ can be derived similarly.

We also assess the ROM performance with the ROM-projection Reynolds stresses $\langle u'u' \rangle_{\mathrm{Proj}}$ and $\langle u'v' \rangle_{\mathrm{Proj}}$:

$$\langle u'u' \rangle_{\mathrm{Proj}} := \langle u_{\mathrm{Proj}}^2 \rangle - \langle u_{\mathrm{Proj}} \rangle^2, \tag{5.11}$$

$$\langle u'v' \rangle_{\text{Proj}} := \langle u_{\text{Proj}} v_{\text{Proj}} \rangle - \langle u_{\text{Proj}} \rangle \langle v_{\text{Proj}} \rangle, \tag{5.12}$$

where the solution projected onto the reduced space is defined as:

$$\boldsymbol{u}_{\text{Proj}} = \boldsymbol{\varphi}_0 + \sum_{j=0}^{N} \tilde{u}_{\text{Proj},j} \boldsymbol{\varphi}_j(\mathbf{x}), \quad \text{and} \quad \tilde{u}_{\text{Proj},j} = (\boldsymbol{\varphi}_j, \boldsymbol{u} - \boldsymbol{\varphi}_0). \tag{5.13}$$

The ROM-projection Reynolds stress can be computed using (5.10) but with $\langle \tilde{u}_{\text{Proj},j} \tilde{u}_{\text{Proj},j} \rangle_t$ and $\langle \tilde{u}_{\text{Proj},j} \rangle_t$ quantities, and is used to compute the error $\varepsilon_{u'v'}$ (5.5). The ROM projection represents the best theoretical approximation of the training data in the given ROM space, and we use it as a benchmark to assess the three Reg-ROMs.

5.4. Reproduction regime

In this section, we perform a numerical investigation of the three Reg-ROMs: L-ROM (Section 4.1), EFR-ROM (Section 4.2), and the new TR-ROM (Section 4.3) in the reproduction regime, i.e., in the time interval in which the snapshots were collected, at $\text{Re}_\tau = 180$ (Section 5.4.1) and $\text{Re}_\tau = 395$ (Section 5.4.2). For comparison purposes, we include results for the G-ROM (Section 2.2) and the ROM projection, which represents the best theoretical approximation of the FOM solution in the given ROM space. The Reg-ROM accuracy is expected to be significantly higher than the G-ROM accuracy. To quantify the ROM accuracy, we use $\varepsilon_{u'u'}$ and $\varepsilon_{u'v'}$, which are the relative ℓ^2 errors of the streamwise Reynolds normal stress $\langle u'u' \rangle$ and Reynolds shear stress $\langle u'v' \rangle$ defined in (5.5).

In our numerical investigation, we also consider the following parameters: For all the ROMs, we utilize 10 values for the ROM dimension, $N \in \{10, 20, \ldots, 90, 100\}$. For each Reg-ROM, we use four HOAF orders: $m = 1$ (which corresponds to the classical DF (3.2)) and $m = 2, 3, 4$ (which correspond to the HOAF (3.3)). For each N and m value, the values of the filter radius, δ, are chosen as follows: For EFR-ROM and TR-ROM, 10, 25, and 10 δ values are uniformly sampled from the intervals $[0.001,\ 0.01]$, $[0.01, 0.1]$, and $[0.1, 1]$, respectively. This yields a total of 43 values for δ from the interval $[0.001,\ 1]$. In addition, we choose 4 uniformly sampled values for the relaxation parameter, χ, in the interval $[\Delta t = 0.005,\ 1]$. We choose this χ range because $\chi = \mathcal{O}(\Delta t)$ is commonly used in EFR-ROM simulations [55,18]. For L-ROM, we uniformly sample 15 additional δ values from the interval $[0.1,\ 0.2]$, which yields a total of 56 values for δ from the interval $[0.001,\ 1]$ for $\text{Re}_\tau = 180$. For $\text{Re}_\tau = 395$, 30 additional δ values are uniformly sampled from the interval $[0.1,\ 0.3]$, which yields a total of 69 values for δ.

We emphasize that, in our Reg-ROM numerical investigation, we use four parameters: the ROM dimension, N, the filter order, m, the filter radius, δ, and (for EFR-ROM and TR-ROM) the relaxation parameter, χ. Thus, to ensure a clear comparison of the three Reg-ROMs, we fix the δ and χ parameters to their optimal values (i.e., the values that yield the most accurate Reynolds shear stress $\langle u'v' \rangle$ for each Reg-ROM), and plot $\varepsilon_{u'v'}$ for all the parameter values for N and m. We note that we show only $\varepsilon_{u'v'}$ results for the following two reasons: (i) We find that $\varepsilon_{u'u'}$ behaves similarly to $\varepsilon_{u'v'}$. Specifically, $\varepsilon_{u'u'}$ is generally smaller than $\varepsilon_{u'v'}$ at $\text{Re}_\tau = 180$, and similar to $\varepsilon_{u'v'}$ at $\text{Re}_\tau = 395$. (ii) In turbulent channel flow investigations, the approximation of the Reynolds shear stress $\langle u'v' \rangle$ is more challenging than the approximation of streamwise Reynolds normal stress $\langle u'u' \rangle$. For the $\varepsilon_{u'u'}$ results, we refer readers to the dissertation [56]. For completeness, in the sensitivity study in Section 5.6, we include Reg-ROM results for all the δ and χ values.

Finally, in Section 5.4.3, we present a summary of the Reg-ROM comparison in the reproduction regime.

5.4.1. $\text{Re}_\tau = 180$

In Fig. 5.3, we plot the relative ℓ^2 error $\varepsilon_{u'v'}$ (5.5) for different ROM dimensions, N, and filter orders, m, for the G-ROM, the ROM projection, and the three Reg-ROMs at $\text{Re}_\tau = 180$. For the ROM projection, two errors are shown. For the error labeled as "ROM proj with snap", $\langle u'v' \rangle_{\text{Proj}}$ is computed with 2,000 FOM data points (snapshot data). For the error labeled as "ROM proj with FOM", $\langle u'v' \rangle_{\text{Proj}}$ is computed with 10,000 FOM data points. Note that to compute the second error, we rerun the FOM simulation, project the DNS data onto the reduced space on the fly, and compute its associated $\langle u_{\text{r},j} u_{\text{r},k} \rangle_t$ and $\langle u_{\text{r},j} \rangle_t$ for all $j,\ k = 0, \ldots, N$. The error $\varepsilon_{u'v'}$ of the ROM projection with the 2,000 FOM data points is expected to be smaller than the error with the 10,000 FOM data points, because the POD basis set is constructed using a sparser data set. For each Reg-ROM, the error is plotted for the optimal δ values and, for EFR-ROM and TR-ROM, for the optimal χ values.

Fig. 5.3a displays the G-ROM results. This plot shows that, for all N values, the G-ROM results are very inaccurate. Even with $N = 100$, G-ROM fails to reconstruct $\langle u'v' \rangle$ with an error of $\mathcal{O}(10^5)$.

Fig. 5.3b displays the L-ROM results for each N and m with the optimal δ, along with the results of the ROM projection for comparison purposes. For $N \geq 30$, $m = 1$ yields the most accurate results, achieving an error of 15% for $N = 40$. Conversely, for $N \leq 20$, a higher-order filter yields better results. Specifically, $m = 4$ achieves an error of 31% for $N = 10$ and $m = 2$ achieves an error of 23% for $N = 20$. With the exception of $(N, m) = (50, 4)$, L-ROM is more accurate than the ROM projection.

Fig. 5.3c displays the EFR-ROM results for each N and m with the optimal χ and δ values, along with the results of the ROM projection for comparison purposes. For $N \geq 40$, $m = 1$ yields the most accurate results, achieving an error of 27% for $N = 90$. Conversely, for $N \leq 30$, a higher-order filter yields better results. Specifically, $m = 2$ achieves an error of 28% and 40% for $N = 10$ and $N = 30$, respectively. Additionally, $m = 3$ achieves an error of 45% for $N = 20$. EFR-ROM is more accurate than the ROM projection for all N with $m = 1,\ 2,\ 3$. With $m = 4$, it is only more accurate than the ROM projection for $N \leq 30$.

Fig. 5.3d displays the TR-ROM results for each N and m with the optimal χ and δ values, along with the results of the ROM projection for comparison purposes. For $20 \leq N \leq 90$, $m = 1$ yields the most accurate results, achieving an error of 22% for $N = 70$. For $N = 10$ and $N = 100$, $m = 3$ yields the most accurate results, achieving an error of 29% and 28%, respectively. In addition, TR-ROM is more accurate than the ROM projection for all N and m values.

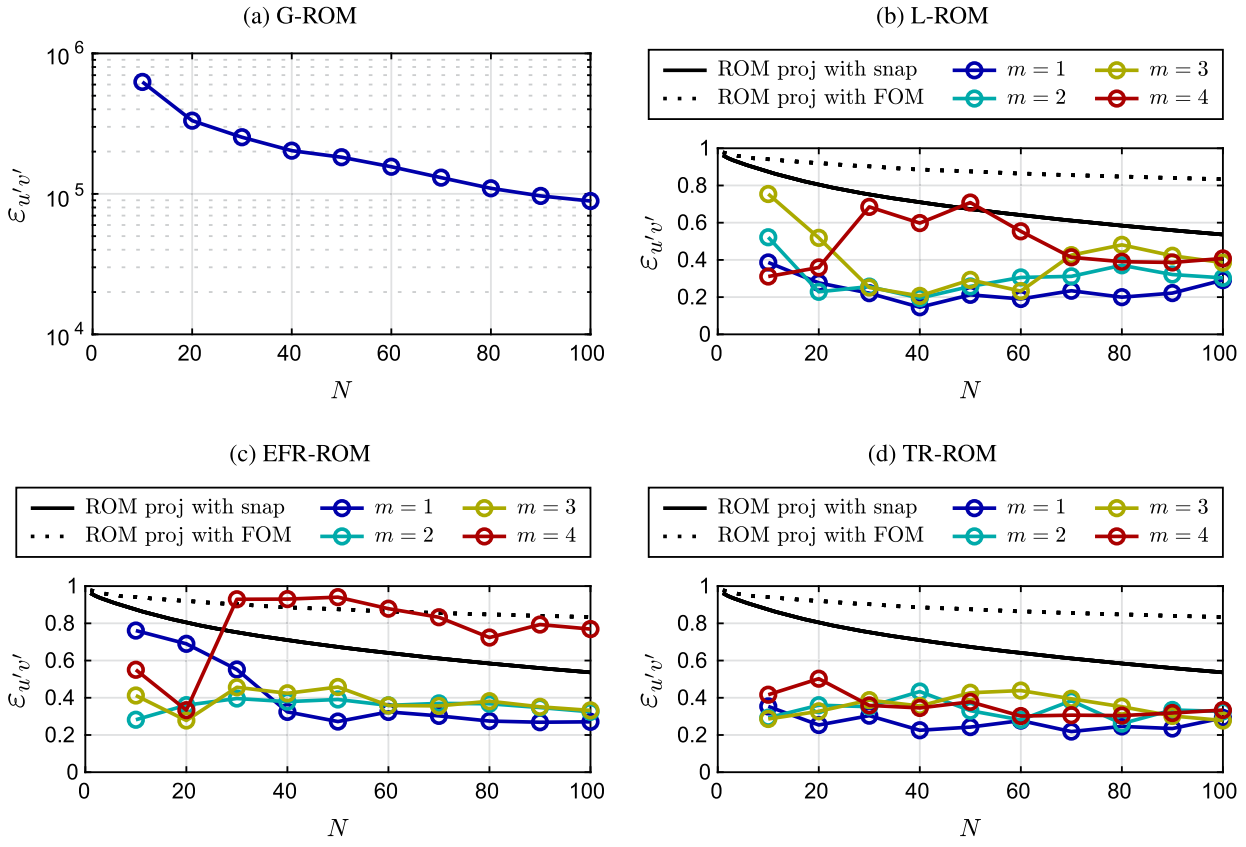

Fig. 5.3. The relative error $\varepsilon_{u'v'}$ (5.5) of G-ROM, ROM projection, L-ROM, EFR-ROM, and TR-ROM in the *reproduction regime* at $\mathrm{Re}_\tau = 180$ for different N and m values with optimal δ and χ values.

In summary, we find that L-ROM and TR-ROM with $m = 1$ yield the most accurate Reynolds shear stress for almost all N values. For EFR-ROM, this is only true for $N \geq 40$. In general, all three Reg-ROMs with $m \geq 2$ yield more accurate Reynolds shear stress for small N values. In addition, we find that the error of L-ROM and EFR-ROM with $m \geq 2$ could increase as N increases, especially with $m = 4$.

5.4.2. $\mathrm{Re}_\tau = 395$

In Fig. 5.4, we plot the relative ℓ^2 error $\varepsilon_{u'v'}$ (5.5) for different N and m values for the G-ROM, the ROM projection, and the three Reg-ROMs at $\mathrm{Re}_\tau = 395$. As in $\mathrm{Re}_\tau = 180$ case, two errors of the ROM-projections are shown. For the error labeled as "ROM proj with snap", $\langle u'v' \rangle_{\mathrm{Proj}}$ is computed with 2,000 FOM data points. For the error labeled as "ROM proj with FOM", $\langle u'v' \rangle_{\mathrm{Proj}}$ is computed with 10,000 FOM data points. Note that the error $\varepsilon_{u'v'}$ for the snapshot data at $\mathrm{Re}_\tau = 395$ is larger (approximately 70%) than the corresponding results at $\mathrm{Re}_\tau = 180$ (approximately 52%). This difference is expected because the $\mathrm{Re}_\tau = 395$ solution is more turbulent and, as a result, requires a larger number of modes to achieve a satisfactory approximation. For each Reg-ROM, the error is plotted for the optimal δ values and, for EFR-ROM and TR-ROM, for the optimal χ values.

Fig. 5.4a displays the G-ROM results. Just as in Section 5.4.1, for all N values, the G-ROM results are very inaccurate. Even with $N = 100$, $\varepsilon_{u'v'}$ is still about $\mathcal{O}(10^5)$.

Fig. 5.4b displays the L-ROM results for each N and m with the optimal δ values, along with the results of the ROM projection for comparison purposes. For all N and m values, the error is much higher than the error for $\mathrm{Re}_\tau = 180$. For $N \geq 20$, the most accurate results are achieved with $m = 1$, with an error of 37% for $N = 40$. For $N = 10$, $m = 3$ achieves an error of 43%. Compared to the ROM projection, L-ROM is more accurate for all values of N and m.

Fig. 5.4c displays the EFR-ROM results for each N and m with the optimal χ and δ values, along with the results of the ROM projection for comparison purposes. These results are qualitatively different from the EFR-ROM results for $\mathrm{Re}_\tau = 180$. For $N \leq 60$, $m = 1$ yields the most accurate results and achieves an error of 50% for $N = 40$. For $N \geq 70$, higher-order filter yields better results. Specifically, $m = 4$ achieves an error of 53% for $N = 100$. Moreover, EFR-ROM is found to be more accurate than the ROM projection for all N with $m = 1$ and for $N \geq 60$ with $m = 3,\ 4$. With $m = 2$, EFR-ROM has a similar level of accuracy as the ROM projection.

Fig. 5.4d displays the TR-ROM results for each N and m with the optimal χ and δ values, along with the results of the ROM projection for comparison purposes. For almost all N values, $m = 1$ yields the most accurate results, achieving an error of around

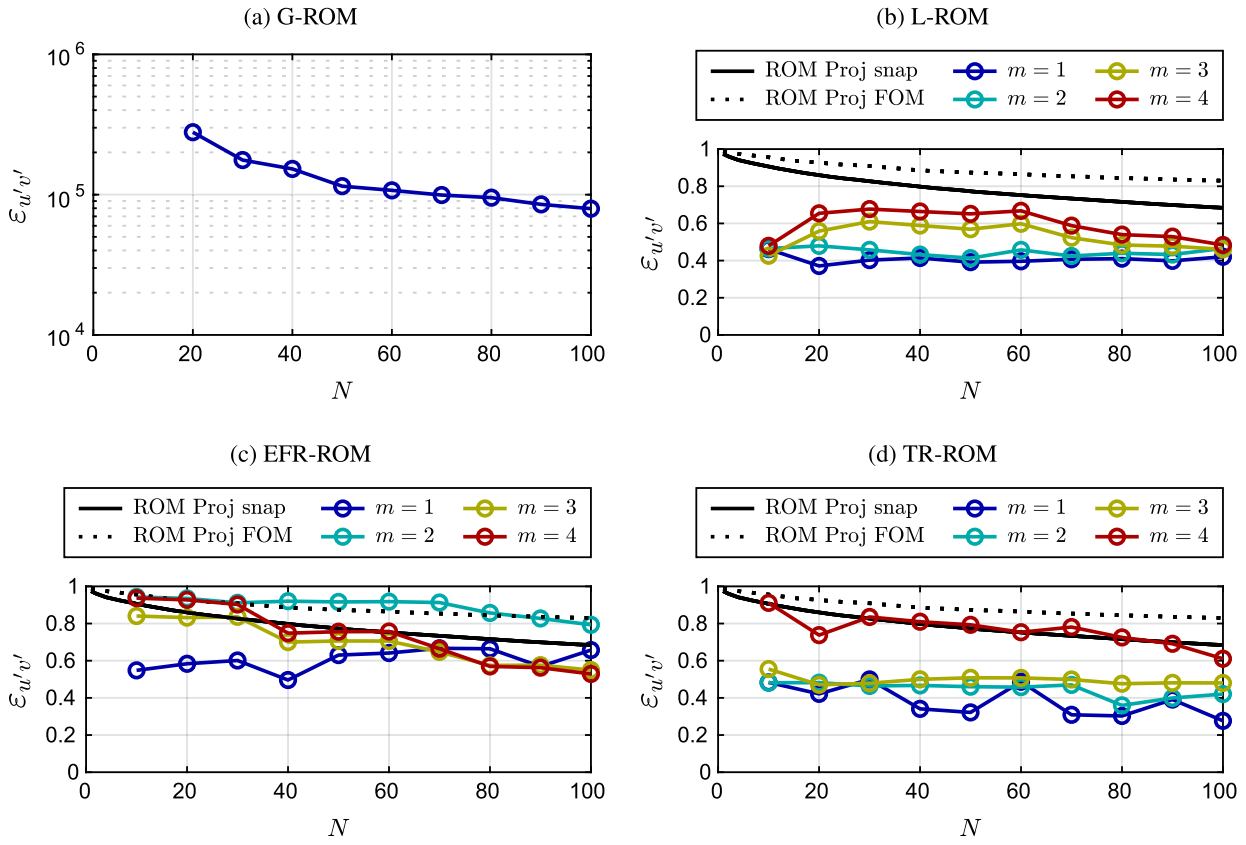

Fig. 5.4. The relative error $\varepsilon_{u'v'}$ (5.5) of G-ROM, ROM projection, L-ROM, EFR-ROM, and TR-ROM in the *reproduction regime* at $\mathrm{Re}_\tau = 395$ for different N and m values with optimal δ and χ values.

Table 1
Reg-ROM accuracy ranking in the reproduction regime for $\mathrm{Re}_\tau = 180$ (top rows) and 395 (bottom rows). The following parameters are listed: Reg-ROMs' rank, the lowest $\varepsilon_{u'v'}$, the corresponding $\varepsilon_{u'u'}$, the ROM dimension N and the filter order m for which the lowest $\varepsilon_{u'v'}$ is achieved.

$\mathrm{Re}_\tau = 180$	L-ROM	EFR-ROM	TR-ROM
Rank	3	2	1
$\varepsilon_{u'v'}$	$\approx 19\%$	$\approx 27\%$	$\approx 22\%$
$\varepsilon_{u'u'}$	$\approx 37.5\%$	$\approx 13\%$	$\approx 16\%$
N	40	90	70
m	1	1	1
$\mathrm{Re}_\tau = 395$	L-ROM	EFR-ROM	TR-ROM
Rank	2	3	1
$\varepsilon_{u'v'}$	$\approx 37\%$	$\approx 50\%$	$\approx 28\%$
$\varepsilon_{u'u'}$	$\approx 40\%$	$\approx 40\%$	$\approx 26\%$
N	20	40	100
m	1	1	1

28% for $N = 100$. These results also show that $m = 2$ and $m = 3$ yield similar results, while $m = 4$ is found to be the least accurate. Moreover, TR-ROM is found to be more accurate than the ROM projection for all N and m values.

In summary, we again find that L-ROM and TR-ROM with $m = 1$ yield the most accurate Reynolds shear stress for almost all N values, which is similar to the $\mathrm{Re}_\tau = 180$ case. For EFR-ROM, this is true for $N \leq 60$. Unlike the $\mathrm{Re}_\tau = 180$ case, Reg-ROMs with $m \geq 2$ generally yield worse results compared with $m = 1$. Moreover, compared to the $\mathrm{Re}_\tau = 180$ case, the TR-ROM error is much larger for $m = 4$ than for the other three m values.

The results of both Re_τ indicate that Reg-ROMs with $m = 1$ generally yield more accurate Reynolds shear stress than Reg-ROMs with $m \geq 2$. In addition, with $m \geq 2$, the error behavior is less consistent between the two Re_τ.

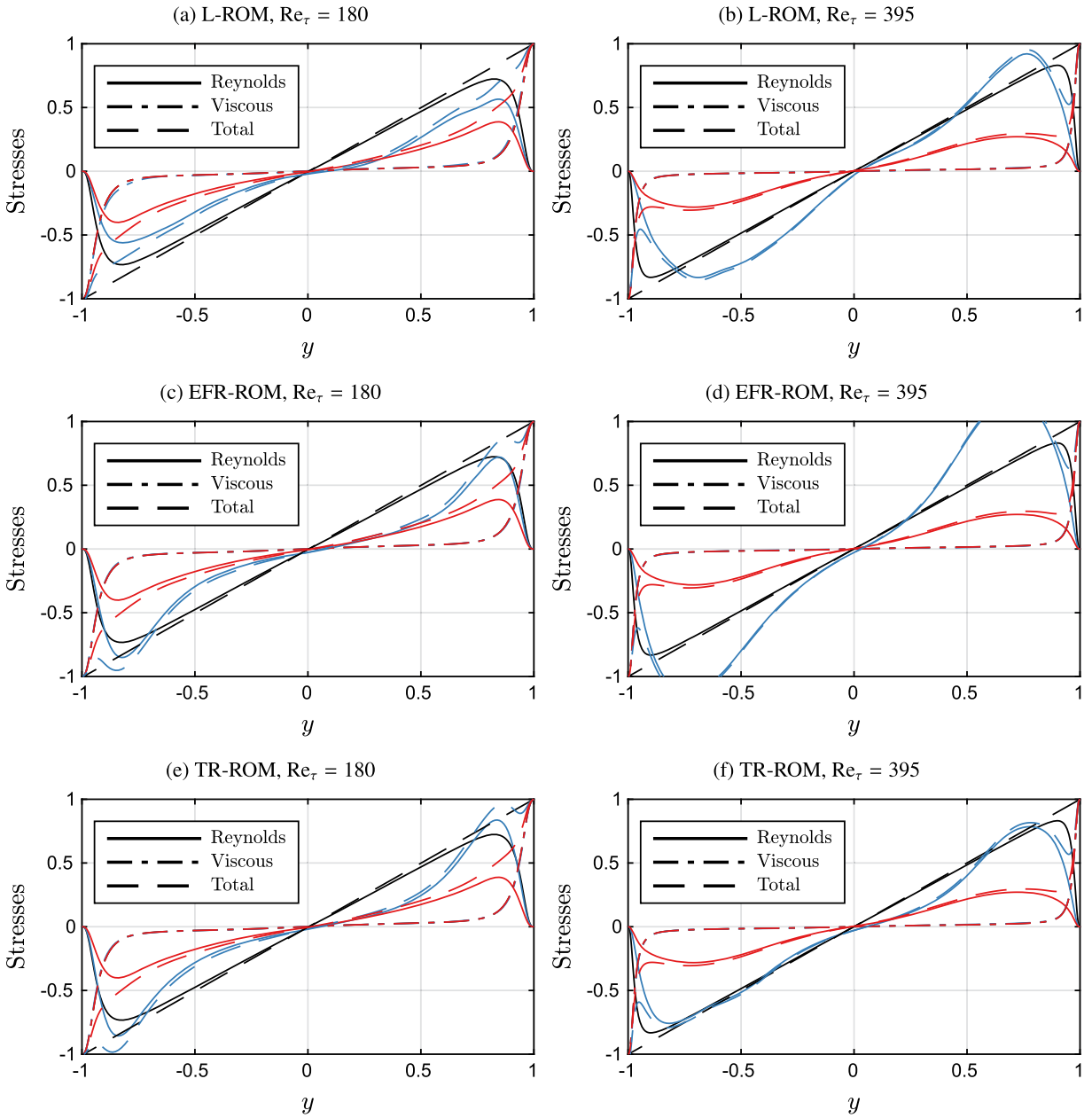

Fig. 5.5. Comparison of the total, viscous, and Reynolds shear stresses of the FOM (black), the ROM projection (red), and the optimal Reg-ROMs, listed in Table 1 (blue) in the *reproduction regime* for $\mathrm{Re}_\tau = 180$ (left) and $\mathrm{Re}_\tau = 395$ (right). The total shear stress is the sum of the viscous and the Reynolds shear stress.

We note that HOAF has been recently used in [33] with EFR-ROM, but without an extensive study with respect to the parameters studied here, that is, the ROM dimension, the filter radius, and the relaxation parameter. To our knowledge, this is the first paper to investigate HOAF extensively and compare its performance with DF. As a first step in this direction, in Appendix A, we investigate if HOAF is indeed a spatial filter and how the ROM coefficients are affected by different m values. We also note that, a discussion of the sensitivity of the optimal filter radius δ_{recon} to the filter order m can be found in the dissertation [56]. These first steps are important in the initial assessment of HOAF, but further investigation is required to gain a better understanding of the error behavior with $m \geq 2$.

5.4.3. Summary

Overall, our numerical investigation in the reproduction regime yields the following general conclusions:

All three Reg-ROMs are significantly more accurate than the standard G-ROM. In fact, with respect to several second-order turbulence statistics, the errors of the three Reg-ROMs equipped with carefully tuned spatial filtering are much lower than the projection error.

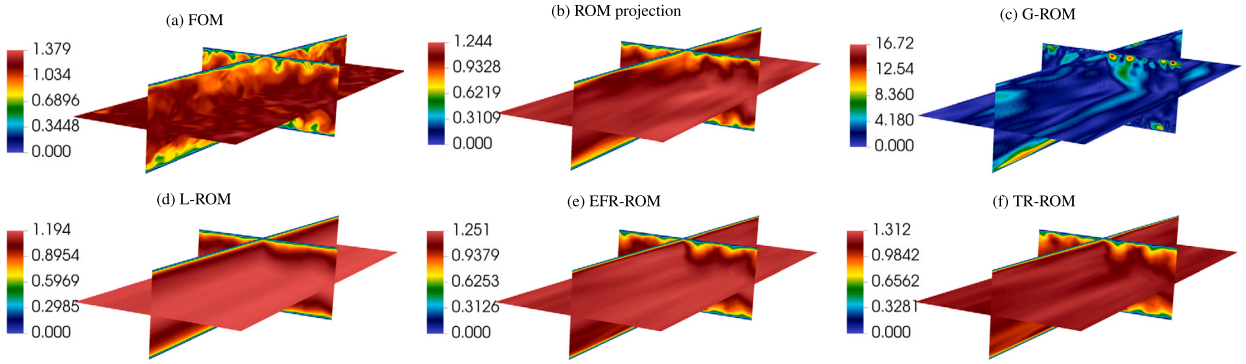

Fig. 5.6. The velocity magnitude field of the FOM, ROM projection, G-ROM, L-ROM, EFR-ROM, and TR-ROM at the same time instance in the *reproduction regime* for $\mathrm{Re}_\tau = 180$. $N = 100$ is used in both ROM projection and G-ROM. The parameters that are used for Reg-ROMs are those that yield the smallest $\varepsilon_{u'v'}$, which are listed in Table 1.

Finally, our numerical investigation demonstrates that, for $\mathrm{Re}_\tau = 180$, all three Reg-ROMs with $m = 1$ (i.e., low-order filtering) consistently produce the most accurate results for large N values, while a higher-order filter is more effective for low N values. For $\mathrm{Re}_\tau = 395$, L-ROM and TR-ROM with $m = 1$ yield the most accurate results for all N values, while EFR-ROM yields the most accurate results for low N values with $m = 1$, and for high N values with $m = 3,\ 4$.

To facilitate the comparison of the three Reg-ROMs, in Table 1, we rank them based on the error $\varepsilon_{u'v'}$ and $\varepsilon_{u'u'}$ achieved for the N and m values investigated. Specifically, for both Reynolds numbers, we list the Reg-ROMs' rank, the lowest $\varepsilon_{u'v'}$, the corresponding $\varepsilon_{u'u'}$, the ROM dimension N and the filter order m for which the lowest $\varepsilon_{u'v'}$ is achieved.

The results in Table 1 yield the following conclusions: For $\mathrm{Re}_\tau = 180$, TR-ROM is the most accurate model with $\varepsilon_{u'v'} \approx 22\%$ and $\varepsilon_{u'u'} \approx 16\%$, followed by EFR-ROM and L-ROM. For $\mathrm{Re}_\tau = 395$, TR-ROM is still the most accurate model with $\varepsilon_{u'v'} \approx 28\%$ and $\varepsilon_{u'u'} \approx 26\%$, followed by L-ROM and EFR-ROM. In addition, we find $\varepsilon_{u'u'}$ is smaller compared to $\varepsilon_{u'v'}$ except for L-ROM for $\mathrm{Re}_\tau = 180$ and $\varepsilon_{u'u'}$ has similar level of accuracy as $\varepsilon_{u'v'}$ for $\mathrm{Re}_\tau = 395$. Moreover, the results in Table 1 also show that $m = 1$ (i.e., low-order filtering) yields the most accurate results. Finally, these results show that TR-ROM requires large N values to achieve its best accuracy, whereas L-ROM yields best accuracy with small N. For EFR-ROM, large N is required for $\mathrm{Re}_\tau = 180$, and small N is required for $\mathrm{Re}_\tau = 395$.

In Fig. 5.5, we compare the total, viscous, and Reynolds shear stresses of the optimal Reg-ROMs (listed in Table 1) along with the results of the FOM and the ROM projection in the reproduction regime for $\mathrm{Re}_\tau = 180$ and $\mathrm{Re}_\tau = 395$. The total shear stress $\tau(y)$ is the sum of the viscous shear stress $\rho\nu\, d\langle u\rangle/dy$ and the Reynolds shear stress $-\rho\langle uv\rangle$, and its distribution is linear [57]. In each model, the three shear stresses are normalized with the model's wall shear stress $\tau_w \equiv \rho\nu\,(d\langle u\rangle/dy)_{y=-1}$.

In terms of the viscous shear stress, the results of the three Reg-ROMs are in good agreement with those of the FOM and the ROM projection for both Re_τ. In terms of the Reynolds shear stress, for $\mathrm{Re}_\tau = 180$, we observe that the L-ROM result is smaller than the FOM result. On the other hand, the results of the EFR-ROM and the TR-ROM are similar, and both have higher values in the boundary layer and lower values outside the boundary layer compared to the FOM. Notice that both the EFR-ROM and the TR-ROM are able to capture the slope of the Reynolds shear stress. For $\mathrm{Re}_\tau = 395$, we find that the result of the TR-ROM is the best, followed by L-ROM and EFR-ROM. Moreover, although the results of the Reg-ROMs are not perfect, we find that the results are much better than the ROM projection. This also indicates that $N = 100$ POD bases are not able to reconstruct the Reynolds stress. Finally, as a result of the discrepancy in the Reynolds shear stress, the total shear stress is not linear in all three Reg-ROMs for both Re_τ.

In addition to the turbulent statistics, we also compare the reconstructed velocity field of the ROMs and the error with respect to the snapshots. In Fig. 5.6, we compare the velocity magnitude field of the FOM, ROM projection, G-ROM, L-ROM, EFR-ROM, and TR-ROM at the same time instance in the reproduction regime for $\mathrm{Re}_\tau = 180$. The velocity field of the ROM projection is computed by projecting the FOM velocity field onto the 100-dimensional POD space. We note that the flow structures near the wall are captured better compared to the structure in the middle of the channel. This is because the flow motion near the wall is the most energetic; hence, POD tends to capture the near-wall flow structures first. For the G-ROM, the velocity field is computed with $N = 100$ modes. The result shows that the G-ROM velocity field has a much larger magnitude compared to the FOM velocity field. The velocity field of the Reg-ROMs is associated with the parameters that are listed in Table 1, which yield the lowest $\varepsilon_{u'v'}$. Compared to the ROM projection, the velocity field of TR-ROM is much more accurate than the velocity field of EFR-ROM and L-ROM. In addition, L-ROM has the smoothest field, which is consistent with the Reynolds shear stress result being under-estimated (see Fig. 5.5).

In Fig. 5.7, we compare the velocity magnitude field of the FOM, ROM projection, G-ROM, L-ROM, EFR-ROM, and TR-ROM at the same time instance in the reproduction regime for $\mathrm{Re}_\tau = 395$. The velocity field of the ROM projection is computed by projecting the FOM field onto the 100-dimensional POD space. The result again shows that the velocity field captures the flow structures near the wall better compared to the structures in the middle of the channel. For the G-ROM, the velocity field is computed with $N = 100$ modes. The results show that the G-ROM velocity has a much larger magnitude than the FOM velocity field, which is not physical. Compared to the $\mathrm{Re}_\tau = 180$ case, the magnitude is much higher. The velocity field of the Reg-ROMs is associated with the parameters that are listed in Table 1, which yield the lowest $\varepsilon_{u'v'}$. Similar to the $\mathrm{Re}_\tau = 180$ case, the TR-ROM velocity field is much more similar to the ROM projection than the L-ROM and EFR-ROM velocity fields. In addition, L-ROM has the smoothest field and the EFR-ROM

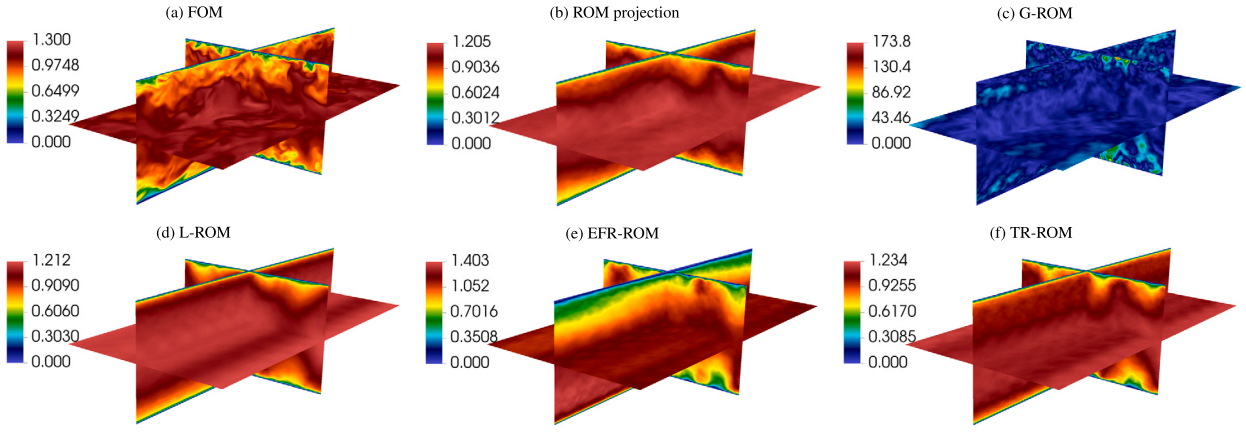

Fig. 5.7. The velocity magnitude field of the FOM, ROM projection, G-ROM, L-ROM, EFR-ROM, and TR-ROM at the same time instance in the *reproduction regime* for $\mathrm{Re}_\tau = 395$. $N = 100$ is used in both ROM projection and G-ROM. The parameters that are used for Reg-ROMs are those that yield the smallest $\varepsilon_{u'v'}$, which are listed in Table 1.

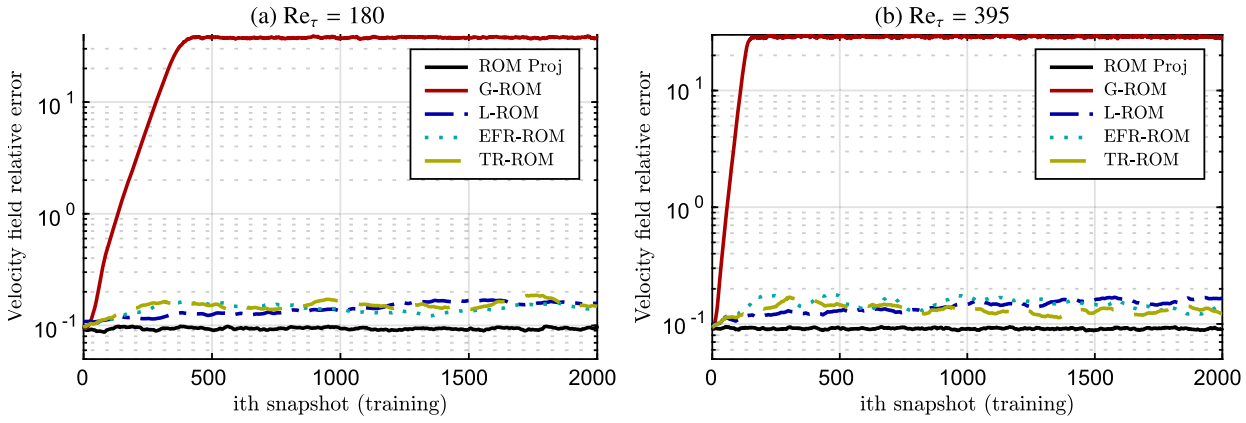

Fig. 5.8. Relative L^2 error of the velocity fields of ROM projection, G-ROM, L-ROM, EFR-ROM, and TR-ROM for (a) $\mathrm{Re}_\tau = 180$ and (b) $\mathrm{Re}_\tau = 395$. $N = 100$ is used in both ROM projection and G-ROM. The parameters that are used for Reg-ROMs are those that yield the smallest $\varepsilon_{u'v'}$, which are listed in Table 1.

velocity field has a much larger magnitude than the FOM velocity field, which is consistent with the EFR-ROM Reynolds shear stress results being over-estimated (see Fig. 5.5).

In Fig. 5.8, we compute the relative L^2 error of the velocity fields of ROM projection, G-ROM, L-ROM, EFR-ROM, and TR-ROM for $\mathrm{Re}_\tau = 180$ and $\mathrm{Re}_\tau = 395$. The results show that the error of the ROM projection remains the lowest, and is around 10% for both Re_τ values. The error of the G-ROM increases quickly and eventually reaches around 3000% for $\mathrm{Re}_\tau = 180$ and 2700% for $\mathrm{Re}_\tau = 395$. The error of the Reg-ROMs is higher than the ROM projection but remains relatively stable. In particular, for $\mathrm{Re}_\tau = 180$, the EFR-ROM and TR-ROM errors have similar trends, whereas L-ROM error increases monotonically. For $\mathrm{Re}_\tau = 395$, the TR-ROM error is the lowest, followed by EFR-ROM and L-ROM errors.

Lastly, we compare the turbulence spectra of the FOM, G-ROM, L-ROM, EFR-ROM, and TR-ROM in the reproduction regime for $\mathrm{Re}_\tau = 180$ at six physical locations near the wall, that is, $(x, y, z) = (1.0, 0.995, 1.0)$, $(2.0, 0.995, 1.0)$, $(1.0, 0.99, 1.0)$, $(2.0, 0.99, 1.0)$, $(1.0, 0.98, 1.0)$, and $(2.0, 0.98, 1.0)$. The results are presented in Fig. 5.9. At each location, 2,000 velocity time samples are collected for the FOM and ROMs. The Fourier transform of the fluctuating velocity of the 2000 samples is computed, and the turbulence spectrum is computed by using the power spectral density of each velocity component in the Fourier space. The results show that the turbulence spectrum of the G-ROM overestimates the turbulence spectrum of the DNS. The turbulence spectrum of the L-ROM, on the other hand, underestimates the turbulence spectrum of the DNS. The turbulence spectra of the EFR-ROM and TR-ROM are similar and more accurate than the L-ROM. In addition, in both cases, the high-frequency components have larger oscillations compared to the DNS. Moreover, for frequencies larger than 1, both EFR-ROM and TR-ROM spectra overestimate the FOM spectrum. We note that the turbulence spectrum of the DNS follows the $-5/3$ slope, and because of the limited number of time samples (2,000 samples in a 500 CTUs time window), the rapidly decaying region of the spectrum is truncated.

In Fig. 5.10, we compare the turbulence spectra of the FOM, G-ROM, L-ROM, EFR-ROM, and TR-ROM in the reproduction regime for $\mathrm{Re}_\tau = 395$ at six physical locations near the wall, that is, $(x, y, z) = (4.0, 0.995, 1.0)$, $(5.0, 0.995, 1.0)$, $(4.0, 0.995, 2.0)$, $(5.0, 0.995, 2.0)$, $(4.0, 0.995, 3.0)$, and $(5.0, 0.995, 3.0)$. At each location, 2,000 velocity time samples are collected for the FOM and ROMs. The results show that the turbulence spectrum of the G-ROM overestimates the turbulence spectrum of the DNS. The turbulence spectrum of the

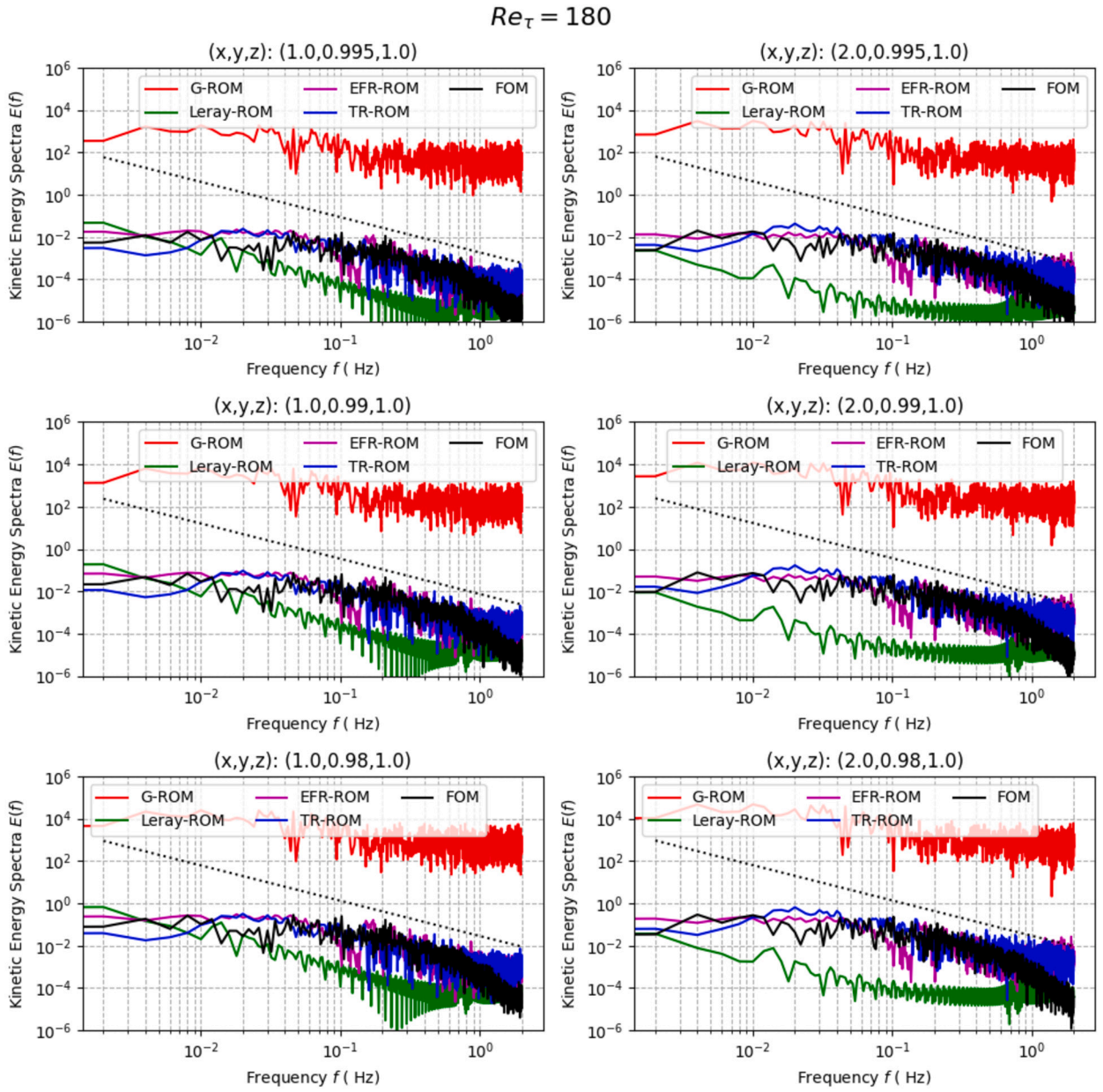

Fig. 5.9. Turbulence spectrum of the FOM, G-ROM, L-ROM, EFR-ROM, and TR-ROM in the *reproduction regime* for $\mathrm{Re}_\tau = 180$. $N = 100$ is used for G-ROM. The parameters that are used for Reg-ROMs are those that yield the smallest $\varepsilon_{u'v'}$, which are listed in Table 1.

L-ROM, on the other hand, underestimates the turbulence spectrum of the DNS and the turbulence spectrum of the EFR-ROM is more accurate that the spectrum of the L-ROM. The TR-ROM is a clear improvement over the L-ROM and EFR-ROM. As in the $\mathrm{Re}_\tau = 180$ case, the high-frequency components of EFR-ROM and TR-ROM have larger oscillations compared to the DNS. Note that, because of limited number of time samples (2,000 samples in a 1000 CTUs time window), the frequency-axis is truncated and thus the $-5/3$ slope and region of rapid decay are not present.

5.5. Predictive regime

In this section, we perform a numerical investigation of the three Reg-ROMs: L-ROM (Section 4.1), EFR-ROM (Section 4.2), and the new TR-ROM (Section 4.3) for the *predictive regime*, on a time interval that is 500 CTUs larger than the time interval on which snapshots were collected, at $\mathrm{Re}_\tau = 180$ (Section 5.5.1) and $\mathrm{Re}_\tau = 395$ (Section 5.5.2). Hence, 1,000 CTU and 1500 CTU time windows are considered for $\mathrm{Re}_\tau = 180$ and 395, respectively. For comparison purposes, we include results for the G-ROM (Section 2.2) and the ROM projection. To quantify the ROM accuracy, we use $\varepsilon_{u'u'}$ and $\varepsilon_{u'v'}$, which are the relative ℓ^2 error of $\langle u'u' \rangle$ and $\langle u'v' \rangle$ defined in

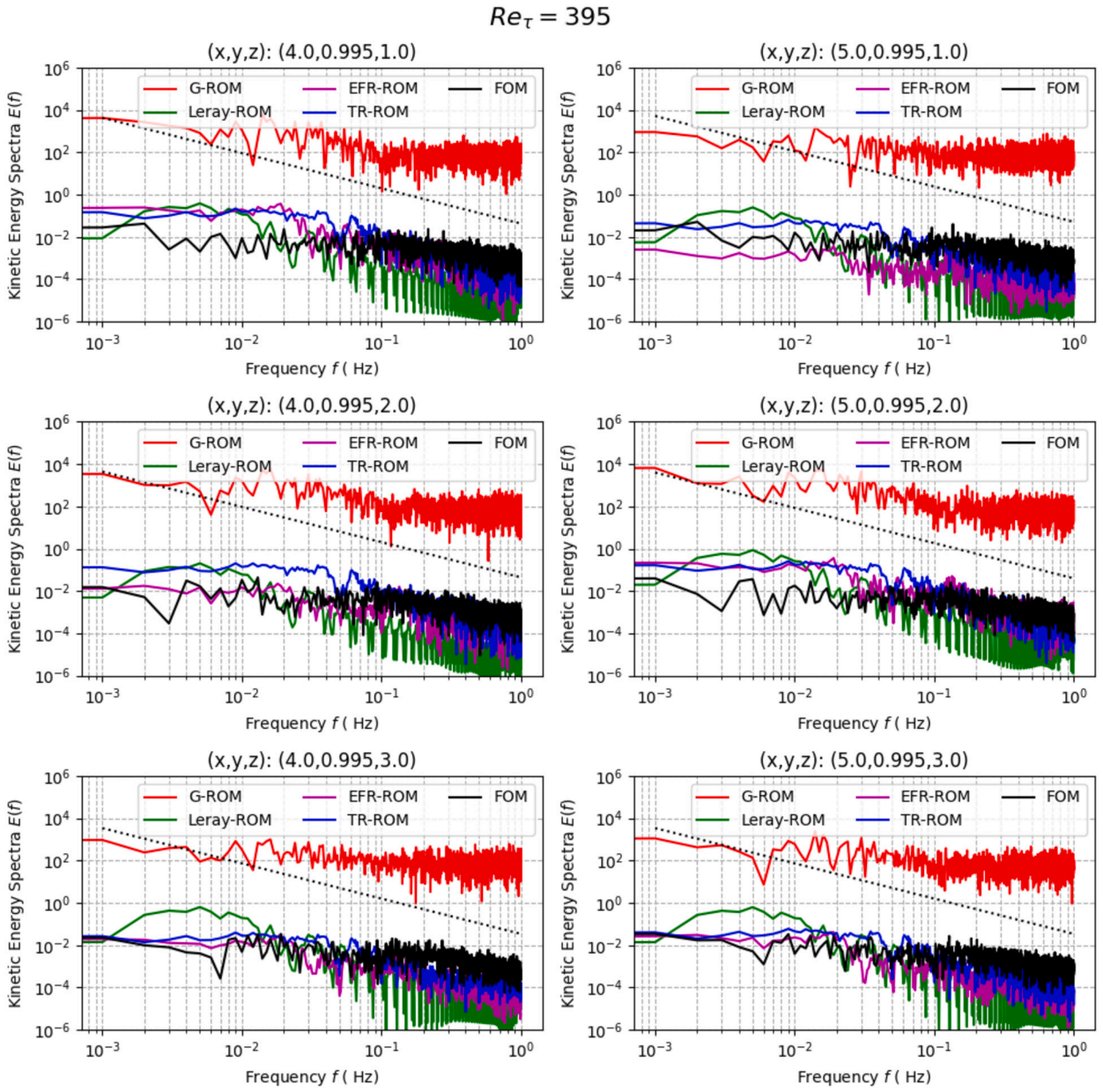

Fig. 5.10. Turbulence spectrum of the FOM, G-ROM, L-ROM, EFR-ROM, and TR-ROM in the *reproduction regime* for $\mathrm{Re}_\tau = 395$. $N = 100$ is used for G-ROM. The parameters that are used for Reg-ROMs are those that yield the smallest $\varepsilon_{u'v'}$, which are listed in Table 1.

(5.5). In order to measure the accuracy of the predicted $\langle u'u' \rangle$ and $\langle u'v' \rangle$, an additional 500 CTUs of FOM simulations are performed for both Re_τ. For the $\varepsilon_{u'u'}$ results, we refer readers to the dissertation [56].

In our numerical investigation, we use the same parameter values for N and m as the values used in Section 5.4. For each N and m values, we plot $\varepsilon_{u'v'}$ with $(\delta,\ \chi)_{\mathrm{recon}}$, that is, the δ and χ parameter values that were found to be optimal in the reproduction regime in Section 5.4. We emphasize that our strategy is different from that used in Section 5.4: Instead of optimizing the δ and χ values on the entire predictive time interval, we use the values that were optimized over the shorter time interval of the reproduction regime. Thus, in this section, we are investigating the predictive power of both the Reg-ROMs *and* their associated parameters.

Finally, in Section 5.5.3, we present a summary of the Reg-ROM comparison in the predictive regime.

5.5.1. $\mathrm{Re}_\tau = 180$

In Fig. 5.11, we plot the relative ℓ^2 error $\varepsilon_{u'v'}$ (5.5) for different N and m values for the G-ROM, the ROM projection, and the three Reg-ROMs at $\mathrm{Re}_\tau = 180$. As in the reproduction regime, two errors are shown for the ROM projection. For the one labeled as "ROM proj with snap", $\langle u'v' \rangle_{\mathrm{Proj}}$ is computed with 4,000 FOM data points (2,000 snapshot data points and 2,000 FOM data points

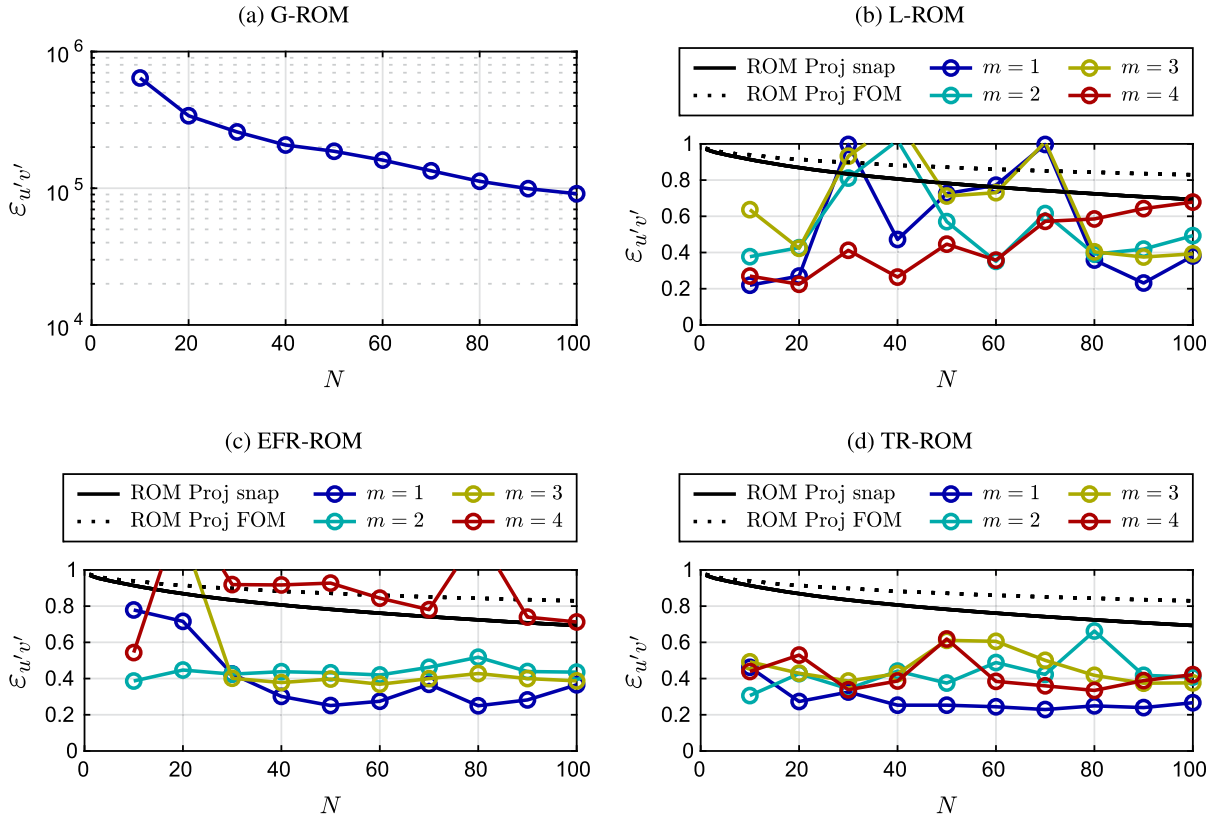

Fig. 5.11. The relative error $\varepsilon_{u'v'}$ (5.5) of G-ROM, ROM projection, L-ROM, EFR-ROM, and TR-ROM in the *predictive regime* at $\mathrm{Re}_\tau = 180$ for different N and m values with optimal δ and χ values *optimized in the reproduction regime*.

from additional 500 CTUs). For the error labeled as "ROM proj with FOM", $\langle u'v' \rangle_{\mathrm{Proj}}$ is computed with 20,000 FOM data points. We emphasize that, to test the predictive capabilities of the Reg-ROM parameters, we plot the error for $(\delta,\ \chi)_{\mathrm{recon}}$ that were optimized in the *reproduction regime* (Section 5.4.1).

Fig. 5.11a displays the G-ROM results. As in the reproduction regime, for all N values, the G-ROM results are very inaccurate.

Fig. 5.11b displays the L-ROM results for each N and m with δ_{recon} along with the ROM projection results for comparison purposes. For $N = 10$ and $N \geq 80$, $m = 1$ yields the most accurate results, achieving an error of 22% for $N = 10$. For $20 \leq N \leq 70$, $m = 4$ yields the most accurate results, achieving an error of 22% for $N = 20$. For the majority of N and m values, except for the (m, N) values $(1, 30)$, $(1, 70)$, $(2, 40)$, $(3, 30)$, $(3, 40)$, and $(3, 70)$, L-ROM is more accurate than the ROM projection.

Fig. 5.11c displays the EFR-ROM results for each N and m with $(\delta,\ \chi)_{\mathrm{recon}}$ along with the ROM projection results for comparison purposes. For $N \leq 30$, higher-order filter yields better results. Specifically, for $N = 10$ and $N = 20$, EFR-ROM achieves an error of 39% and 45%, respectively, with $m = 2$. Additionally, for $N = 30$, EFR-ROM achieves an error of 40% with $m = 3$. For $N \geq 40$, $m = 1$ yields the most accurate results, achieving an error of 25% for $N = 80$. Compared to the ROM projection, EFR-ROM is more accurate for $m \leq 3$, except for $N = 10$ and $N = 20$ with $m = 3$. For $m = 4$, EFR-ROM is not accurate and its level of accuracy is similar to that of the ROM projection.

Fig. 5.11d displays the TR-ROM results for each N and m with $(\delta,\ \chi)_{\mathrm{recon}}$ along with the ROM projection results for comparison purposes. For $N = 10$, $m = 2$ yields the lowest error of 30%. For $N \geq 20$, $m = 1$ yields the best results, achieving an error of 23% for $N = 70$. TR-ROM is more accurate than the ROM projection for all N and m values.

Compared with the results observed in the reproduction regime (discussed in Section 5.4.1), $\varepsilon_{u'v'}$ exhibits a higher sensitivity to changes in N across all m values. In particular, a much higher sensitivity is observed in both L-ROM and EFR-ROM. The non-monotonic behavior in errors in the predictive regime is a consequence of the error being calculated with the optimal parameters found in the *reproduction regime*. Specifically, the optimal parameters are selected to be those that minimize the Reynolds shear stress in the *reproduction regime*, and are further used to predict the Reynolds shear stress in a longer time interval (i.e., in the predictive regime). From the error behavior in the predictive regimes, TR-ROM is the least sensitive to the optimal parameters, followed by L-ROM and EFR-ROM. This is supported by the sensitivity study of the optimal parameters which is presented in Section 5.6.1 for $m = 1$, and the dissertation [56] for $m \geq 2$.

5.5.2. $\mathrm{Re}_\tau = 395$

In Fig. 5.12, we plot the relative ℓ^2 error $\varepsilon_{u'v'}$ for different N and m values for the G-ROM, the ROM projection, and the three Reg-ROMs at $\mathrm{Re}_\tau = 395$. As in the reproduction regime, two errors are shown for the ROM projection. For the error labeled as "ROM proj

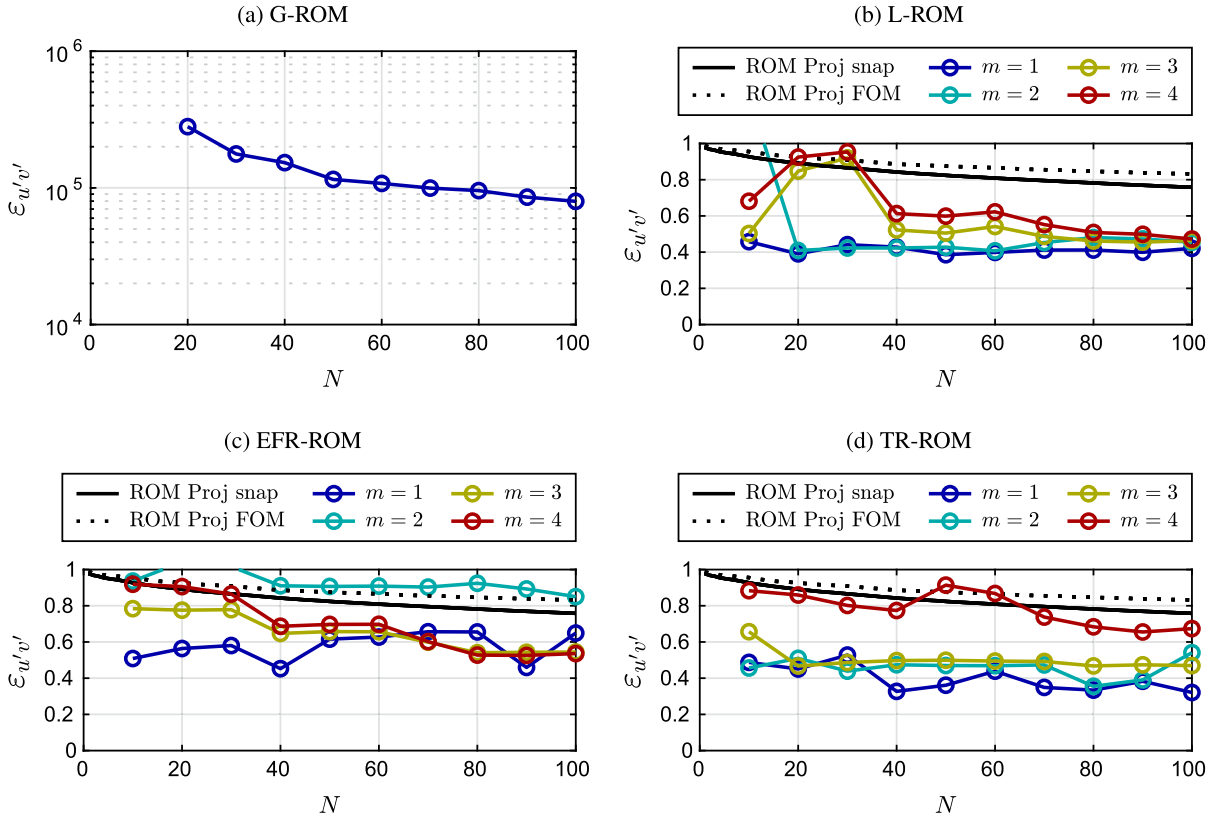

Fig. 5.12. The relative error $\varepsilon_{u'v'}$ (5.5) of G-ROM, ROM projection, L-ROM, EFR-ROM, and TR-ROM in the *predictive regime* at $\mathrm{Re}_\tau = 395$ for different N and m values with optimal δ and χ values *optimized in the reproduction regime*.

with snap", $\langle u'v' \rangle_{\mathrm{Proj}}$ is computed with 3,000 FOM data points (2,000 snapshot data points and 1,000 FOM data points from additional 500 CTUs). For the error labeled as "ROM proj with FOM", $\langle u'v' \rangle_{\mathrm{Proj}}$ is computed with 15,000 FOM data points. We emphasize that, to test the predictive capabilities of the Reg-ROM parameters, we plot the error for $(\delta,\ \chi)_{\mathrm{recon}}$ that were optimized in the *reproduction regime* (Section 5.4.2).

Fig. 5.12a displays the G-ROM results. Just as in Section 5.5.1, for all N values, the G-ROM results are very inaccurate with an error of $\mathcal{O}(10^5)$ for $N = 100$.

Fig. 5.12b displays the L-ROM results for each N and m with δ_{recon}, along with the ROM projection results for comparison purposes. For almost all N values, except for $N = 30$ and $N = 40$, $m = 1$ yields the most accurate results, achieving an error of 39% with $N = 20$. For $m = 3$ and $m = 4$, the accuracy of the L-ROM is improved as N increases but is still larger than the $m = 1$ case. Compared to the ROM projection, L-ROM is more accurate except for the (m, N) pairs $(2, 10), (3, 30)$, $(4, 20)$, and $(4, 30)$.

Fig. 5.12c displays the EFR-ROM results for each N and m with $(\delta,\ \chi)_{\mathrm{recon}}$ along with the ROM projection results for comparison purposes. For $N \leq 60$, $m = 1$ yields the most accurate results, achieving an error of 45% with $N = 40$. For $N \geq 70$, except for $N = 90$, a higher-order filter yields better results. Specifically, $m = 4$ achieves an error of 53% with $N = 80$. For $N = 90$, $m = 1$ achieves an error of 46%. Compared to the ROM projection, EFR-ROM is more accurate for all N values and $m = 1,\ 3,\ 4$. For $m = 2$, the EFR-ROM's level of accuracy is similar to that of the ROM projection.

Fig. 5.12d displays the TR-ROM results for each N and m with $(\delta,\ \chi)_{\mathrm{recon}}$, along with the ROM projection results for comparison purposes. For all N values except $N = 10$ and $N = 30$, $m = 1$ yields the most accurate results, achieving an error of around 32% for $N = 100$. These results also show that $m = 2$ and $m = 3$ yield similar accuracy, and $m = 4$ is the least accurate. TR-ROM is more accurate than the ROM projection for all N and m values, except for the (m, N) pairs $(4, 50)$ and $(4, 60)$.

Compared to the results for $\mathrm{Re}_\tau = 180$ in the predictive regime, $\varepsilon_{u'v'}$ exhibits a smaller sensitivity to changes in N across all m values. This is because the optimal parameters in the *reproduction regime* are also the optimal ones in the predictive regime for almost all N values. The optimal parameter sensitivity will be discussed in Section 5.6.1 for $m = 1$. For $m \geq 2$, the results are discussed in the dissertation [56].

5.5.3. Summary

Overall, our numerical investigation in the predictive regime yields the following general conclusions:

All three Reg-ROMs are significantly more accurate than the standard G-ROM. In fact, with respect to several second-order turbulence statistics, the errors of the three Reg-ROMs equipped with carefully tuned spatial filtering are much lower than the projection error.

Finally, our numerical investigation demonstrates that, for $\mathrm{Re}_\tau = 180$, EFR-ROM and TR-ROM with $m = 1$ (i.e., low-order filtering) consistently produce the most accurate results for large N values, while a higher-order filter is more effective for low N values. In addition, L-ROM is sensitive to changes in N for all m values. For $\mathrm{Re}_\tau = 395$, L-ROM and TR-ROM with $m = 1$ yield the most accurate results for all N values, while EFR-ROM yields the most accurate results for low N values for $m = 1$, and high N values for $m = 3, 4$.

To facilitate the comparison of the three Reg-ROMs, in Table 2, we rank them based on the lowest error achieved for the N and m values investigated. Specifically, for both Reynolds numbers, we list the Reg-ROMs' rank, the lowest $\varepsilon_{u'v'}$, the corresponding $\varepsilon_{u'u'}$, the ROM dimension N and the filter order m for which the lowest $\varepsilon_{u'v'}$ is achieved. The results in Table 2 yield the following conclusions:

Table 2
Reg-ROM accuracy ranking in the predictive regime for $\mathrm{Re}_\tau = 180$ (top rows) and 395 (bottom rows). The following parameters are listed: Reg-ROMs' rank, the lowest $\varepsilon_{u'v'}$ with δ_{recon}, the corresponding $\varepsilon_{u'u'}$, the ROM dimension N and the filter order m for which the lowest $\varepsilon_{u'v'}$ with δ_{recon} is achieved.

$\mathrm{Re}_\tau = 180$	L-ROM	EFR-ROM	TR-ROM
Rank	2	3	1
$\varepsilon_{u'v'}$	$\approx 22\%$	$\approx 25\%$	$\approx 23\%$
$\varepsilon_{u'u'}$	$\approx 23\%$	$\approx 26\%$	$\approx 9\%$
N	10	80	70
Filter order m	1	1	1
$\mathrm{Re}_\tau = 395$	L-ROM	EFR-ROM	TR-ROM
Rank	2	3	1
$\varepsilon_{u'v'}$	$\approx 39\%$	$\approx 45\%$	$\approx 32\%$
$\varepsilon_{u'u'}$	$\approx 39\%$	$\approx 36\%$	$\approx 30\%$
N	50	40	100
Filter order m	1	1	1

For $\mathrm{Re}_\tau = 180$, TR-ROM is the most accurate model with $\varepsilon_{u'v'} \approx 23\%$ and $\varepsilon_{u'u'} \approx 9\%$, followed by L-ROM and EFR-ROM. For $\mathrm{Re}_\tau = 395$, TR-ROM is still the most accurate model with $\varepsilon_{u'v'} \approx 32\%$ and $\varepsilon_{u'u'} \approx 30\%$, followed by EFR-ROM and L-ROM. In addition, the results in Table 2 also show that $m = 1$ (i.e., low-order filtering) yields the most accurate results. Moreover, these results show that TR-ROM requires large N values to achieve its best accuracy, whereas L-ROM yields best accuracy with small N. For EFR-ROM, large N is required for $\mathrm{Re}_\tau = 180$, and small N is required for $\mathrm{Re}_\tau = 395$.

Similarly to the reproduction regime (Fig. 5.5), in Fig. 5.13, we compare the total, viscous, and the Reynolds shear stresses of the optimal Reg-ROMs (listed in Table 2) along with the results of the FOM and the ROM projection in the predictive regime for $\mathrm{Re}_\tau = 180$ and $\mathrm{Re}_\tau = 395$.

In terms of the viscous shear stress, the results of the three Reg-ROMs are in good agreement with those of the FOM and the ROM projection for both Re_τ. In terms of the Reynolds shear stress, we find that TR-ROM yields the most accurate results for both Re_τ and the L-ROM is better than the EFR-ROM for $\mathrm{Re}_\tau = 180$. For $\mathrm{Re}_\tau = 395$, L-ROM and EFR-ROM perform similarly. In addition, from the results of the ROM projection, we find that $N = 100$ POD basis functions are insufficient to reconstruct the Reynolds shear stress accurately. Finally, as results of the discrepancy in the Reynolds shear stress, the total shear stress is not linear in all three Reg-ROMs for both Re_τ.

Next, we discuss the potential issue that preclude Reg-ROMs from getting more accurate Reynolds shear stress.

From Figs. 5.3–5.12, we found that $\varepsilon_{u'v'}$ of the ROM projection has at least 55% errors for $\mathrm{Re}_\tau = 180$, and 70% errors for $\mathrm{Re}_\tau = 395$. This indicates the poor approximation capability of the reduced basis functions for the Reynolds shear stress $\langle u'v' \rangle$. With this approximation error, it is not surprising to find that $\varepsilon_{u'v'}$ of Reg-ROMs is not below 10%. In order to improve the accuracy, one either needs to increase the number of ROM basis functions or consider a ROM basis that is designed for the Reynolds stress approximation.

5.6. Sensitivity study

In this section, we perform sensitivity studies for the three Reg-ROMs: In Section 5.6.1, we present a sensitivity study of the optimal parameter $(\delta,\ \chi)_{\mathrm{recon}}$ for each N and m in the predictive regime. In Section 5.6.2, we present a sensitivity study of the relative ℓ^2 error $\varepsilon_{u'v'}$ of EFR-ROM and TR-ROM with respect to the relaxation parameter, χ. In Section 5.6.3, we present a sensitivity study of the relative ℓ^2 error $\varepsilon_{u'v'}$ of the three Reg-ROMs with respect to the filter radius, δ. We refer to the dissertation [56] for the optimal filter radius δ_{recon}'s sensitivity with respect to the filter order m for the three Reg-ROMs.

5.6.1. Reg-ROM parameter sensitivity in the predictive regime

In Section 5.5, for given N and m, we investigated the accuracy of the three Reg-ROMs using $(\delta,\ \chi)_{\mathrm{recon}}$ in the *predictive regime*, where $(\delta,\ \chi)_{\mathrm{recon}}$ are the δ and χ values that are optimal in the reproduction regime. In this section, we extend that study and

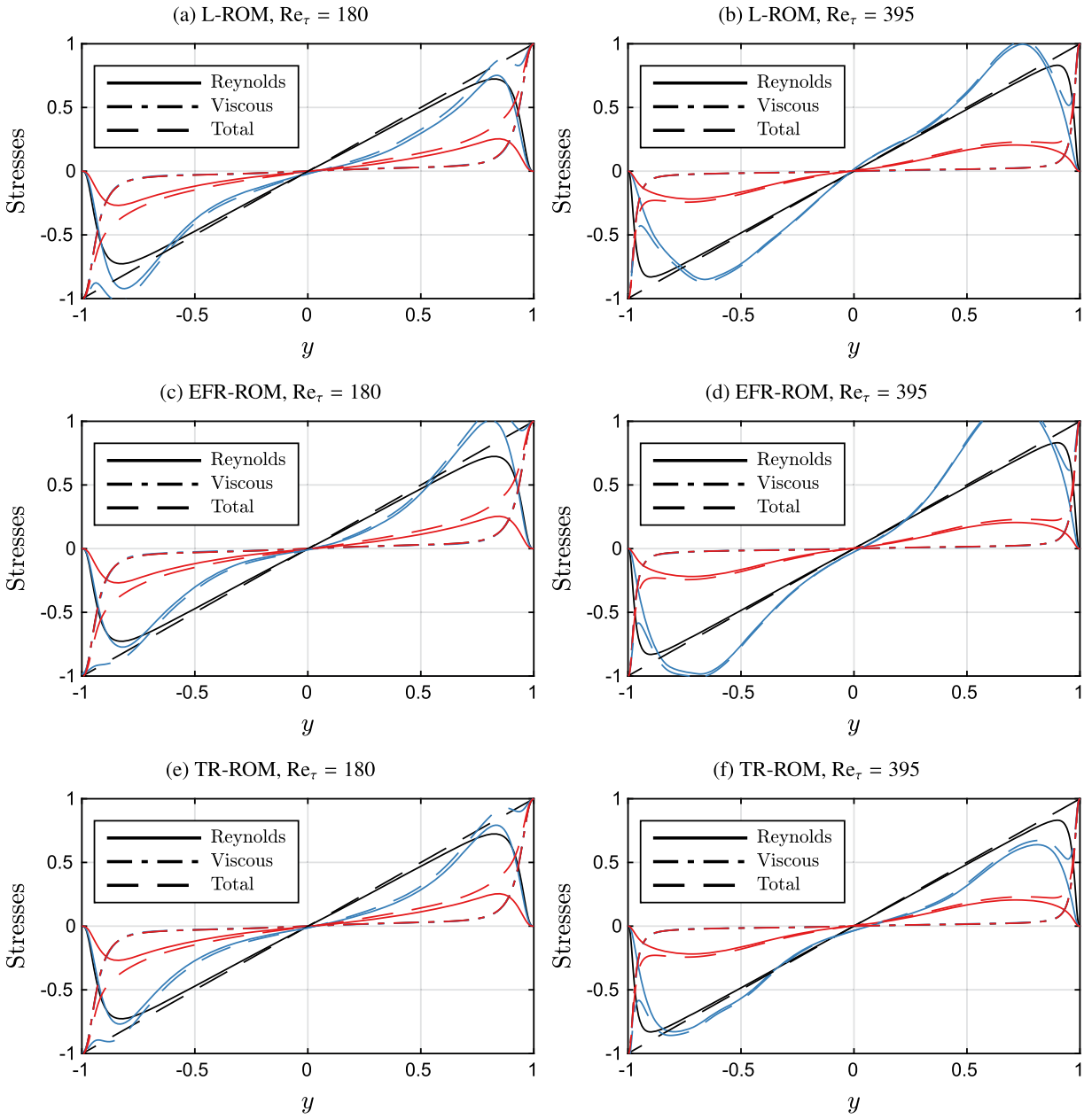

Fig. 5.13. Comparison of the total, viscous, and Reynolds shear stresses of the FOM (black), the ROM projection (red), and the optimal Reg-ROMs, listed in Table 2 (blue) in the *predictive regime* for $\mathrm{Re}_\tau = 180$ (left) and $\mathrm{Re}_\tau = 395$ (right). The total shear stress is the sum of the viscous and the Reynolds shear stress.

investigate the robustness of the optimal parameter $(\delta,\ \chi)_{\text{recon}}$ for each N value with $m = 1$ by comparing $(\delta,\ \chi)_{\text{recon}}$ to $(\delta,\ \chi)_{\text{pred}}$, that is, the δ and χ values that are optimal in the predictive regime. We present $m = 1$ results because this is the filter order that yields the best models compared to other m values. For the sensitivity results of other m values, see [56]. In order to find $(\delta,\ \chi)_{\text{pred}}$, we consider the same parameter sets for δ and χ as those used in the reproduction regime (Section 5.4). An additional 500 CTUs FOM simulations are performed for both Re_τ in order to compute $\varepsilon_{u'u'}$ and $\varepsilon_{u'v'}$.

In Fig. 5.14, we plot δ_{recon} and δ_{pred} for different N values for the three Reg-ROMs at both Re_τ. δ_{recon} is displayed as a smaller filled marker, while δ_{pred} is displayed as a larger empty marker. We also use different markers to distinguish the relaxation parameter, χ. We note that, for a given N, if $(\delta,\ \chi)_{\text{recon}}$ is also optimal for the predictive regime, the two corresponding markers of different sizes will be on top of each other.

Figs. 5.14a and 5.14b display L-ROM's $(\delta,\ \chi)_{\text{recon}}$ and $(\delta,\ \chi)_{\text{pred}}$ for each N for $\mathrm{Re}_\tau = 180$ and $\mathrm{Re}_\tau = 395$, respectively. Note that the relaxation parameter, χ, is not used in L-ROM (4.1) and, therefore, is not plotted. For $\mathrm{Re}_\tau = 180$, we find that δ_{recon} is close to

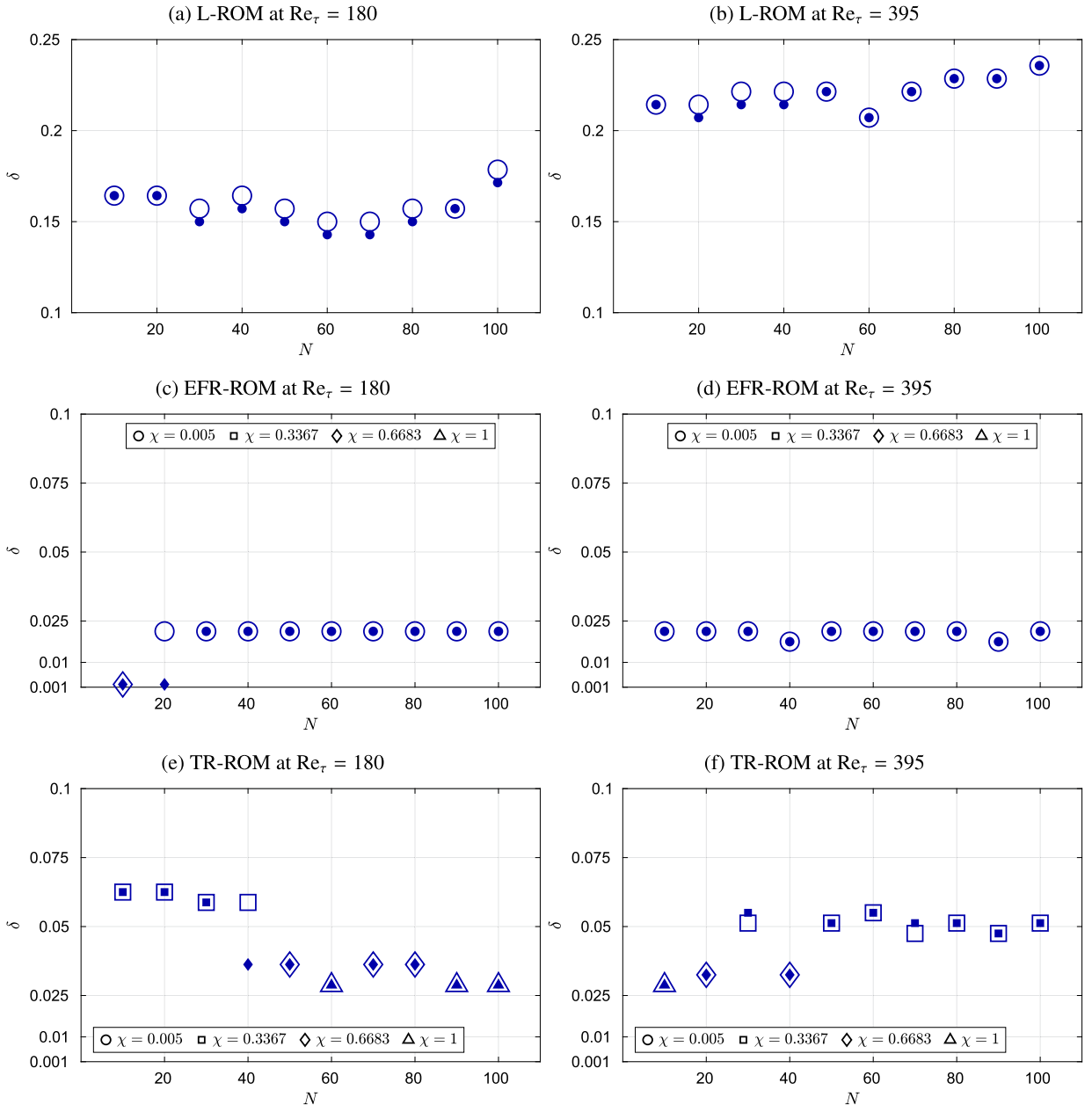

Fig. 5.14. $(\delta,\ \chi)_{\text{recon}}$ (smaller filled marker) and $(\delta,\ \chi)_{\text{pred}}$ (larger empty marker) distributions of the three Reg-ROMs for $m = 1$ and $N = 10, \ldots, 100$ at $\text{Re}_\tau = 180$ (left) and $\text{Re}_\tau = 395$ (right). $(\delta,\ \chi)_{\text{recon}}$ and $(\delta,\ \chi)_{\text{pred}}$ are the optimal filter radius and relaxation parameter values found in the reproduction and predictive regimes, respectively.

but not identical to δ_{pred} for most N values. For $\text{Re}_\tau = 395$, we find that δ_{recon} is identical to δ_{pred} for most N values, except for $N = 20,\ 30,\ 40$. In addition, for both Re_τ, we find that larger N lead to larger δ_{recon} and δ_{pred}.

Figs. 5.14c and 5.14d display EFR-ROM's $(\delta,\ \chi)_{\text{recon}}$ and $(\delta,\ \chi)_{\text{pred}}$ for each N for $\text{Re}_\tau = 180$ and $\text{Re}_\tau = 395$, respectively. For $\text{Re}_\tau = 180$, we find that $(\delta,\ \chi)_{\text{recon}}$ is optimal for almost all N values except for $N = 20$. For $\text{Re}_\tau = 395$, we find that δ_{recon} is identical to δ_{pred} for all N values.

In addition, we find that the EFR-ROM's δ is less sensitive to N compared to the L-ROM's δ. Moreover, for the same χ_{recon}, we find that δ_{recon} and δ_{pred} are not sensitive to Re_τ. Finally, we find that $\chi = 0.005$ works best for most N except for $N = 10,\ 20$ at $\text{Re}_\tau = 180$.

Figs. 5.14e and 5.14f display TR-ROM's $(\delta,\ \chi)_{\text{recon}}$ and $(\delta,\ \chi)_{\text{pred}}$ for each N for $\text{Re}_\tau = 180$ and $\text{Re}_\tau = 395$, respectively. For $\text{Re}_\tau = 180$, we find that δ_{recon} is robust for all N values except for $N = 40$. For $\text{Re}_\tau = 395$, we again find that δ_{recon} is robust for all

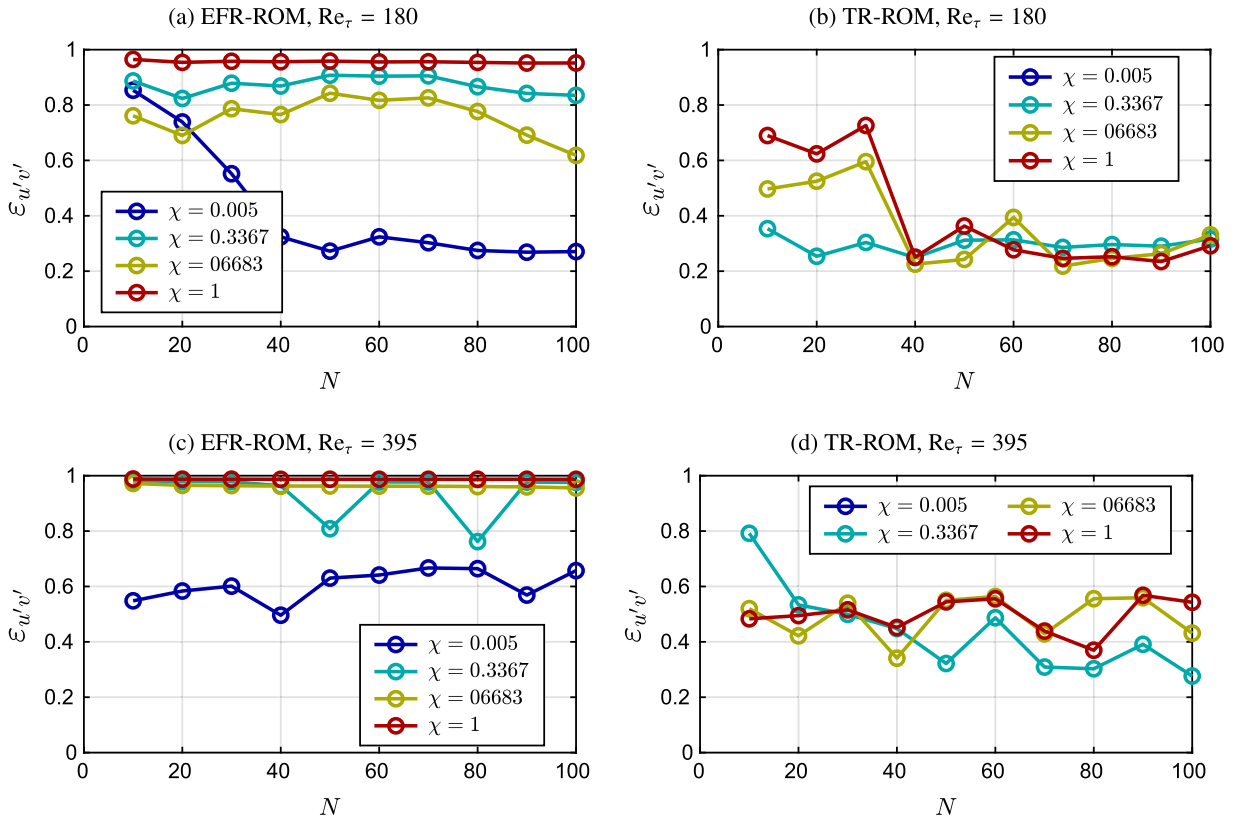

Fig. 5.15. The relative error $\varepsilon_{u'v'}$ (5.5) of EFR-ROM and TR-ROM with respect to N and χ for $\mathrm{Re}_\tau = 180$ (5.15a and 5.15b) and $\mathrm{Re}_\tau = 395$ (5.15c and 5.15d) with $m = 1$ and δ_{recon}, where δ_{recon} is the optimal δ value found in the reproduction regime.

N values except for $N = 30$ and $N = 70$. Compared to the L-ROM and EFR-ROM results, we find that $(\delta,\ \chi)_{\mathrm{recon}}$ and $(\delta,\ \chi)_{\mathrm{pred}}$ are in general more sensitive to N and Re_τ in TR-ROM.

In summary, across all three Reg-ROMs with $m = 1$, we find that δ_{recon} is optimal for most N values for both Re_τ, demonstrating the predictive capabilities of the three Reg-ROMs and their associated parameters.

5.6.2. *Reg-ROM sensitivity to the relaxation parameter χ*

In this section, we study the EFR-ROM and TR-ROM sensitivity to the relaxation parameter, χ. To this end, we consider $\varepsilon_{u'v'}$ as the metric. For each N and m, we investigate how $\varepsilon_{u'v'}$ is affected by χ, and what χ values yield the lowest $\varepsilon_{u'v'}$ values.

We consider four χ values, which are uniformly sampled in the interval $[\Delta t = 0.005,\ 1]$. For each N and χ values, we show $\varepsilon_{u'v'}$ with δ_{recon} and $m = 1$. We fix the filter order m to be 1 because this is the value that yields the best Reg-ROMs in the reproduction and predictive regimes (Sections 5.4.3 and 5.5.3).

Fig. 5.15a displays the EFR-ROM results at $\mathrm{Re}_\tau = 180$ for each N and for four χ values. We recall that, in EFR-ROM (4.4), χ represents the contribution from the filtered solution at each time step. We find that EFR-ROM with $\chi = \Delta t = 0.005$ yields the best results. For $\chi = 1$, EFR-ROM is too dissipative and leads to an error of around 100% in $\langle u'v' \rangle$ for all N values. Although the number of samples we consider for χ is limited due to the training time, it is interesting to see that $\chi = \Delta t$ yields the best EFR-ROM results, just as in the FOM case [55,18].

Fig. 5.15b displays the TR-ROM results for $\mathrm{Re}_\tau = 180$ for each N and for four χ values. We recall that, in TR-ROM (4.5), χ represents the amount of additional diffusion added to the G-ROM (2.3). This time, we find that TR-ROM with $\chi = \Delta t = 0.005$ yields the worst results. Because the amount of diffusion added to G-ROM is not able to stabilize it, the error $\varepsilon_{u'v'}$ for each N is more than 100%. For the other three χ values, for $N \leq 30$, we find that smaller χ values lead to better accuracy, and for $N \geq 40$, we find that the error $\varepsilon_{u'v'}$ is similar.

Fig. 5.15c displays the EFR-ROM results for $\mathrm{Re}_\tau = 395$ for each N and for four χ values. We again find that EFR-ROM with $\chi = \Delta t = 0.005$ yields the best results. In contrast with the results for $\mathrm{Re}_\tau = 180$, we find that EFR-ROM for the other three χ values leads to an error of around 100% in $\langle u'v' \rangle$ for all N values.

Fig. 5.15d displays the TR-ROM results of $\mathrm{Re}_\tau = 395$ for each N and for four χ values. Again, we find that TR-ROM for $\chi = \Delta t = 0.005$ yields the worst results and the error $\varepsilon_{u'v'}$ is more than 100% for each N. For $N \leq 40$, we find that $\chi = 0.6683$ yields the best results for $N = 20$ and 40, and $\chi = 1$ yields the best results for $N = 10$ and $N = 30$. For $N \geq 50$, we find that $\chi = 0.3367$ yields the best results.

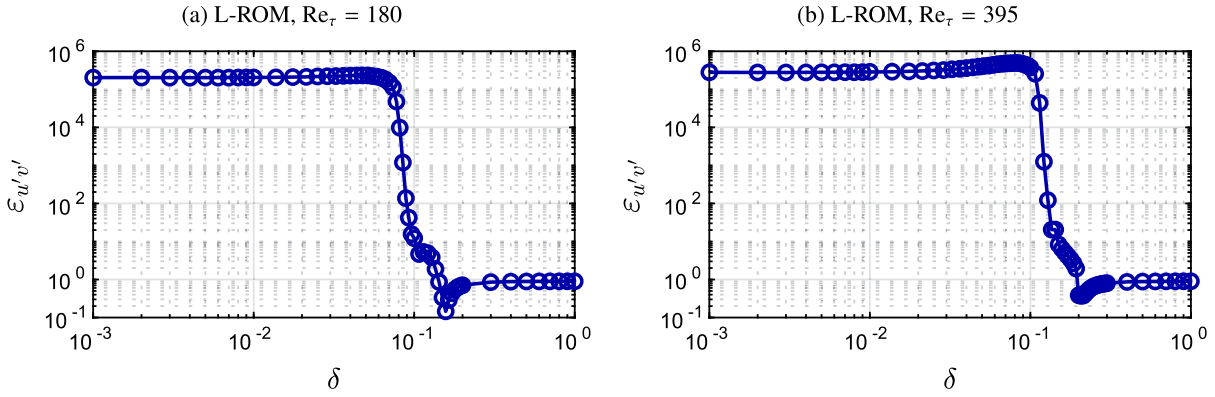

Fig. 5.16. The relative error $\varepsilon_{u'v'}$ (5.5) of L-ROM with respect to δ for $\mathrm{Re}_\tau = 180$ (5.16a) and $\mathrm{Re}_\tau = 395$ (5.16b).

In summary, we found that both EFR-ROM and TR-ROM are sensitive to the relaxation parameter χ. Furthermore, for EFR-ROM, we found that $\chi = \Delta t = 0.005$ outperforms the other three values for almost all N. For TR-ROM, we found that $\chi = 0.3367$ outperforms the other values for all N for $\mathrm{Re}_\tau = 180$, and for large N for $\mathrm{Re}_\tau = 395$.

5.6.3. *Reg-ROM sensitivity to the filter radius δ*

In this section, for the optimal parameters listed in Table 1, we study the Reg-ROM sensitivity to the filter radius δ for $\mathrm{Re}_\tau = 180$ and $\mathrm{Re}_\tau = 395$. Our goal is to analyze the impact of δ on the Reg-ROM performance and identify the δ values that yield the best results.

Figs. 5.16a and 5.16b display the L-ROM's $\varepsilon_{u'v'}$ behavior with respect to the filter radius, δ, for $\mathrm{Re}_\tau = 180$ and $\mathrm{Re}_\tau = 395$. To discuss these results, we divide the interval $[0.001,\ 1]$ into four subintervals: (i) For $\delta \in [0.001,\ 0.01]$, $\varepsilon_{u'v'}$ is high and does not change with respect to δ. (ii) For $\delta \in [0.01,\ 0.1]$, $\varepsilon_{u'v'}$ increases as δ increases, and starts decreasing when δ approaches 0.01. In addition, a much larger error drop is observed for $\mathrm{Re}_\tau = 180$ than for $\mathrm{Re}_\tau = 395$. (iii) For $\delta \in [0.1,\ 0.2]$, $\varepsilon_{u'v'}$ decreases dramatically from $\mathcal{O}(10^5)$ down to 0.1 and 0.37 for $\mathrm{Re}_\tau = 180$ and $\mathrm{Re}_\tau = 395$, respectively. For both Re_τ, the optimal filter radius, δ_{recon}, is obtained in the interval $[0.1,\ 0.2]$. (iv) For $\delta \in [0.2,\ 1]$, $\varepsilon_{u'v'}$ increases as δ increases, and eventually plateaus at $\mathcal{O}(1)$ because L-ROM becomes too dissipative.

Figs. 5.17a and 5.17b display the EFR-ROM's $\varepsilon_{u'v'}$ behavior with respect to the filter radius, δ, for four χ values and for $\mathrm{Re}_\tau = 180$ and $\mathrm{Re}_\tau = 395$. From the results, we can categorize EFR-ROM's $\varepsilon_{u'v'}$ behavior into two types:

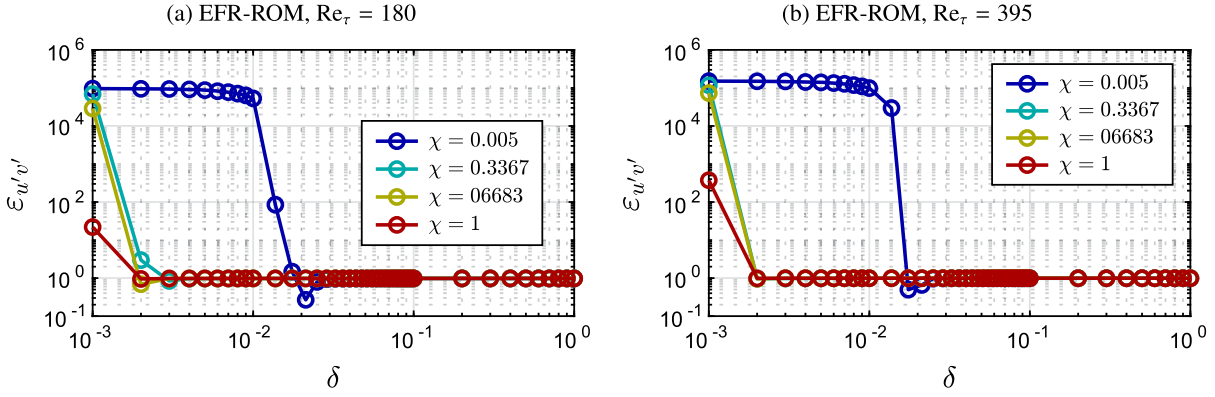

Fig. 5.17. The relative error $\varepsilon_{u'v'}$ (5.5) of EFR-ROM with respect to δ for $\mathrm{Re}_\tau = 180$ (5.17a) and $\mathrm{Re}_\tau = 395$ (5.17b).

For $\chi = \Delta t = 0.005$, the behavior of $\varepsilon_{u'v'}$ with respect to δ is similar to that for L-ROM. We can divide the interval $[0.001,\ 1]$ into three subintervals: (i) For $\delta \in [0.001,\ 0.01]$, $\varepsilon_{u'v'}$ decreases slightly as δ increases. (ii) For $\delta \in [0.01,\ 0.03]$, $\varepsilon_{u'v'}$ decreases dramatically from $\mathcal{O}(10^5)$ down to 0.27 and 0.5 for $\mathrm{Re}_\tau = 180$ and $\mathrm{Re}_\tau = 395$, respectively. For both Re_τ values, the optimal filter radius, δ_{recon}, is obtained in the interval $[0.01,\ 0.03]$. (iii) For $\delta \in [0.03,\ 1]$, $\varepsilon_{u'v'}$ increases as δ increases, and eventually plateaus at $\mathcal{O}(1)$ because EFR-ROM becomes too dissipative.

For the other three χ values, we can divide the interval $[0.001,\ 1]$ into two subintervals: (i) For $\delta \in [0.001,\ 0.003]$, $\varepsilon_{u'v'}$ decreases dramatically to $\mathcal{O}(1)$. However, the fact that there is no δ such that $\varepsilon_{u'v'}$ is below 1 suggests that the optimal filter radius δ_{recon} is either very sensitive, which requires more sampling points in the interval $[0.001,\ 0.003]$, or it does not exist at all. (ii) For $\delta \in [0.003,\ 1]$, $\varepsilon_{u'v'}$ is mostly $\mathcal{O}(1)$, suggesting that, for these χ values, EFR-ROM is too dissipative regardless of the δ value.

Figs. 5.18a and 5.18b display the TR-ROM's $\varepsilon_{u'v'}$ behavior with respect to the filter radius, δ, for four χ values and for $\mathrm{Re}_\tau = 180$ and $\mathrm{Re}_\tau = 395$. From the results, we can categorize TR-ROM's $\varepsilon_{u'v'}$ behavior into two:

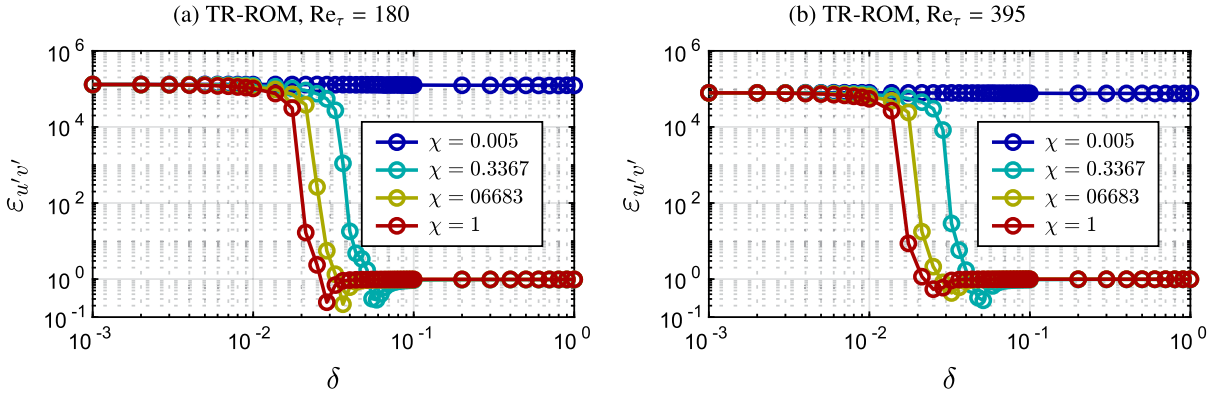

Fig. 5.18. The relative error $\varepsilon_{u'v'}$ (5.5) of TR-ROM with respect to δ for $\mathrm{Re}_\tau = 180$ (5.21a) and $\mathrm{Re}_\tau = 395$ (5.21b).

For $\chi = \Delta t = 0.005$, there is no improvement in $\varepsilon_{u'v'}$ as δ increases. This suggests that χ is so small that, regardless of how large the dissipative term $(\boldsymbol{u}_r - \overline{\boldsymbol{u}}_r)$ (4.6) (determined by δ) is, the total contribution $\chi(\boldsymbol{u}_r - \overline{\boldsymbol{u}}_r)$ is too small to stabilize G-ROM (2.3).

For the other three χ values, the TR-ROM's behavior of $\varepsilon_{u'v'}$ with respect to δ is similar to that of L-ROM and EFR-ROM for $\chi = 0.005$. We can divide the interval $[0.001,\ 1]$ into three subintervals: (i) For $\delta \in [0.001,\ 0.01]$, $\varepsilon_{u'v'}$ decreases slightly as δ increases. (ii) For $\delta \in [0.01,\ 0.1]$, $\varepsilon_{u'v'}$ decreases dramatically from $\mathcal{O}(10^5)$ down to its optimal value. Furthermore, the smaller the χ value, the larger the δ value required to achieve its optimal $\varepsilon_{u'v'}$. This is expected because assuming that the total contribution $\chi(\boldsymbol{u}_r - \overline{\boldsymbol{u}}_r)$ for optimal TR-ROM is fixed, larger χ will then require smaller δ. (iii) For $\delta \in [0.1,\ 1]$, $\varepsilon_{u'v'}$ increases as δ increases, and eventually plateaus at $\mathcal{O}(1)$ because TR-ROM becomes too dissipative.

In summary, we find that all three Reg-ROMs are sensitive to the filter radius, δ. For EFR-ROM and TR-ROM, δ_{recon} is affected by the relaxation parameter χ, and in the worst-case scenario, δ_{recon} might not even exist. In addition, we find that the optimal range for δ and the effect of χ are similar for the two Re_τ values.

5.7. Comparison between Reg-ROMs and mixing-length ROM

In this section, we compare the Reg-ROMs with an eddy viscosity approach, the mixing-length ROM (ML-ROM), which is proposed in [58] and defined as follows: *Find* $\boldsymbol{u}_r$ *of the form* (2.2) *such that,* $\forall\, i = 1, \ldots N$,

$$\left(\frac{\partial \boldsymbol{u}_\mathrm{r}}{\partial t}, \boldsymbol{\varphi}_i\right) + Re^{-1}\ \left(\nabla \boldsymbol{u}_\mathrm{r}, \nabla \boldsymbol{\varphi}_i\right) + \left((\boldsymbol{u}_\mathrm{r} \cdot \nabla)\boldsymbol{u}_\mathrm{r}, \boldsymbol{\varphi}_i\right) + \nu_e \left((\nabla \boldsymbol{u}_\mathrm{r} + \nabla \boldsymbol{u}_\mathrm{r}{}^T), \nabla \boldsymbol{\varphi}_i\right) = 0, \tag{5.14}$$

where $\nu_e = \alpha U_{\mathrm{ML}} \delta$ is the eddy viscosity parameter, U_{ML} and δ are characteristic velocity and length scales for the unresolved scales, and α is a dimensionless parameter. ML-ROM was first used to study the wall region of the turbulent boundary layer, and was later investigated in the minimal flow unit [59] and channel flow [60]. A further investigation of the ML-ROM with other eddy viscosity approaches was presented in [61].

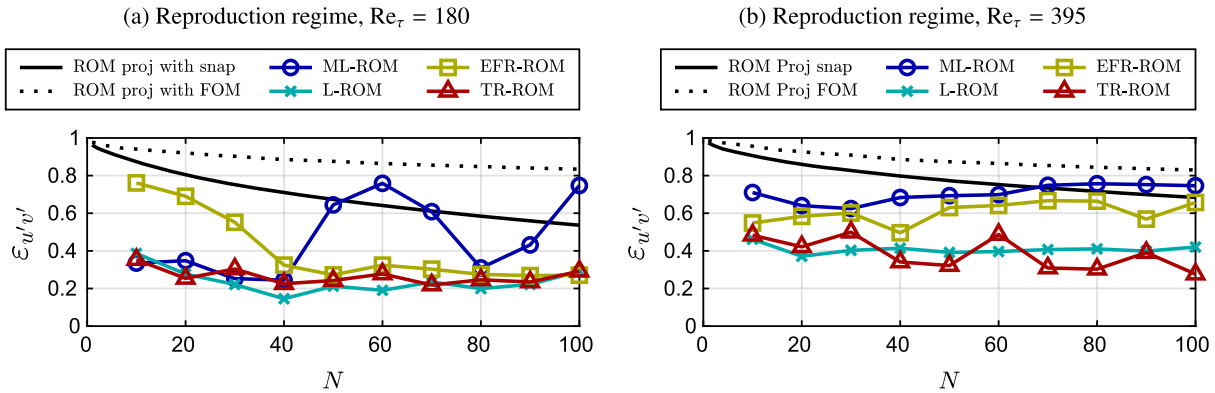

Fig. 5.19. The relative error $\varepsilon_{u'v'}$ (5.5) of the ROM projection, L-ROM, EFR-ROM, TR-ROM, and ML-ROM with respect to N in the reproduction regime for $\mathrm{Re}_\tau = 180$ and $\mathrm{Re}_\tau = 395$. For each N value, Reg-ROMs' errors are associated with $m = 1$ and optimal δ and χ values. ML-ROM's error is associated with the optimal eddy viscosity parameter that yields the most accurate Reynolds shear stress $\langle u'v' \rangle$.

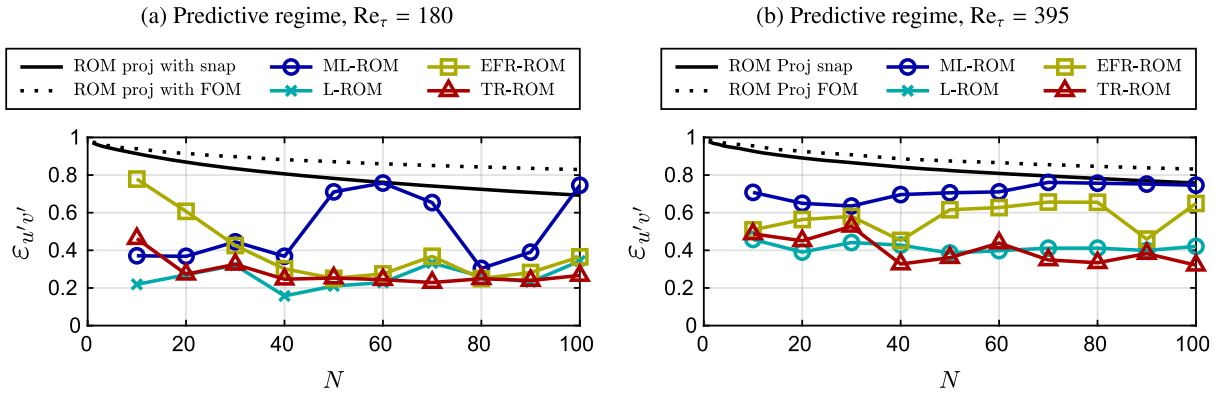

Fig. 5.20. The relative error $\varepsilon_{u'v'}$ (5.5) of the ROM projection, L-ROM, EFR-ROM, TR-ROM, and ML-ROM with respect to N in the predictive regime for $\mathrm{Re}_\tau = 180$ and $\mathrm{Re}_\tau = 395$. For each N value, the errors of the Reg-ROMs are associated with $m = 1$ and optimal δ and χ values optimized in the *reproduction regime*. The error of the ML-ROM is associated with the optimal eddy viscosity parameter optimized in the *reproduction regime*.

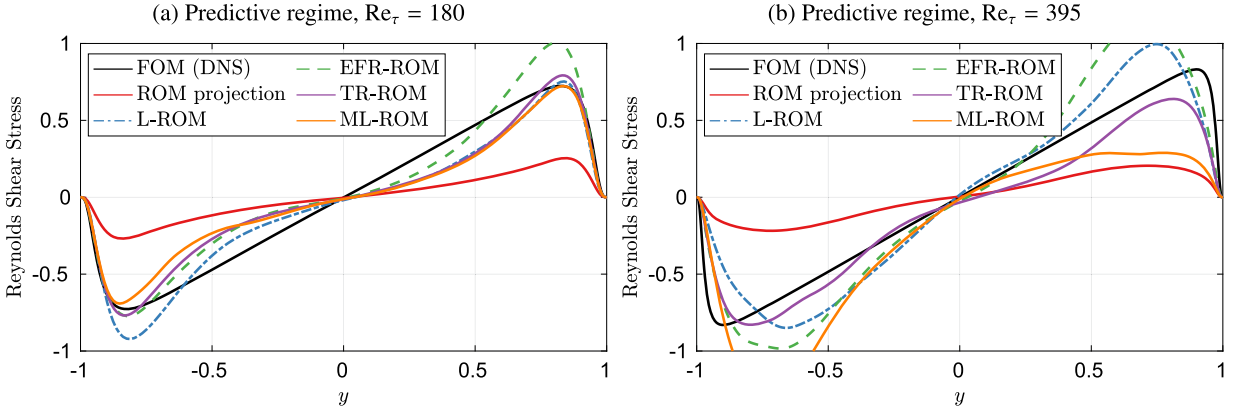

Fig. 5.21. Comparison of the Reynolds shear stress in the predictive regime of the FOM (black), the ROM projection (red), the optimal Reg-ROMs, listed in Table 2 and the optimal ML-ROM for $\mathrm{Re}_\tau = 180$ (left) and $\mathrm{Re}_\tau = 395$ (right).

We investigate the ML-ROM in the reproduction and predictive regimes for $\mathrm{Re}_\tau = 180$ and $\mathrm{Re}_\tau = 395$. In Fig. 5.19, the errors of the ML-ROM, ROM projection, and Reg-ROMs in the reproduction regime are shown for 10 N values. Note that Reg-ROMs' errors are associated with $m = 1$ and optimal δ and χ values. For ML-ROM, we conduct a parameter search for the optimal eddy viscosity parameter, ν_e, that yields the most accurate Reynolds shear stress $\langle u'v' \rangle$. In particular, for each $N \in \{10, 20, \ldots, 90, 100\}$, 10 ν_e values are uniformly sampled from the intervals $[0.001,\ 0.01]$, $[0.01, 0.1]$, and $[0.1, 1]$, resulting in a total of 30 ν_e values. The error associated to the ν_e value that yields the smallest $\varepsilon_{u'v'}$ is reported.

At $\mathrm{Re}_\tau = 180$, the error of ML-ROM with $N = 10, 20, 30, 40$ are similar to the errors of L-ROM and TR-ROM, and better than EFR-ROM. For $N > 40$, the error of ML-ROM is larger than the error of Reg-ROMs. We note that the error behavior of ML-ROM is also less stable compared to the errors of Reg-ROMs. A further investigation of this behavior should be performed. At $\mathrm{Re}_\tau = 395$, for all considered N values, the error of ML-ROM is larger compared to the errors of Reg-ROMs. We also note that, at both Re_τ, the error of ML-ROM can be larger than the error of ROM projection for certain N values.

In Fig. 5.20, the errors of the ML-ROM for 10 N values are shown, along with the errors of the ROM projection and Reg-ROMs in the predictive regime are presented. For ML-ROM and Reg-ROMs, the errors are associated with the optimal parameters optimized in the *reproduction regime*. At $\mathrm{Re}_\tau = 180$, the errors of the ML-ROM are higher for $N = 10, 30, 40$, and at $\mathrm{Re}_\tau = 395$, they consistently exceed the errors of Reg-ROMs for all N values. In both cases, the behavior of the error of the ML-ROM follows the same trend as in the reproduction regime.

We further compare the Reynolds shear stress of the optimal ML-ROM with the Reynolds shear stress of the FOM, ROM projection, and optimal Reg-ROMs in the predictive regime in Fig. 5.21. The optimal ML-ROM is chosen to be the one that has the smallest $\varepsilon_{u'v'}$ in Fig. 5.20. The optimal Reg-ROMs are those reported in Table 2. At $\mathrm{Re}_\tau = 180$, the Reynolds shear stress of ML-ROM is better than the Reynolds shear stress of L-ROM and EFR-ROM near the wall in terms of magnitude. Although the Reynolds shear stress profile of ML-ROM is similar to the one of TR-ROM, its peak value in the lower half of the channel is predicted at a different y value compared to the FOM and TR-ROM. Away from the wall, similar to the three Reg-ROMs, the ML-ROM's Reynolds shear stress is underestimated. At $\mathrm{Re}_\tau = 395$, the Reynolds shear stress of ML-ROM is highly underestimated in the upper half of the channel, and overestimated in the lower half of the channel compared to the FOM and TR-ROM.

This is our first step in comparing the Reg-ROMs with the eddy viscosity approaches. We are aware that there are other eddy viscosity approaches in the literature [61], for example, the Smagorinsky ROM, and dynamic subgrid-scale ROM. Those are considered to be more advanced models compared to the mixing-length model, and could yield better results. We hope to include a comprehensive comparison between regularized ROMs and more advanced eddy viscosity approaches in future work.

6. Conclusions and future work

In this paper, we propose the time-relaxation ROM (TR-ROM), which is a novel regularized ROM (Reg-ROM) for under-resolved turbulent flows. The TR-ROM employs ROM spatial filtering to smooth out the flow velocity and eliminate the spurious numerical oscillations displayed by the standard Galerkin ROM (G-ROM) (i.e., the ROM that does not use any numerical stabilization). We emphasize that one novel feature of the TR-ROM, which distinguishes it from the other Reg-ROM in current use (i.e., the Leray ROM (L-ROM) and the evolve-filter-relax ROM (EFR-ROM)), is that it introduces different dissipation for the large resolved scales and the small resolved scales. This is in stark contrast with the other two types of Reg-ROMs, i.e., L-ROM and EFR-ROM, which use spatial filtering without distinguishing between small and large resolved scales.

To assess the new TR-ROM, we compare it with the L-ROM and the EFR-ROM in the numerical simulation of the turbulent channel flow at $Re_\tau = 180$ and $Re_\tau = 395$ in both the reproduction and the predictive regimes. The spatial filtering in all three Reg-ROMs is performed using the first-order ROM differential filter or the higher-order ROM algebraic filter. In addition, we investigate the sensitivity of the Reg-ROMs with respect to the following parameters: the time interval, the relaxation parameter, and the filter radius. To our knowledge, this is the first numerical comparison of different Reg-ROMs in the numerical simulation of turbulent flows. We also compare the performance of Reg-ROMs with an eddy viscosity approach, the mixing-length ROM (ML-ROM).

Our numerical investigation yields the following conclusions: All three Reg-ROMs are dramatically more accurate than the classical G-ROM without significantly increasing its computational cost. In fact, with respect to several second-order turbulence statistics, the three Reg-ROMs' errors are much lower than the projection error. In addition, with the optimal parameters, the new TR-ROM yields more accurate results than the L-ROM and the EFR-ROM in all tests. Our numerical investigation also shows that the HOAF with filter order $m = 1$ yields the best results for most of the N values. On the other hand, the HOAF with $m > 1$ works better for small N, i.e., $N \leq 20$, at lower Reynolds number $\mathrm{Re}_\tau = 180$. The comparison with the ML-ROM shows that, for most N values, the Reynolds shear stress of the three Reg-ROMs is more accurate than the Reynolds shear stress of the ML-ROM in both the reproduction and the predictive regimes.

The sensitivity study shows that the optimal parameters trained in the reproduction regime $(\delta, \chi)_{\mathrm{recon}}$ are also optimal in the predictive regime for most of the N values and for all three Reg-ROMs. Although all three Reg-ROMs are sensitive with respect to the relaxation parameter, χ, and filter radius, δ, the optimal range for δ and the effect of χ are similar for the two Re_τ values.

From the numerical investigation of the HOAF (Section Appendix A.2.3), we found that the HOAF in the POD setting is indeed a spatial filter, and has a similar behavior as in the SEM setting, i.e., the higher-order filter (larger m) tends to damp the higher index modes more, and has less impact on the lower index modes.

The first steps in the numerical investigation of the new TR-ROM for the turbulent channel flow have been encouraging. There are, however, several other research directions that should be pursued next. For example, one can investigate whether ROM approximate deconvolution [62,63] can be leveraged to further increase the localization of the dissipation mechanism in the new TR-ROM. One could also compare the approximate deconvolution approach with the effect of increasing the order of the higher-order algebraic filter (3.3) in TR-ROM. In addition, a further investigation of the HOAF with $m \geq 2$ is required to gain a better understanding of the Reg-ROMs error behavior when a higher-order filter is used. Finally, TR-ROM's numerical analysis, which could yield new, robust parameter scalings [64], should be performed.

CRediT authorship contribution statement

Ping-Hsuan Tsai: Writing – review & editing, Writing – original draft, Visualization, Validation, Software, Methodology, Investigation, Data curation, Conceptualization. **Paul Fischer:** Writing – review & editing, Validation, Supervision, Methodology, Conceptualization. **Traian Iliescu:** Writing – review & editing, Writing – original draft, Validation, Supervision, Methodology, Conceptualization.

Declaration of competing interest

The authors declare that they have no known competing financial interests or personal relationships that could have appeared to influence the work reported in this paper.

Acknowledgements

The research used resources at the Oak Ridge Leadership Computing Facility at Oak Ridge National Laboratory, which is supported by the Office of Science of the U.S. Department of Energy under Contract DE-AC05-00OR22725, at the Argonne Leadership Computing Facility, under Contract DE-AC02-06CH11357, and at the Delta advanced computing, which is supported by the National Science Foundation (award OAC 2005572) and the State of Illinois.

P.T. and P.F. acknowledge support through he DOE Office of Nuclear Energy under the Nuclear Energy University Program (Projs. No. DE_NE0008780 and DE_NE0009396). T.I. acknowledges support through National Science Foundation grants DMS-2012253 and CDS&E-MSS-1953113.

We thank the reviewers for their comments and suggestions, which significantly improved the quality and clarity of the manuscript.

Appendix A. HOAF investigation

In this section, we perform a theoretical and numerical investigation of the HOAF (3.3), which, for clarity, we rewrite below: *Given* $\boldsymbol{u}_r = \sum_{j=1}^{N} u_{r,j}\boldsymbol{\varphi}_j$, *find* $\overline{\boldsymbol{u}}_r = \sum_{j=1}^{N} \overline{u}_{r,j}\boldsymbol{\varphi}_j$ *such that*

$$\left(\mathbb{I} + \delta^{2m} A^m\right)\underline{\overline{u}}_r = \underline{u}_r, \tag{A.1}$$

where $\underline{u}_r$ *and* $\underline{\overline{u}}_r$ *are the vectors of ROM basis coefficients of* $\boldsymbol{u}_r$ *and* $\overline{\boldsymbol{u}}_r$*, respectively, and* $m \geq 2$ *is an integer.*

We note that we consider only integers $m \geq 2$ because, as explained in Remark 3.1, the standard (low-order) DF (3.2) can be considered as a particular case of HOAF with $m = 1$. Thus, to distinguish between the DF and the HOAF, in this section we exclusively consider $m \geq 2$ in HOAF.

In addition, we note that the expansions for $\boldsymbol{u}_r$ and $\overline{\boldsymbol{u}}_r$ do not include the time-averaged velocity field, $\boldsymbol{\varphi}_0$. This is in contrast with the expansion (2.2), which does include $\boldsymbol{\varphi}_0$. The reason for not including $\boldsymbol{\varphi}_0$ in our expansions is that, in our numerical investigation, we decided not to filter the time-averaged velocity field, $\boldsymbol{\varphi}_0$, because this strategy was shown in [16] to yield more accurate results.

Moreover, we note that, in a spectral element setting, in [32] it was shown that HOAF (A.1) is a spatial filter that attenuates the high wavenumber components of the input field. Furthermore, it was also shown that the exponent m in the HOAF (A.1) controls the percentage of filtering at different wavenumbers: As m increases, the amount of filtering increases for the high wavenumber components of the input field, and decreases for the low wavenumber components [32, Figure 1].

In this section, we investigate whether the HOAF (A.1) is a spatial filter. We also study the role of the exponent m in the HOAF (A.1). We address this question first from a theoretical point of view (Section Appendix A.1), and then from a computational point of view (Section Appendix A.2).

A.1. Theoretical investigation

In this section, we perform a theoretical investigation of HOAF (A.1). To this end, we first discuss the *weak form (variational formulation)* of HOAF, which is needed to construct the ROM discretization of HOAF.

We note that the weak form for DF is clear: The DF linear systems (3.2) results from the ROM discretization of the weak form of the Helmholtz equation (3.1). Thus, because the DF can be interpreted as the HOAF (A.1) with $m = 1$, we hope we can leverage that to find the HOAF weak form.

We emphasize that finding the HOAF weak form is important. Indeed, the connection between HOAF (A.1) and its conjectured weak form is used in the physical interpretation of the time relaxation term (Case 2 in Section 4.3). More importantly, the HOAF weak form can tell us whether HOAF is a spatial filter, just as in the DF case.

In this section, we discuss the HOAF weak form for $m = 2$. We believe this discussion can be naturally extended to higher m values.

To discuss the HOAF weak form and the associated ROM formulation, we formally extend the mixed finite element discretization of the biharmonic equation proposed by Falk and Osborn [65], which is based on earlier work by Ciarlet and Raviart [66], Glowinski [67], and Mercier [68].

Because DF is HOAF with $m = 1$, it is natural to associate the following PDE with HOAF: *Given* $\boldsymbol{u} \in L^2(\Omega)$*, find* $\overline{\boldsymbol{u}} \in H_0^2(\Omega)$ *such that*

$$\delta^4 \Delta^2 \overline{\boldsymbol{u}} + \overline{\boldsymbol{u}} = \boldsymbol{u} \qquad \text{in } \Omega, \tag{A.2}$$

$$\overline{\boldsymbol{u}} = \frac{\partial \overline{\boldsymbol{u}}}{\partial \mathbf{n}} = 0 \qquad \text{on } \partial\Omega. \tag{A.3}$$

We note that, as pointed out in [66], the most straightforward finite element discretization of the biharmonic equation is to use a conforming method, in which the finite element space is a subspace of $H_0^2(\Omega) = \{\mathbf{v} \in H^2(\Omega) : \mathbf{v} = \frac{\partial \mathbf{v}}{\partial \boldsymbol{n}} = \mathbf{0} \text{ on } \partial\Omega\}$. Constructing such subspaces, however, requires sophisticated finite elements. Thus, to avoid these computational challenges, nonconforming finite elements have been proposed, in which the finite element space are subspaces of $H^1(\Omega)$. One such strategy is the mixed finite element formulation of the biharmonic equation proposed in [65], which utilizes standard finite element spaces in $H^1(\Omega)$.

We emphasize that, in our numerical investigation in Section 5, the spectral element discretization used to construct the ROM basis function is posed in $H_0^1(\Omega)$. Thus, we extend the mixed finite element strategy proposed in [65] to our ROM setting. To this end, we first define the following auxiliary variable:

$$\mathbf{w} := -\Delta \overline{\boldsymbol{u}}. \tag{A.4}$$

Next, we extend the weak form (3.3) in [65] to the PDE we considered in (A.2)–(A.3): *Given* $\boldsymbol{u} \in L^2(\Omega)$*, find* $(\mathbf{w}, \overline{\boldsymbol{u}}) \in (H_0^1(\Omega), H_0^1(\Omega))$ *such that*

$$(\mathbf{w}, \mathbf{v}_{\mathbf{w}}) - (\nabla \overline{\boldsymbol{u}}, \nabla \mathbf{v}_{\mathbf{w}}) = 0 \qquad \forall\, \mathbf{v}_{\mathbf{w}} \in H_0^1(\Omega) \tag{A.5}$$

$$\delta^4 (\nabla \mathbf{w}, \nabla \mathbf{v}_{\overline{\boldsymbol{u}}}) + (\overline{\boldsymbol{u}}, \mathbf{v}_{\overline{\boldsymbol{u}}}) = (\boldsymbol{u}, \mathbf{v}_{\overline{\boldsymbol{u}}}) \qquad \forall\, \mathbf{v}_{\overline{\boldsymbol{u}}} \in H_0^1(\Omega) \tag{A.6}$$

Remark A.1 *(ROM-FEM Weak Form).* We note that, although the weak form (A.5)–(A.6) is similar to the weak form (3.3) in [65], there are several significant differences. Probably the most important difference is that we use $H_0^1(\Omega)$ instead of $H^1(\Omega)$ to approximate the auxiliary variable $\mathbf{w}$. Our choice is motivated by the spectral element space used in our numerical investigation in Section 5, which is a subspace of $H_0^1(\Omega)$.

To find the ROM discretization of the weak formulations (A.5) and (A.6), we use the classical Galerkin method: For (A.5), we consider the ROM expansions $\overline{\boldsymbol{u}} \approx \overline{\boldsymbol{u}}_{\mathrm{r}} = \sum_{j=1}^{N} \overline{u}_{\mathrm{r},j} \boldsymbol{\varphi}_j$ and $\mathbf{w} \approx \mathbf{w}_{\mathrm{r}} = \sum_{j=1}^{N} w_{\mathrm{r},j} \boldsymbol{\varphi}_j$, and choose the test functions $\mathbf{v}_{\mathbf{w}} := \boldsymbol{\varphi}_i, i = 1, \ldots, N$. This yields the following linear system:

$$\mathbb{I} \underline{w}_{\mathrm{r}} = A \underline{\overline{u}}_{\mathrm{r}}, \tag{A.7}$$

where $\underline{w}_{\mathrm{r}}$ and $\underline{\overline{u}}_{\mathrm{r}}$ are the vector of ROM coefficients of $\mathbf{w}_{\mathrm{r}}$ and $\overline{\boldsymbol{u}}_{\mathrm{r}}$, respectively, and $\mathbb{I}$ and A are the identity and ROM stiffness matrices, respectively.

To find the ROM discretization of the weak formulation (A.6), we use again the ROM expansions $\overline{\boldsymbol{u}} \approx \overline{\boldsymbol{u}}_{\mathrm{r}} = \sum_{j=1}^{N} \overline{u}_{\mathrm{r},j} \boldsymbol{\varphi}_j$ and $\mathbf{w} \approx \mathbf{w}_{\mathrm{r}} = \sum_{j=1}^{N} w_{\mathrm{r},j} \boldsymbol{\varphi}_j$, and choose the test functions $\mathbf{v}_{\overline{\boldsymbol{u}}} := \boldsymbol{\varphi}_i, i = 1, \ldots, N$. This yields the following linear system:

$$\delta^4 A \underline{w}_{\mathrm{r}} + \mathbb{I} \underline{\overline{u}}_{\mathrm{r}} = \mathbb{I} \underline{u}_{\mathrm{r}}, \tag{A.8}$$

where $\underline{u}_{\mathrm{r}}$ is the vector of ROM coefficients of $\boldsymbol{u}_{\mathrm{r}}$. Plugging the formula for $\underline{w}_{\mathrm{r}}$ in (A.7) in (A.8) yields

$$\delta^4 A \left(A \underline{\overline{u}}_{\mathrm{r}} \right) + \mathbb{I} \underline{\overline{u}}_{\mathrm{r}} = \mathbb{I} \underline{u}_{\mathrm{r}}, \tag{A.9}$$

which is exactly the HOAF linear system (A.1) for $m = 2$.

Thus, for $m = 2$, we have shown that the ROM discretization of the weak forms (A.5) and (A.6) is the HOAF linear system (A.1).

We note that, in a spectral element setting, the PDE associated with HOAF (A.1) was discussed in [32] (albeit with a missing minus sign).

A.2. Numerical investigation

In this section, we investigate whether the HOAF (A.1) is a spatial filter by solving (A.1) and examining if the output $\overline{\boldsymbol{u}}$ is smoother compared to the input $\boldsymbol{u}$. We also study the role of the exponent m in the HOAF. In sections Appendix A.2.1–Appendix A.2.2, we investigate the HOAF in one- and two-dimensional spectral element (SEM) settings. In section Appendix A.2.3, we investigate the HOAF in a POD setting. We note that a similar numerical investigation was carried out in the spectral element setting in [32], where it was shown that HOAF (A.1) is a low-pass filter [32, Figure 1].

A.2.1. One-dimensional SEM setting

We consider the spatial domain $\Omega = [0, 1]$ and construct the HOAF (A.1) using a SEM discretization that consists of a 64-dimensional array of 7th-order spectral elements. Note that, in the SEM setting, instead of A^m we use $(B^{-1}A)^m$ in (A.1), and $\underline{u}$ and $\underline{\overline{u}}$ are the SEM basis coefficients for the input (unfiltered) and output (filtered) functions, respectively.

We construct an input function u that has both low and high wavenumber components:

$$u(x) = 0.5 \sin(2\pi x) + 0.5 \sin(10\pi x) + 2 \sin(20\pi x), \tag{A.10}$$

and set the filter radius δ to be 0.025. We then consider four m values and compare the corresponding HOAF output $\overline{u}$ with the input function u in Fig. A.1.

The $m = 1$ results show that, although HOAF has attenuated the high wavenumber ($k = 20$) component of the input function, that component is still visible. However, as we increase the HOAF order (i.e., use $m = 2, 3, 4$), the high wavenumber component of the input function starts to significantly decrease. In fact, for $m = 4$, the high wavenumber component is practically eliminated. We also note that the medium wavenumber ($k = 10$) component of the input function is affected differently by the different m values: For $m = 1$, the medium wavenumber component is slightly attenuated. In contrast, for $m = 4$, the medium wavenumber component remains unchanged. Finally, the low wavenumber ($k = 2$) component of the input function is practically unaffected by the HOAF order. Thus, the results in Fig. A.1 suggest that, as expected, using the classical DF (i.e., HOAF with $m = 1$) attenuates the medium and high wavenumber components of the input function. The higher-order HOAF (i.e., HOAF with $m = 2, 3, 4$) attenuates more the high wavenumber component, and almost not at all the medium wavenumber component.

A.2.2. Two-dimensional SEM setting

We consider the spatial domain $\Omega = [0, 1]^2$ and construct the HOAF (A.1) using a SEM discretization that consists of a 12×12 array of 7th-order spectral elements. We construct an input function u that has both low and high wavenumber components:

$$u(x, y) = 0.5 \sin(2\pi x) \sin(2\pi y) + \sin(4\pi x) \sin(4\pi y) + 2 \sin(6\pi x) \sin(6\pi y), \tag{A.11}$$

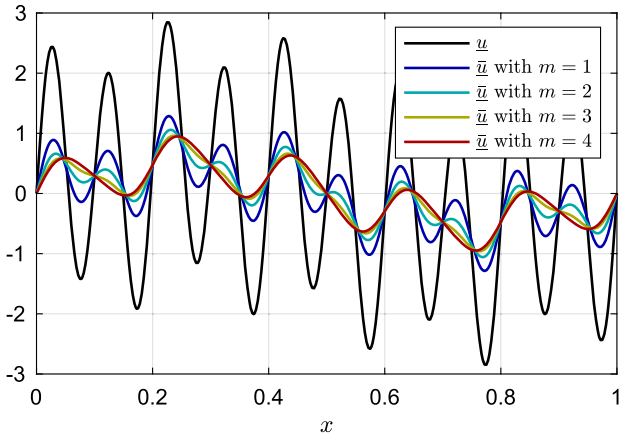

Fig. A.1. Comparison of the input function $u(x) = 0.5\sin(2\pi x) + 0.5\sin(10\pi x) + 2\sin(20\pi x)$ and four HOAF outputs $\bar{u}$ that correspond to $m = 1,\ 2,\ 3,\ 4$, and $\delta = 0.025$.

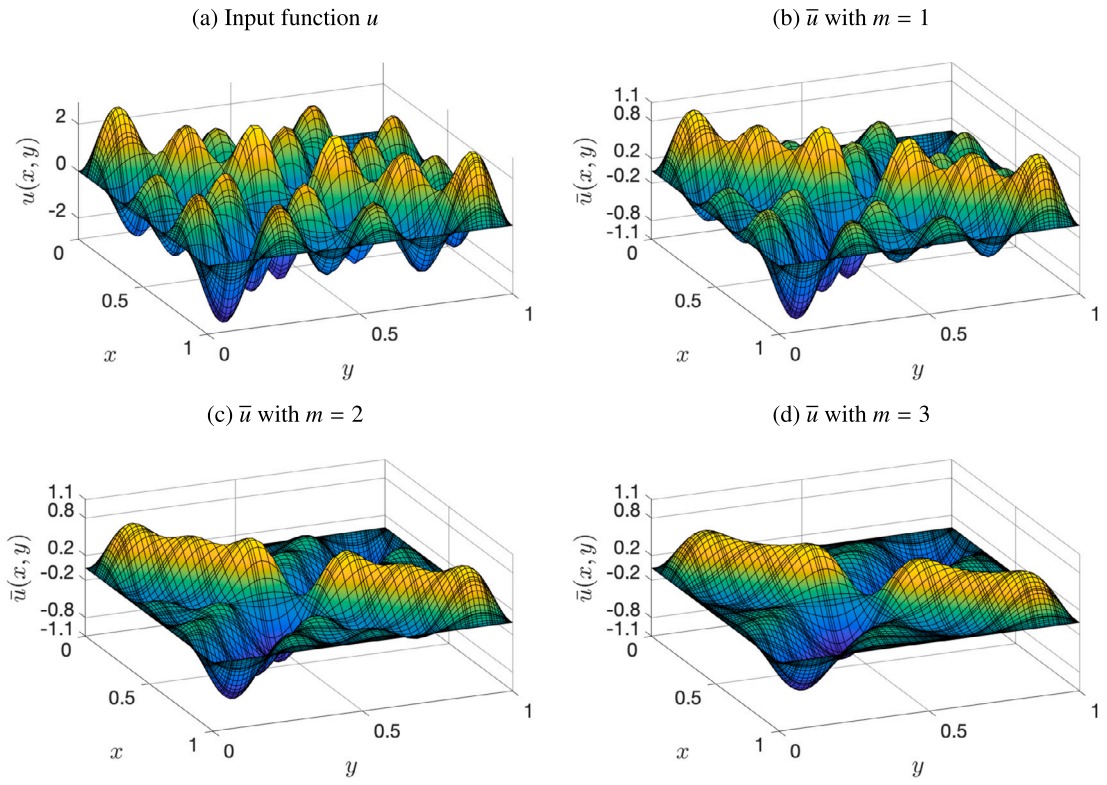

Fig. A.2. Comparison of the input function $u(x, y) = 0.5\sin(2\pi x)\sin(2\pi y) + \sin(4\pi x)\sin(4\pi y) + 2\sin(6\pi x)\sin(6\pi y)$ and three HOAF outputs $\bar{u}$ corresponding to $m = 1,\ 2,\ 3$ with $\delta = 0.06$.

and set the filter radius δ to be 0.06. We then consider three m values and compare the corresponding HOAF output $\bar{u}$ with the input function u in Fig. A.2. The $m = 1$ results show that, although HOAF has attenuated the high wavenumber ($(k_1, k_2) = (6, 6)$ component of the input function, that component is still visible. However, as we increase the HOAF order (i.e., use $m = 2, 3$), the high wavenumber component of the input function starts to significantly decrease. We also note that the medium wavenumber ($(k_1, k_2) = (4, 4)$) component of the input function is affected differently by the different m values: For $m = 1$, the medium wavenumber component is slightly attenuated. In contrast, for $m = 3$, the medium wavenumber component remains unchanged. Finally, the low wavenumber ($(k_1, k_2) = (2, 2)$) component of the input function is unaffected by the HOAF order. Thus, the results in Fig. A.2 again suggest that the classical DF (i.e., HOAF with $m = 1$) attenuates the medium and high wavenumber components of the input function. The higher-order HOAF (i.e., HOAF with $m = 2, 3$) attenuates more the high wavenumber component, and almost not at all the medium wavenumber component.

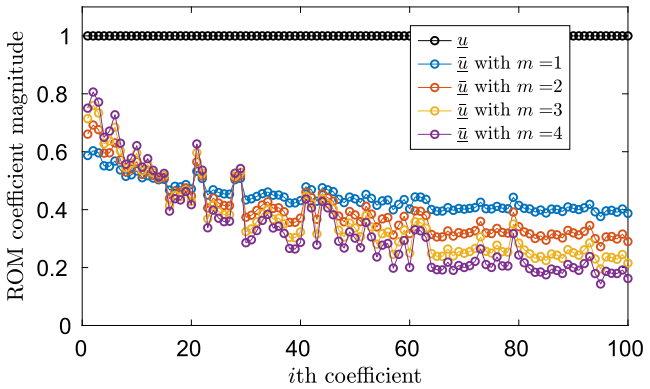

Fig. A.3. The unfiltered and filtered coefficient magnitude of the ith POD basis function, u_i and $\bar{u}_i$, with four filter order values $m = 1,\ 2,\ 3,\ 4$ for $i = 1, \ldots, N$. The HOAF (A.1) is formed using $N = 100$ L^2 POD basis functions and a filter radius of $\delta = 0.08125$.

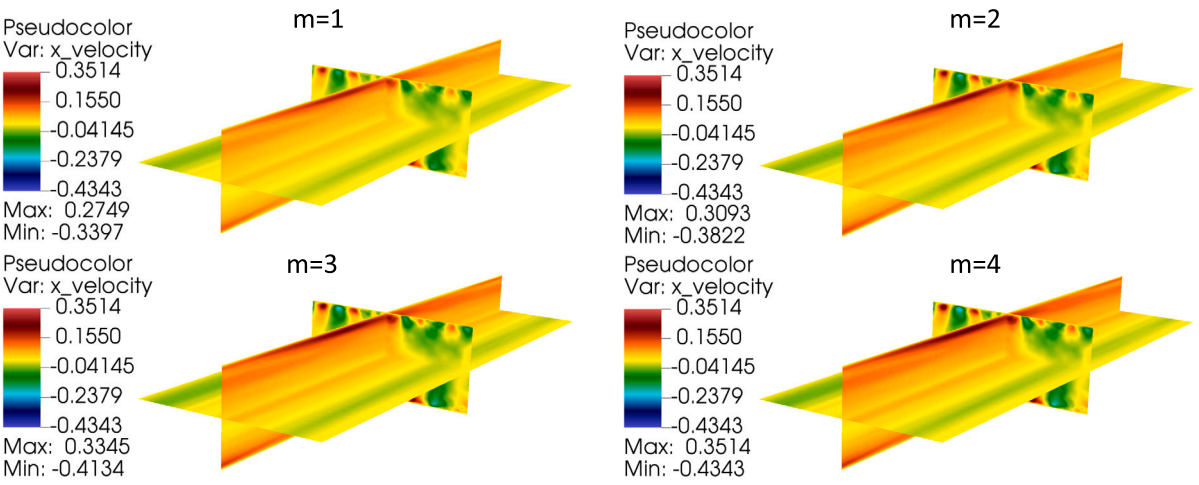

Fig. A.4. Comparison of streamwise component of the 1st filtered POD basis function for four filter order values $m = 1,\ 2,\ 3,\ 4$. The HOAF is constructed with $N = 100$ basis functions and filter radius $\delta = 0.08125$. The display range is fixed to be $[-0.4343,\ 0.3514]$ and the maximum and minimum magnitudes are reported in the legend.

A.2.3. POD setting

We investigate the HOAF (A.1) in a POD setting. In particular, we consider the POD basis functions for the turbulent channel flow at $\mathrm{Re}_\tau = 180$, as detailed in Section 5.2. The HOAF is constructed using $N = 100$ L^2 POD basis functions, and filter radius $\delta = 0.08125$. The δ value is chosen such that the damping is neither too strong nor too weak.

To understand how each POD basis function is affected by the HOAF with different m values, we consider the following procedure: For a given m value, and for each mode i, where $1 \le i \le N$, we construct an input coefficient vector $\underline{u} = [0, \ldots, 0, 1, 0, \ldots, 0]^T$, where 1 appears only in the ith component (i.e., $u_i = 1$) and obtain the output vector $\underline{\bar{u}}$ by solving the HOAF linear system (A.1). The ith component of the output vector $\underline{\bar{u}}$ (i.e., $\bar{u}_i$) indicates the amount of damping caused by the HOAF in the ith POD basis function.

Fig. A.3 displays the unfiltered and the filtered coefficient magnitude of the ith POD basis function, u_i (black) and $\bar{u}_i$ (multi-colored), with four filter order values $m = 1,\ 2,\ 3,\ 4$, for $i = 1, \ldots, N$. Note that, for each mode i, although the input vector $\underline{u}$ has only zero components except the ith component (i.e., $u_i = 1$), the output vector $\underline{\bar{u}}$ could have a nonzero jth component (i.e., $\bar{u}_j \neq 0$) for $j \neq i$, because the input vector $\underline{u}$ is not necessary an eigenvector of the HOAF. In Fig. A.3, for each mode i, we show only the behavior of $\bar{u}_i$ because the purpose of this study is to investigate how each ith POD basis function is affected by the HOAF. In addition, we observe that, although $\underline{\bar{u}}$ contains excitations of other modes, these nonzero values are relatively small compared to the ith component.

In Fig. A.3, we see the expected behavior: Increasing m yields a sharper drop in the transfer function $(\bar{u}_i/u_i)$ for high mode numbers, i, with less suppression of the low mode numbers, which is consistent with an interpretation of the POD modes as "Fourier" modes. Note that all the curves intersect at $\bar{u}_i/u_i \approx 1/2$ near $i = 15$, which implies that modes with $i < 15$ have characteristic length scales $\lambda_i > \delta = 0.08125$, given that we expect

$$\frac{\bar{u}_i}{u_i} \sim \frac{1}{1 + (\delta/\lambda_i)^{2m}} .$$

Thus, we see that, in this case, the HOAF provides a convenient means to associate a length scale with each mode.

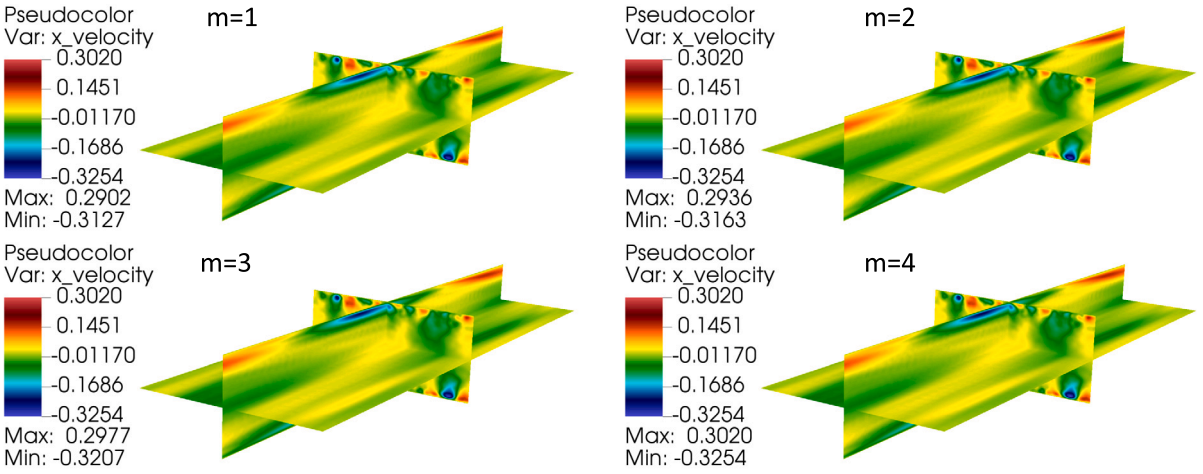

Fig. A.5. Comparison of streamwise component of the 15th filtered POD basis function for four filter order values $m = 1,\ 2,\ 3,\ 4$. The HOAF is constructed with $N = 100$ basis functions and filter radius $\delta = 0.08125$. The display range is fixed to be $[-0.3254,\ 0.3020]$ and the maximum and minimum magnitudes are reported in the legend.

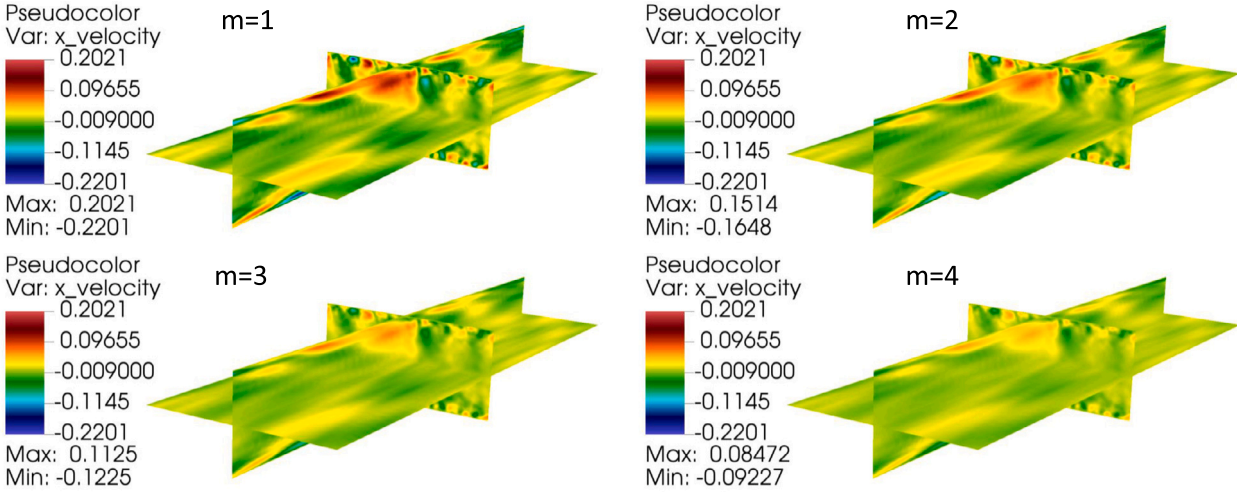

Fig. A.6. Comparison of streamwise component of the 100th filtered POD basis function for four filter order values $m = 1,\ 2,\ 3,\ 4$. The HOAF is constructed with $N = 100$ basis functions and filter radius $\delta = 0.08125$. The display range is fixed to be $[-0.2201,\ 0.2201]$ and the maximum and minimum magnitudes are reported in the legend.

Figs. A.4–A.6 illustrate the physical-space effect of the HOAF with $m = 1,\ 2,\ 3,\ 4$ and $\delta = 0.08125$ for modes $i = 1, 15$, and 100. It is clear that the higher-order filter (i.e., a larger m value) has less damping in mode $i = 1$ and more damping in mode $i = 100$. For mode $i = 15$, all m values yield similar damping. Because the filtered basis function is simply the unfiltered basis function weighted by the coefficients given in Fig. A.3, we expect the filtered basis function for different m values to differ only in the magnitude. Thus, in Figs. A.4–A.6, to compare the damping for different m values, we compare the maximum and minimum magnitudes that are reported in the legends.

Overall, these results show that the HOAF in the POD setting has a similar behavior as in the SEM setting, that is, larger m values tend to damp the higher modes more and have less impact on the lower modes compared to smaller m values. However, unlike in the SEM setting where the low-wave number modes are usually undamped regardless of the m value, all POD modes are damped in the POD setting.

In this numerical investigation we exclusively used L^2 POD basis functions, which is the most popular choice in reduced order modeling. We note, however, that the H_0^1 POD basis functions could provide a clearer illustration of the HOAF spatial filtering capabilities. Indeed, as highlighted in [14], the H_0^1 POD basis functions are better in capturing the small-scale structures and distinguishing them from the large-scale structures in the solution compared to the L^2 POD basis functions. Hence, we anticipate more distinct results in the filtered coefficients when the HOAF is constructed by using the H_0^1 POD basis functions.

Data availability

Data will be made available on request.

References

[1] S.L. Brunton, J.N. Kutz, Data-Driven Science and Engineering: Machine Learning, Dynamical Systems, and Control, Cambridge University Press, 2019.
[2] J.S. Hesthaven, G. Rozza, B. Stamm, Certified Reduced Basis Methods for Parametrized Partial Differential Equations, Springer, 2015.
[3] B.R. Noack, M. Morzynski, G. Tadmor, Reduced-Order Modelling for Flow Control, vol. 528, Springer Verlag, 2011.
[4] A. Quarteroni, A. Manzoni, F. Negri, Reduced Basis Methods for Partial Differential Equations: An Introduction, vol. 92, Springer, 2015.
[5] J. Kim, P. Moin, R. Moser, Turbulence statistics in fully developed channel flow at low Reynolds number, J. Fluid Mech. 177 (1987) 133–166.
[6] R. Moser, J. Kim, N.N. Mansour, Direct numerical simulation of turbulent channel flow up to $Re_\tau = 590$, Phys. Fluids 11 (4) (1999) 943–945.
[7] S.E. Ahmed, S. Pawar, O. San, A. Rasheed, T. Iliescu, B.R. Noack, On closures for reduced order models — a spectrum of first-principle to machine-learned avenues, Phys. Fluids 33 (9) (2021) 091301.
[8] P. Tsai, P. Fischer, E. Solomonik, Accelerating the Galerkin reduced-order model with the tensor decomposition for turbulent flows, arXiv preprint arXiv: 2311.03694, 2023.
[9] M. Couplet, P. Sagaut, C. Basdevant, Intermodal energy transfers in a proper orthogonal decomposition–Galerkin representation of a turbulent separated flow, J. Fluid Mech. 491 (2003) 275–284.
[10] K. Carlberg, C. Bou-Mosleh, C. Farhat, Efficient non-linear model reduction via a least-squares Petrov–Galerkin projection and compressive tensor approximations, Int. J. Numer. Methods Eng. 86 (2) (2011) 155–181.
[11] E.J. Parish, C. Wentland, K. Duraisamy, The adjoint Petrov–Galerkin method for non-linear model reduction, Comput. Methods Appl. Mech. Eng. 365 (2020) 112991.
[12] C. Mou, E. Merzari, O. San, T. Iliescu, An energy-based lengthscale for reduced order models of turbulent flows, Nucl. Eng. Des. 412 (2023) 112454.
[13] K. Kaneko, An augmented basis method for reduced order models of turbulent flow, Ph.D. thesis, 2022.
[14] L. Fick, Y. Maday, A.T. Patera, T. Taddei, A stabilized POD model for turbulent flows over a range of Reynolds numbers: optimal parameter sampling and constrained projection, J. Comput. Phys. 371 (2018) 214–243.
[15] P. Johansson, H. Andersson, E. Rønquist, Reduced-basis modeling of turbulent plane channel flow, Comput. Fluids 35 (2) (2006) 189–207.
[16] D. Wells, Z. Wang, X. Xie, T. Iliescu, An evolve-then-filter regularized reduced order model for convection-dominated flows, Int. J. Numer. Methods Fluids 84 (2017) 598–615.
[17] F. Sabetghadam, A. Jafarpour, α regularization of the POD-Galerkin dynamical systems of the Kuramoto–Sivashinsky equation, Appl. Math. Comput. 218 (10) (2012) 6012–6026.
[18] M. Strazzullo, M. Girfoglio, F. Ballarin, T. Iliescu, G. Rozza, Consistency of the full and reduced order models for evolve-filter-relax regularization of convection-dominated, marginally-resolved flows, Int. J. Numer. Methods Eng. 123 (14) (2022) 3148–3178.
[19] K. Kaneko, P.-H. Tsai, P. Fischer, Towards model order reduction for fluid-thermal analysis, Nucl. Eng. Des. 370 (2020) 110866.
[20] P. Fischer, M. Schmitt, A. Tomboulides, Recent developments in spectral element simulations of moving-domain problems, in: Recent Progress and Modern Challenges in Applied Mathematics, Modeling and Computational Science, Springer, 2017, pp. 213–244.
[21] N. Ghaddar, G. Karniadakis, A. Patera, A conservative isoparametric spectral element method for forced convection; application to fully developed flow in periodic geometries, Numer. Heat Transf., Part A, Appl. 9 (3) (1986) 277–300.
[22] S. Patankar, C. Liu, E. Sparrow, Fully Developed Flow and Heat Transfer in Ducts Having Streamwise-Periodic Variations of Cross-Sectional Area, 1977.
[23] P. Tsai, P. Fischer, Parametric model-order-reduction development for unsteady convection, Front. Phys. 10 (2022) 903169.
[24] G. Berkooz, P. Holmes, J. Lumley, The proper orthogonal decomposition in the analysis of turbulent flows, Annu. Rev. Fluid Mech. 25 (1) (1993) 539–575.
[25] S. Volkwein, Proper Orthogonal Decomposition: Theory and Reduced-Order Modelling, Lecture Notes, University of Konstanz, 2013, http://www.math.uni-konstanz.de/numerik/personen/volkwein/teaching/POD-Book.pdf.
[26] F. Ballarin, A. Manzoni, A. Quarteroni, G. Rozza, Supremizer stabilization of POD–Galerkin approximation of parametrized steady incompressible Navier–Stokes equations, Int. J. Numer. Methods Eng. 102 (2015) 1136–1161.
[27] V. DeCaria, T. Iliescu, W. Layton, M. McLaughlin, M. Schneier, An artificial compression reduced order model, SIAM J. Numer. Anal. 58 (1) (2020) 565–589.
[28] B.R. Noack, P. Papas, P.A. Monkewitz, The need for a pressure-term representation in empirical Galerkin models of incompressible shear flows, J. Fluid Mech. 523 (2005) 339–365.
[29] M. Germano, Differential filters of elliptic type, Phys. Fluids 29 (6) (1986) 1757–1758.
[30] W.J. Layton, L.G. Rebholz, Approximate Deconvolution Models of Turbulence: Analysis, Phenomenology and Numerical Analysis, vol. 2042, Springer, Berlin Heidelberg, 2012.
[31] M. Girfoglio, A. Quaini, G. Rozza, A linear filter regularization for POD-based reduced-order models of the quasi-geostrophic equations, C. R., Méc. 351 (S1) (2023) 1–21.
[32] J.S. Mullen, P.F. Fischer, Filtering techniques for complex geometry fluid flows, Commun. Numer. Methods Eng. 15 (1) (1999) 9–18.
[33] M. Gunzburger, T. Iliescu, M. Mohebujjaman, M. Schneier, An evolve-filter-relax stabilized reduced order stochastic collocation method for the time-dependent Navier-Stokes equations, SIAM/ASA J. Uncertain. Quantificat. 7 (4) (2019) 1162–1184.
[34] J. Leray, Sur le mouvement d'un fluide visqueux emplissant l'espace, Acta Math. 63 (1934) 193–248.
[35] B.J. Geurts, D.D. Holm, Regularization modeling for large-eddy simulation, Phys. Fluids 15 (1) (2003) L13–L16.
[36] J. Guermond, J. Oden, S. Prudhomme, Mathematical perspectives on large eddy simulation models for turbulent flows, J. Math. Fluid Mech. 6 (2) (2004) 194–248.
[37] J. Guermond, R. Pasquetti, B. Popov, Entropy viscosity method for nonlinear conservation laws, J. Comput. Phys. 230 (11) (2011) 4248–4267.
[38] C. Foiaş, D. Holm, E. Titi, The Navier-Stokes-alpha model of fluid turbulence, in: Advances in Nonlinear Mathematics and Science, Physica D 152/153 (2001) 505–519.
[39] M. Girfoglio, A. Quaini, G. Rozza, A POD-Galerkin reduced order model for a LES filtering approach, J. Comput. Phys. 436 (2021) 110260.
[40] M. Girfoglio, A. Quaini, G. Rozza, A hybrid projection/data-driven reduced order model for the Navier-Stokes equations with nonlinear filtering stabilization, J. Comput. Phys. 486 (2023) 112127.
[41] M. Gunzburger, T. Iliescu, M. Schneier, A Leray regularized ensemble-proper orthogonal decomposition method for parameterized convection-dominated flows, IMA J. Numer. Anal. 40 (2) (2020) 886–913.
[42] M. Girfoglio, A. Quaini, G. Rozza, A novel large eddy simulation model for the quasi-geostrophic equations in a finite volume setting, J. Comput. Appl. Math. 418 (2023) 114656.
[43] M.O. Deville, P.F. Fischer, E.H. Mund, High-Order Methods for Incompressible Fluid Flow, Cambridge Monographs on Applied and Computational Mathematics, vol. 9, Cambridge University Press, Cambridge, 2002.
[44] M. Strazzullo, F. Ballarin, T. Iliescu, C. Canuto, New feedback control and adaptive evolve-filter-relax regularization for the Navier-Stokes equations in the convection-dominated regime, arXiv preprint http://arxiv.org/abs/2307.00675, 2023.

[45] S. Stolz, N. Adams, L. Kleiser, An approximate deconvolution model for large-eddy simulation with application to incompressible wall-bounded flows, Phys. Fluids 13 (4) (2001) 997–1015.
[46] S. Stolz, N. Adams, L. Kleiser, The approximate deconvolution model for large-eddy simulations of compressible flows and its application to shock-turbulent-boundary-layer interaction, Phys. Fluids 13 (10) (2001) 2985–3001.
[47] N.A. Adams, S. Stolz, A subgrid-scale deconvolution approach for shock capturing, J. Comput. Phys. 178 (2) (2002) 391–426.
[48] W. Layton, M. Neda, Truncation of scales by time relaxation, J. Math. Anal. Appl. 325 (2) (2007) 788–807.
[49] P. Schlatter, S. Stolz, L. Kleiser, Evaluation of high-pass filtered eddy-viscosity models for large-eddy simulation of turbulent flows, J. Turbul. 6 (2005) N5.
[50] M. Olshanskii, X. Xiong, A connection between filter stabilization and eddy viscosity models, Numer. Methods Partial Differ. Equ. 29 (6) (2013) 2061–2080.
[51] P. Fischer, J. Kruse, J. Mullen, H. Tufo, J. Lottes, S. Kerkemeier, Nek5000–Open Source Spectral Element CFD Solver, Argonne National Laboratory, Mathematics and Computer Science Division, Argonne, IL, 2008, https://nek5000.mcs.anl.gov/index.php/MainPage.
[52] P. Fischer, S. Kerkemeier, M. Min, Y.-H. Lan, M. Phillips, T. Rathnayake, E. Merzari, A. Tomboulides, A. Karakus, N. Chalmers, et al., NekRS, a GPU-accelerated spectral element Navier–Stokes solver, Parallel Comput. (2022) 102982.
[53] A. Vreman, G. Kuerten, Comparison of direct numerical simulation databases of turbulent channel flow at $Re_\tau = 180$, Phys. Fluids 26 (1) (2014) 015102.
[54] K. Kaneko, P. Tsai, P. Fischer, NekROM, https://github.com/Nek5000/NekROM.
[55] V.J. Ervin, W.J. Layton, M. Neda, Numerical analysis of filter-based stabilization for evolution equations, SIAM J. Numer. Anal. 50 (5) (2012) 2307–2335.
[56] P. Tsai, Parametric model order reduction development for Navier-Stokes equations from 2d chaotic to 3d turbulent flow problems, Ph.D. thesis, 2023.
[57] S. Pope, Turbulent flows, Combust. Flame 125 (2000) 1361–1362, Cambridge University Press, Cambridge, UK.
[58] N. Aubry, P. Holmes, J.L. Lumley, E. Stone, The dynamics of coherent structures in the wall region of a turbulent boundary layer, J. Fluid Mech. 192 (1988) 115–173.
[59] B. Podvin, J. Lumley, A low-dimensional approach for the minimal flow unit, J. Fluid Mech. 362 (1998) 121–155.
[60] B. Podvin, A proper-orthogonal-decomposition–based model for the wall layer of a turbulent channel flow, Phys. Fluids 21 (2009) 015111.
[61] Z. Wang, I. Akhtar, J. Borggaard, T. Iliescu, Proper orthogonal decomposition closure models for turbulent flows: a numerical comparison, Comput. Methods Appl. Mech. Eng. 237–240 (2012) 10–26.
[62] A. Sanfilippo, I.R. Moore, F. Ballarin, T. Iliescu, Approximate deconvolution Leray reduced order model, arXiv preprint http://arxiv.org/abs/arXiv:2307.10817, 2023.
[63] X. Xie, D. Wells, Z. Wang, T. Iliescu, Approximate deconvolution reduced order modeling, Comput. Methods Appl. Mech. Eng. 313 (2017) 512–534.
[64] X. Xie, D. Wells, Z. Wang, T. Iliescu, Numerical analysis of the Leray reduced order model, J. Comput. Appl. Math. 328 (2018) 12–29.
[65] R.S. Falk, J.E. Osborn, Error estimates for mixed methods, ESAIM: Math. Model. Numer. Anal. 14 (1980) 249–277.
[66] P.G. Ciarlet, P.-A. Raviart, A mixed finite element method for the biharmonic equation, in: Mathematical Aspects of Finite Elements in Partial Differential Equations, Elsevier, 1974, pp. 125–145.
[67] R. Glowinski, Approximations externes, par éléments finis de Lagrange d'ordre un et deux, du problème de Dirichlet pour l'operateur biharmonique. Méthode iterative de résolution des problèmes approches, in: Topics in Numerical Analysis, 1973, pp. 123–171.
[68] B. Mercier, Numerical solution of the biharmonic problem by mixed finite elements of class C0, Boll. Unione Mat. Ital. 10 (1) (1974) 133–149.